



Leibniz
Universität
Hannover



ALBERT EINSTEIN INSTITUTE
HANNOVER
(MAX PLANCK INSTITUTE FOR
GRAVITATIONAL PHYSICS)

LEIBNIZ UNIVERSITÄT HANNOVER

MASTER DEGREE PROJECT

Emission beam geometry of PSR J2007+2722 derived from pulse polarization data

Author:

Tjark MIENER
2860000

Supervisors:

Prof. Dr. Bruce ALLEN
Dr. Benjamin KNISPEL

February 22, 2018

Declaration of autonomy

I hereby declare to have written the present work independently and only with help of specified sources and resources. The passages in the text, which, in their wording or meaning, were taken from other sources are clearly identified through their stated origin. The present work has not been submitted for another degree or diploma at any university or other institute of higher education.

Hannover, the 22nd of February, 2018

Abstract

The task of this master degree project is to derive the emission beam geometry of PSR J2007+2722 from pulse polarization data. Therefore, the fundamentals of polarization, especially the Stokes parameters, are presented. The pulse polarization data of PSR J2007+2722 provides full Stokes parameters at observing frequencies 1500 and 2000 MHz, whence the polarization position angle curves are determined. The emission beam geometry of PSR J2007+2722, which was derived by B. Allen and B. Knispel [2] in 2013 from the conventional *rotating vector model* (RVM), is confirmed in this thesis.

This thesis provides further investigations, since the RVM only describes the data to a certain degree. In the discussion, several new attempts to explain the deviations and particularities of PSR J2007+2722 are accomplished. One successful attempt is to disregard the data points of the almost completely depolarized part at 2000 MHz for the RVM fitting. This leads to a higher consistency between the emission beam geometries at both observing frequencies. The attempt to describe the pulse polarization data of PSR J2007+2722, by extending the RVM with the interpulse (IP), failed. This project suggests that the superposition of the mainpulse (MP) and the IP can not improve the previous RVM fitting. The polarization position angle ψ_{MP} of the MP is equal to the polarization position angle ψ_{IP} of the IP. However, the idea of the attempt is carried out using the superposition of the MP and a fixed linear polarization, which is produced by an assumed source of radiation. This model is called *background radiation model* (BRM) and is able to describe the pulse polarization data of PSR J2007+2722 much better than the RVM.

Contents

1. Introduction	1
2. Polarization	3
2.1. Polarization ellipse	3
2.2. Derivation of the Stokes polarization parameters	6
2.3. Complex form of the Stokes parameters	7
2.4. Stokes vector	10
2.5. Orientation angle of the polarization ellipse	13
3. Theoretical background	17
3.1. Early polarization studies	17
3.2. Pulsar magnetosphere	20
3.2.1. Goldreich-Julian model	20
3.2.2. Orthogonal rotator	25
3.2.3. Oblique rotator	26
3.3. Rotating vector model	28
3.4. Curvature radiation	32
3.5. Interpulse studies	34
4. Emission beam geometry of PSR J2007+2722	37
4.1. Previous studies of PSR J2007+2722	37
4.1.1. Pulse profile	37
4.1.2. Polarization studies	39
4.2. Discussion	45
4.2.1. Disregard the bump at 2000MHz	45
4.2.2. Extending the RVM with interpulse	46
4.2.3. Background radiation model	49
5. Conclusion	57
A. Symmetric and antisymmetric functions	I
B. Additional calculations	IV
C. Codes	VII
6. Bibliography	XXV

List of Figures

2.1.	Components of the electric field	4
2.2.	Resulting electric field vector	11
2.3.	Rotated polarization ellipse	14
3.1.	Plane of polarization	18
3.2.	Difference in position angle at different frequencies	19
3.3.	Possible model for PSR B0833-45	20
3.4.	Pulsar geometry	29
3.5.	Depiction of $\zeta = \alpha + \beta$ and the emission cone geometry	30
3.6.	Projection of the magnetic axis onto the plane of the sky	31
3.7.	Geometry of the coherent curvature radiation mechanism	33
3.8.	Illustration of various plasma velocities and accelerations	35
4.1.	Observing frequency evolution of the pulse profile of PSR J2007+2722 . .	38
4.2.	Stokes profiles and polarization position angles at 1500 and 2000 MHz . .	40
4.3.	Emission beam geometry of PSR J2007+2722 at 1500 MHz	42
4.4.	Reduced χ^2 values as a function of (α, ζ) at 1500 MHz (RVM)	43
4.5.	Reduced χ^2 values as a function of (α, ζ) at 2000 MHz (RVM)	44
4.6.	Polarization position angle for a selected data set at 2000 MHz (RVM) . .	47
4.7.	Reduced χ^2 values for a selected data set at 2000 MHz (RVM)	48
4.8.	Superposition of electric field vectors	51
4.9.	Reduced χ^2 values as a function of (α, ζ) at 1500 MHz (BRM)	52
4.10.	Reduced χ^2 values as a function of (α, ζ) at 2000 MHz (BRM)	53
4.11.	Polarization position angles at 1500 and 2000 MHz (BRM)	54
4.12.	Reduced χ^2 values for a selected data set at 2000 MHz (BRM)	55
4.13.	Polarization position angle for a selected data set at 2000 MHz (BRM) . .	56

List of Tables

4.1.	The best-fit RVM parameters for PSR J2007+2722	41
4.2.	The best-fit RVM parameters for a selected data set of PSR J2007+2722 .	47
4.3.	The best-fit BRM parameters for PSR J2007+2722	51
4.4.	The best-fit BRM parameters for a selected data set of PSR J2007+2722	56

1. Introduction

If you can't explain it simply, you don't understand it well enough.

(Albert Einstein, physicist)

Even though astronomy is one of the oldest fields of science, huge progress has been made over the last decades. Especially the new possibilities of exoatmospheric satellite telescopes open a new observation window. Meanwhile, the astronomical observations, which were restricted to the optical wavelength range until less than 60 years ago, cover a wide range of the electromagnetic spectrum. Besides the common observations via radio telescopes, these days it is possible to observe astronomical objects via X-rays and gamma-rays. This thesis focus on the polarization of the radio pulsar radiation.

Radio pulsars (pulsating source of radio emission) are rapidly rotating, highly magnetized neutron stars, which emit radiation along the magnetic poles. In general, the magnetic axis is not aligned with the rotation axis. If the emitted beam passes lighthouse-like across the earth, the observatories on and around Earth can measure the nearly periodic signal. Although observations have shown that most pulses of the radio pulsar are almost completely linearly polarized, radio pulsars are unique and versatile objects that can be used to study an extremely wide range of physical and astrophysical problems [12].

One essential aspect of this thesis is the polarization of electromagnetic radiation, which is described in Chapter 2. With the aid of the polarization ellipse (see Section 2.1), the Stokes vector, which is a set of Stokes polarization parameters, is derived in Section 2.2. Additionally, the Stokes vector can be expressed in terms of components of a complex electric field as well as in terms of intensities (see Section 2.3 and 2.4). The orientation angle of the polarization ellipse is derived in Section 2.5 and identified with the position angle of linear polarization ψ of the *rotating vector model* (RVM).

In Chapter 3, the theoretical background of radio pulsar astronomy is elaborated and the most common pulsar models are presented. When an observer receives electromagnetic radiation from astronomical objects, the first questions to face are "*Where does the charged particles come from? What accelerates them? What is the emission mechanism?*". Therefore the pulsar electrodynamics, especially the pulsar magnetosphere, is described in Section 3.2. Plasma is extracted from the neutron star surface and accelerated along the open magnetic field lines. The most likely emission mechanism is curvature radiation (see Section 3.4). Since the radiation is linearly polarized, the RVM, which is essential for this thesis, is introduced in Section 3.3. The emission beam geometry of a pulsar is determined by the RVM.

The main purpose of this project is to understand and explain the polarization position

angle curve of PSR J2007+2722 (see Figure 4.2). In Chapter 4, the theoretical knowledge of Chapter 2 and 3 is applied to pulse polarization data of PSR J2007+2722. The emission beam geometry of the pulsar is determined by the RVM (see Section 4.1). However, the RVM only describes the data to a certain degree, so new attempts to improve the RVM are carried out in Section 4.2.

2. Polarization

Before studying the theoretical background of radio pulsar astronomy, it is necessary to understand explicitly the fundamentals of polarization. Since the *rotating vector model* (RVM), which will be the most important pulsar model in this thesis, is based on polarization studies, the polarization of electromagnetic radiation is described in this chapter.

In Section 2.1, the electric field of an electromagnetic plane wave is used to derive the polarization ellipse. Moreover, the physical meaning of the polarization ellipse is explained. Depending on the properties of the electric field, the polarization ellipse degenerates to special forms [7].

A more common way of describing the polarization state of electromagnetic radiation is the Stokes vector, which is a set of Stokes polarization parameters (see Section 2.2). The polarization degree of a light beam can be deduced by the Stokes polarization parameters. In Section 2.3 and 2.4, the Stokes vector is expressed in terms of components of a complex electric field as well as in terms of intensities. Supplementary, the complex representation of electric fields is elaborated [7, 23].

The RVM is a quantitative prediction of the polarization position angle ψ . This angle is identified with the orientation angle of the polarization ellipse, which is derived in Section 2.5. Since the orientation angle of the polarization ellipse is expressed in terms of the first and second Stokes polarization parameters, a radio telescope measures the Stokes polarization parameters of the radiation to calculate the experimental ψ as a function of rotational phase ϕ . In Chapter 4, the theoretical curve ψ_{RVM} is compared with the measured ψ of PSR J2007+2722. This procedure leads to the emission beam geometry of PSR J2007+2722 (see Figure 4.3) [7, 12].

2.1. Polarization ellipse

The polarization of a transverse wave such as electromagnetic radiation specifies the geometrical orientation of its oscillation. By convention the polarization of an electromagnetic plane wave refers to the oscillation of the electric field \vec{E} . The components of the electric field E_x , E_y and E_z are depicted on the left hand side of Figure 2.1. The transverse components are represented by

$$E_x(z, t) = E_{0x} \cos(\tau + \delta_x), \quad (2.1)$$

$$E_y(z, t) = E_{0y} \cos(\tau + \delta_y), \quad (2.2)$$

where $\tau = \omega t - kz$ is called the propagator. E_{0x} and E_{0y} are the maximum amplitudes and δ_x and δ_y are the corresponding phases. The resulting electric field vector is given

by

$$\vec{E}(z, t) = \vec{e}_x \cdot E_{0x} \cos(\tau + \delta_x) + \vec{e}_y \cdot E_{0y} \cos(\tau + \delta_y). \quad (2.3)$$

In the following, the dependence of the electric field and their components are omitted [7].

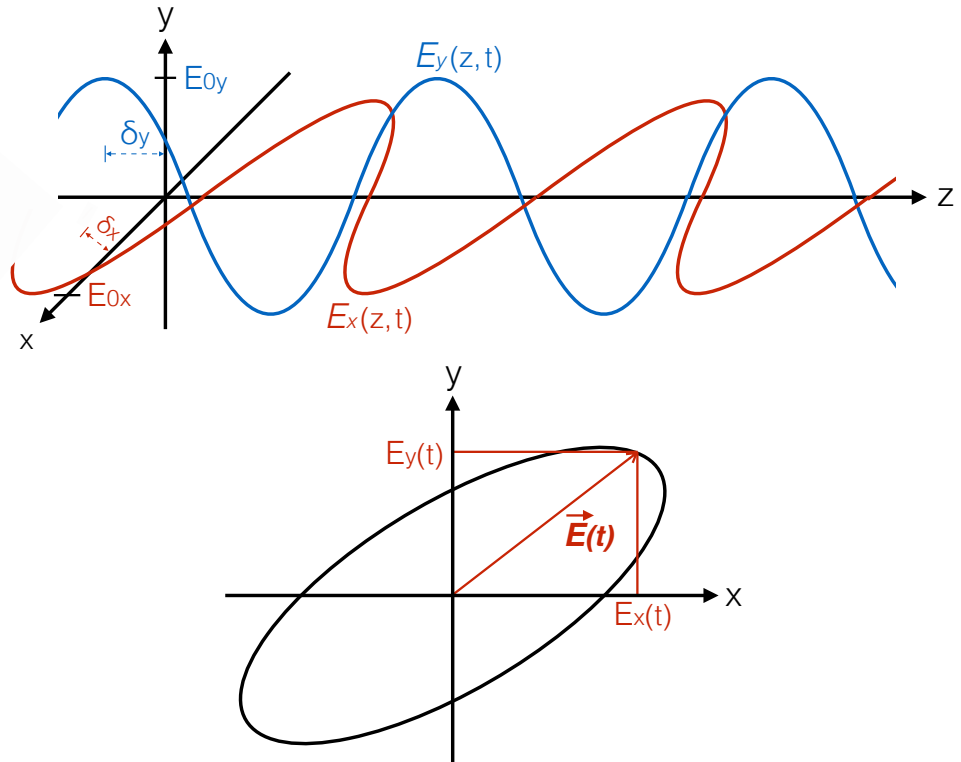


Figure 2.1.: The upper panel shows the propagation of the components of the electric field in the z direction. It is an illustration of Equations 2.1 and 2.2. The arbitrary phases satisfy $\delta_x \neq \delta_y \neq 0$. In the lower panel, the resulting electric field vector $\vec{E}(t)$ is rotated in the xy -plane by setting $z = 0$. The overall shape of this figure is elliptical.

The goal of this section is the derivation of the polarization ellipse. Therefore Equations 2.1 and 2.2 are written as

$$\frac{E_x}{E_{0x}} = \cos \tau \cos \delta_x - \sin \tau \sin \delta_x, \quad (2.4)$$

$$\frac{E_y}{E_{0y}} = \cos \tau \cos \delta_y - \sin \tau \sin \delta_y, \quad (2.5)$$

using the trigonometric formula $\cos(x \pm y) = \cos x \cos y \mp \sin x \sin y$. Hence,

$$\begin{aligned} \frac{E_x}{E_{0x}} \sin \delta_y - \frac{E_y}{E_{0y}} \sin \delta_x &= \cos \tau \cos \delta_x \sin \delta_y - \sin \tau \sin \delta_x \sin \delta_y \\ &\quad - (\cos \tau \cos \delta_y \sin \delta_x - \sin \tau \sin \delta_y \sin \delta_x) \quad (2.6) \\ &= \cos \tau (\cos \delta_x \sin \delta_y - \cos \delta_y \sin \delta_x) \\ &= \cos \tau \sin(\delta_y - \delta_x) \end{aligned}$$

$$\frac{E_x}{E_{0x}} \cos \delta_y - \frac{E_y}{E_{0y}} \cos \delta_x = \sin \tau \sin(\delta_y - \delta_x). \quad (2.7)$$

Squaring and adding Equations 2.6 and 2.7 gives the Equation of the polarization ellipse

$$\frac{E_x^2}{E_{0x}^2} + \frac{E_y^2}{E_{0y}^2} - 2 \frac{E_x E_y}{E_{0x} E_{0y}} \cos \delta = \sin^2 \delta, \quad (2.8)$$

where $\delta = \delta_y - \delta_x$ is the phase difference [7].

The electromagnetic wave assumes special shapes of polarization for certain values of E_{0x} , E_{0y} and δ . Thus, the polarization ellipse (Equation 2.8) degenerates to special forms:

1. The resulting electric field vector oscillates only in the x direction for a *horizontally linearly polarized wave*. Therefore, $E_{0y} = 0$ and $E_{0x} \neq 0$. If $E_{0x} = 0$ and $E_{0y} \neq 0$, the wave is *vertically linearly polarized* and it oscillates only in the y direction [7].
2. Setting $\delta = 0$ or $\delta = \pi$ leads to a reduction of the Equation 2.8 to

$$\frac{E_x^2}{E_{0x}^2} + \frac{E_y^2}{E_{0y}^2} \pm \frac{E_x E_y}{E_{0x} E_{0y}} = \left(\frac{E_x}{E_{0x}} \pm \frac{E_y}{E_{0y}} \right)^2 = 0. \quad (2.9)$$

Applying the condition $E_{0x} = E_{0y} = E_0$ on Equation 2.9 results in

$$E_y = \pm E_x. \quad (2.10)$$

The positive case of Equation 2.10 represents the $+45^\circ$ *linearly polarized wave*, and the negative case represents the -45° *linearly polarized wave* [7].

3. If $\delta = \frac{\pi}{2}$ or $\frac{3\pi}{2}$, Equation 2.8 reduces to

$$\frac{E_x^2}{E_{0x}^2} + \frac{E_y^2}{E_{0y}^2} = 1. \quad (2.11)$$

This is the standard equation of an ellipse, which means that the wave is *elliptically polarized*. Going one step further by setting $E_{0x} = E_{0y} = E_0$ leads to the equation of a circle:

$$\frac{E_x^2}{E_0^2} + \frac{E_y^2}{E_0^2} = 1. \quad (2.12)$$

The wave is *right circularly polarized* for $\delta = \frac{\pi}{2}$ and *left circularly polarized* for $\delta = \frac{3\pi}{2}$ [7].

2.2. Derivation of the Stokes polarization parameters

To describe the polarization state of electromagnetic radiation, the Stokes vector \vec{S} , a set of parameters, is introduced. The only time-dependent variables in Equation 2.8 are E_x and E_y . Taking the time average of Equation 2.8 and multiplying by $4E_{0x}^2 E_{0y}^2$ yields

$$4E_{0y}^2 \langle E_x^2(t) \rangle + 4E_{0x}^2 \langle E_y^2(t) \rangle - 8E_{0x}E_{0y} \langle E_x(t)E_y(t) \rangle \cos \delta = (2E_{0x}E_{0y} \sin \delta)^2. \quad (2.13)$$

The average values of Equation 2.13 can be computed as follows:

$$\begin{aligned} \langle E_x^2(t) \rangle &= \langle E_{0x}^2 \cos^2 \tau \rangle \\ &= \frac{1}{2} E_{0x}^2, \end{aligned} \quad (2.14)$$

$$\begin{aligned} \langle E_y^2(t) \rangle &= \langle E_{0y}^2 \cos^2(\tau + \delta) \rangle \\ &= \frac{1}{2} E_{0y}^2, \end{aligned} \quad (2.15)$$

$$\begin{aligned} \langle E_x(t)E_y(t) \rangle &= \langle E_{0x} \cos \tau E_{0y} \cos(\tau + \delta) \rangle \\ &= E_{0x}E_{0y} \langle \cos^2 \tau \cos \delta - \cos \tau \sin \tau \sin \delta \rangle \\ &= \frac{1}{2} E_{0x}E_{0y} \cos \delta. \end{aligned} \quad (2.16)$$

Substituting Equations 2.14, 2.15 and 2.16 into Equation 2.13 gives

$$4E_{0x}^2 E_{0y}^2 - (2E_{0x}E_{0y} \cos \delta)^2 = (2E_{0x}E_{0y} \sin \delta)^2. \quad (2.17)$$

With the auxiliary calculation $(E_{0x}^2 + E_{0y}^2)^2 - (E_{0x}^2 - E_{0y}^2)^2 = E_{0x}^4 + E_{0y}^4 + 2E_{0x}^2 E_{0y}^2 - E_{0x}^4 - E_{0y}^4 + 2E_{0x}^2 E_{0y}^2 = 4E_{0x}^2 E_{0y}^2$, Equation 2.17 yields to the final expression of

$$\underbrace{(E_{0x}^2 + E_{0y}^2)^2}_{\equiv S_0} - \underbrace{(E_{0x}^2 - E_{0y}^2)^2}_{\equiv S_1} - \underbrace{(2E_{0x}E_{0y} \cos \delta)^2}_{\equiv S_2} = \underbrace{(2E_{0x}E_{0y} \sin \delta)^2}_{\equiv S_3}. \quad (2.18)$$

The quantities inside the parentheses of Equation 2.18 are defined as the Stokes parameters for a plane wave as follows

$$\vec{S} = \begin{pmatrix} S_0 \\ S_1 \\ S_2 \\ S_3 \end{pmatrix} = \begin{pmatrix} E_{0x}^2 + E_{0y}^2 \\ E_{0x}^2 - E_{0y}^2 \\ 2E_{0x}E_{0y} \cos \delta \\ 2E_{0x}E_{0y} \sin \delta \end{pmatrix} \quad (2.19)$$

and Equation 2.18 results in

$$S_0^2 = S_1^2 + S_2^2 + S_3^2. \quad (2.20)$$

The first Stokes parameter S_0 is the total intensity of the light. The second and third Stokes parameter S_1 and S_2 particularizes the linear polarization. S_1 describes the amount of linear horizontal or vertical polarization and S_2 describes the amount of linear $+45^\circ$ or -45° polarization. The forth Stokes parameter S_3 describes the amount of right and left circular polarization [7].

A light beam is a superposition of several plane waves. Every single plane wave obeys Equations 2.18, 2.19 and 2.20. However, the superposition of several plane waves will lead to the following relation of the Stokes parameters:

$$S_0^2 \geq S_1^2 + S_2^2 + S_3^2. \quad (2.21)$$

If the light beam is completely polarized, Equation 2.21 is an equality. On the other hand, it is an inequality, if the light beam is partially polarized or unpolarized. Going one step further, the degree of polarization Π for any state of polarization is defined by

$$\Pi = \frac{I_{pol}}{I_{tot}} = \frac{\sqrt{S_1^2 + S_2^2 + S_3^2}}{S_0}, \quad (2.22)$$

where I_{tot} is the total intensity of the light beam and I_{pol} is the intensity of the sum of the polarization components. The degree of polarization Π obeys the condition $0 \leq \Pi \leq 1$ [7].

2.3. Complex form of the Stokes parameters

In this section, the Stokes parameters are expressed in terms of components of a complex electric field. The complex representation of electromagnetic fields has to be elaborated explicitly, before defining the complex form of the Stokes parameters for a plane wave and showing the equality to Equation 2.19.

The Fourier transform of a real (physically measurable) electric field $E(z=0, t)$, from now on written as $E(t)$, is a complex function

$$(\mathcal{F}E)(\omega) \equiv \tilde{E}(\omega) = \frac{1}{\sqrt{2\pi}} \int_{-\infty}^{+\infty} E(t) \exp(-i\omega t) dt \quad (2.23)$$

in the frequency domain defined for frequencies $-\infty < \omega < +\infty$. For reasons of simplification there is only one component used instead of the field vector. The original electric field $E(t)$ can be reconstructed from $\tilde{E}(\omega)$ with the *Fourier inversion theorem* as follows

$$E(t) = \frac{1}{\sqrt{2\pi}} \int_{-\infty}^{+\infty} \tilde{E}(\omega) \exp(i\omega t) d\omega. \quad (2.24)$$

Note that Equation 2.30 shows that $E(t)$ is real [23].

Taking the complex conjugate of Equation 2.23 ($E(t)$ is real), the relation follows

$$\tilde{E}(\omega) = \tilde{E}^*(-\omega). \quad (2.25)$$

Since $\tilde{E}(\omega)$ is a complex function, $\tilde{E}(\omega)$ can be separated into a real part $\tilde{E}^R(\omega)$ and an imaginary part $\tilde{E}^I(\omega)$ as follows

$$\tilde{E}(\omega) = \tilde{E}^R(\omega) + i\tilde{E}^I(\omega). \quad (2.26)$$

The right side of Equation 2.25 gives

$$\tilde{E}^*(-\omega) = \tilde{E}^R(-\omega) - i\tilde{E}^I(-\omega). \quad (2.27)$$

Comparing Equations 2.26 and 2.27 with respect to Equation 2.25 results in

$$\tilde{E}^R(\omega) = \tilde{E}^R(-\omega), \quad (2.28)$$

$$\tilde{E}^I(\omega) = -\tilde{E}^I(-\omega). \quad (2.29)$$

The Definition A.1 in Appendix A implies that the real part $\tilde{E}^R(\omega)$ is symmetric/even and the imaginary part $\tilde{E}^I(\omega)$ is antisymmetric/odd. It is difficult to imagine negative frequencies in a physical way, because the frequency is defined as the number of oscillations per second. But negative frequencies are required, so that the original electric field $E(t)$ is real in the time domain [23].

To show that $E(t)$ is real in the time domain, the properties of symmetric and antisymmetric functions are used. In Appendix A, the Theorem A.5 ($\int_{-a}^a f_{sym}(x) dx = 2 \cdot \int_0^a f_{sym}(x) dx$) and the Theorem A.6 ($\int_{-a}^a f_{asym}(x) dx = 0$) are mathematically proven. Moreover, it is shown that the product of two symmetric functions and the product of two antisymmetric functions are symmetric functions (Corollary A.2 and A.3). While the Corollary A.4 says that a product of a symmetric and an antisymmetric function is an antisymmetric function. The cosine is a symmetric function ($\cos x = \cos(-x)$) and the sine is an antisymmetric function ($\sin x = -\sin(-x)$). Thus,

$$\begin{aligned} E(t) &= \frac{1}{\sqrt{2\pi}} \int_{-\infty}^{+\infty} \tilde{E}(\omega) \exp(i\omega t) d\omega \\ &= \frac{1}{\sqrt{2\pi}} \int_{-\infty}^{+\infty} \left[\tilde{E}^R(\omega) \cos(\omega t) + i\tilde{E}^I(\omega) \cos(\omega t) + i\tilde{E}^R(\omega) \sin(\omega t) - \tilde{E}^I(\omega) \sin(\omega t) \right] d\omega \\ &= \frac{2}{\sqrt{2\pi}} \int_{-\infty}^{+\infty} \left[\tilde{E}^R(\omega) \cos(\omega t) - \tilde{E}^I(\omega) \sin(\omega t) \right] d\omega. \end{aligned} \quad (2.30)$$

In the first step, Equation 2.26 is expanded with the *Euler's formula* $\exp(ix) = \cos x + i \sin x$ [23].

One way to avoid negative frequencies is to define a new function $\tilde{E}^+(\omega)$, that discards the negative frequency component and doubling the positive frequency component:

$$\tilde{E}^+(\omega) = \begin{cases} 0 & \text{if } \omega \leq 0 \\ 2\tilde{E}(\omega) & \text{if } \omega > 0. \end{cases} \quad (2.31)$$

As a consequence, the inverse transform of $\tilde{E}^+(\omega)$, written as $E^+(t)$, is complex in the time domain. Calculating $E^+(t)$ with the theorems and corollaries of Appendix A leads

to

$$\begin{aligned}
E^+(t) &= \frac{1}{\sqrt{2\pi}} \int_{-\infty}^{+\infty} \tilde{E}^+(\omega) \exp(i\omega t) d\omega \\
&= \frac{1}{\sqrt{2\pi}} \int_0^{+\infty} 2\tilde{E}(\omega) \exp(i\omega t) d\omega \\
&= \frac{2}{\sqrt{2\pi}} \int_0^{+\infty} [\tilde{E}^R(\omega) \cos(\omega t) - \tilde{E}^I(\omega) \sin(\omega t)] d\omega \\
&\quad + \frac{2i}{\sqrt{2\pi}} \int_0^{+\infty} [\tilde{E}^I(\omega) \cos(\omega t) + \tilde{E}^R(\omega) \sin(\omega t)] d\omega \\
&= E(t) + \frac{2i}{\sqrt{2\pi}} \int_0^{+\infty} [\tilde{E}^I(\omega) \cos(\omega t) + \tilde{E}^R(\omega) \sin(\omega t)] d\omega.
\end{aligned} \tag{2.32}$$

Equation 2.32 implies an important relationship between the complex field $E^+(t)$ and the original electric field $E(t)$ as follows

$$E(t) = \Re\{E^+(t)\}. \tag{2.33}$$

Taking the real part of the complex field $E^+(t)$ gives the original electric field $E(t)$. The imaginary part of $E^+(t)$ is a function, where the cos and sin components are shifted by $\frac{\pi}{2}$ in phase towards the components of the real part [23].

The properties of the complex field $E^+(t)$ above conclude that $E^+(t)$ is defined by

$$E_x^+(t) = E_{0x} \exp[i(\omega t + \delta_x)], \tag{2.34}$$

$$E_y^+(t) = E_{0y} \exp[i(\omega t + \delta_y)]. \tag{2.35}$$

To check the consistency of the field definitions, the complex field $E^+(t)$ (Equations 2.34 and 2.35) have to become Equations 2.1 and 2.2, when applying the condition of Equation 2.33:

$$E_x(z=0, t) = \Re\{E_x^+(t)\} = \Re\{E_{0x} \exp[i(\omega t + \delta_x)]\} = E_{0x} \cos(\omega t + \delta_x), \tag{2.36}$$

$$E_y(z=0, t) = \Re\{E_y^+(t)\} = \Re\{E_{0y} \exp[i(\omega t + \delta_y)]\} = E_{0y} \cos(\omega t + \delta_y). \tag{2.37}$$

In addition, the imaginary part of $E^+(t)$ has to be shifted by $\frac{\pi}{2}$ in phase towards $\Im\{E^+(t)\}$. The components of the imaginary part of $E^+(t)$ are

$$\Im\{E_x^+(t)\} = \Im\{E_{0x} \exp[i(\omega t + \delta_x)]\} = E_{0x} \sin(\omega t + \delta_x), \tag{2.38}$$

$$\Im\{E_y^+(t)\} = \Im\{E_{0y} \exp[i(\omega t + \delta_y)]\} = E_{0y} \sin(\omega t + \delta_y). \tag{2.39}$$

Since $\sin(x + \frac{\pi}{2}) = \cos(x)$, the consistency of the definitions is shown. In the following, the complex representation is used and $E^+(t)$ is written as $E(t)$ [7, 23].

Using the *Euler's formula* $\exp(ix) = \cos x + i \sin x$ and $\delta = \delta_y - \delta_x$, the complex form

of the Stokes parameters for a plane wave is obtained as follows

$$\begin{aligned} S_0 &\equiv E_x E_x^* + E_y E_y^* = E_{0x}^2 \exp[i(\omega t + \delta_x) - i(\omega t + \delta_x)] \\ &\quad + E_{0y}^2 \exp[i(\omega t + \delta_y) - i(\omega t + \delta_y)] \\ &= E_{0x}^2 + E_{0y}^2, \end{aligned} \quad (2.40)$$

$$\begin{aligned} S_1 &\equiv E_x E_x^* - E_y E_y^* = E_{0x}^2 \exp[i(\omega t + \delta_x) - i(\omega t + \delta_x)] \\ &\quad - E_{0y}^2 \exp[i(\omega t + \delta_y) - i(\omega t + \delta_y)] \\ &= E_{0x}^2 - E_{0y}^2, \end{aligned} \quad (2.41)$$

$$\begin{aligned} S_2 &\equiv E_x E_y^* + E_y E_x^* = E_{0x} E_{0y} (\exp[i(\omega t + \delta_x) - i(\omega t + \delta_y)] \\ &\quad + \exp[i(\omega t + \delta_y) - i(\omega t + \delta_x)]) \\ &= E_{0x} E_{0y} (\cos \delta - i \sin \delta + \cos \delta + i \sin \delta) \\ &= 2E_{0x} E_{0y} \cos \delta, \end{aligned} \quad (2.42)$$

$$\begin{aligned} S_3 &\equiv i(E_x E_y^* - E_y E_x^*) = iE_{0x} E_{0y} (\exp[i(\omega t + \delta_x) - i(\omega t + \delta_y)] \\ &\quad - \exp[i(\omega t + \delta_y) - i(\omega t + \delta_x)]) \\ &= iE_{0x} E_{0y} (\cos \delta - i \sin \delta - \cos \delta - i \sin \delta) \\ &= 2E_{0x} E_{0y} \sin \delta. \end{aligned} \quad (2.43)$$

Taking the real and imaginary part of $E_x^* E_y = E_{0x} E_{0y} \exp(i\delta)$ gives $2\Re\{E_x^* E_y\} = 2E_{0x} E_{0y} \cos \delta$ and $2\Im\{E_x^* E_y\} = 2E_{0x} E_{0y} \sin \delta$. This implies the Stokes vector

$$\vec{S} = \begin{pmatrix} S_0 \\ S_1 \\ S_2 \\ S_3 \end{pmatrix} = \begin{pmatrix} E_x E_x^* + E_y E_y^* \\ E_x E_x^* - E_y E_y^* \\ E_x E_y^* + E_y E_x^* \\ i(E_x E_y^* - E_y E_x^*) \end{pmatrix} = \begin{pmatrix} E_x E_x^* + E_y E_y^* \\ E_x E_x^* - E_y E_y^* \\ 2\Re\{E_x^* E_y\} \\ 2\Im\{E_x^* E_y\} \end{pmatrix} \quad (2.44)$$

in terms of a complex electric field [7].

2.4. Stokes vector

The next goal is to calculate the Stokes vector $\vec{S}_{lin,\alpha}$ of an α -linearly polarized wave. A wave is linearly polarized, when $\delta = 0$ or $\delta = \pi$. If $\delta = 0$, α_1 complies the condition $0 \leq \alpha_1 \leq \frac{\pi}{2}$ (see Figure 2.2) and if $\delta = \pi$, α_2 complies the condition $\frac{\pi}{2} \leq \alpha_2 \leq \pi$. The resulting electric field vector $\vec{E}_{\alpha_1}(t)$ oscillates linear in the $(+, +)$ and $(-, -)$ quadrants and $\vec{E}_{\alpha_2}(t)$ in the $(+, -)$ and $(-, +)$ quadrants. The total intensity is defined as $I_0 \equiv 2E_0^2$. The determination of the amplitudes

$$E_{0x} = E_0 \cos \alpha_1 = -E_0 \cos \alpha_2, \quad (2.45)$$

$$E_{0y} = E_0 \sin \alpha_1 = E_0 \sin \alpha_2 \quad (2.46)$$

is demonstrated in Figure 2.2 [7].

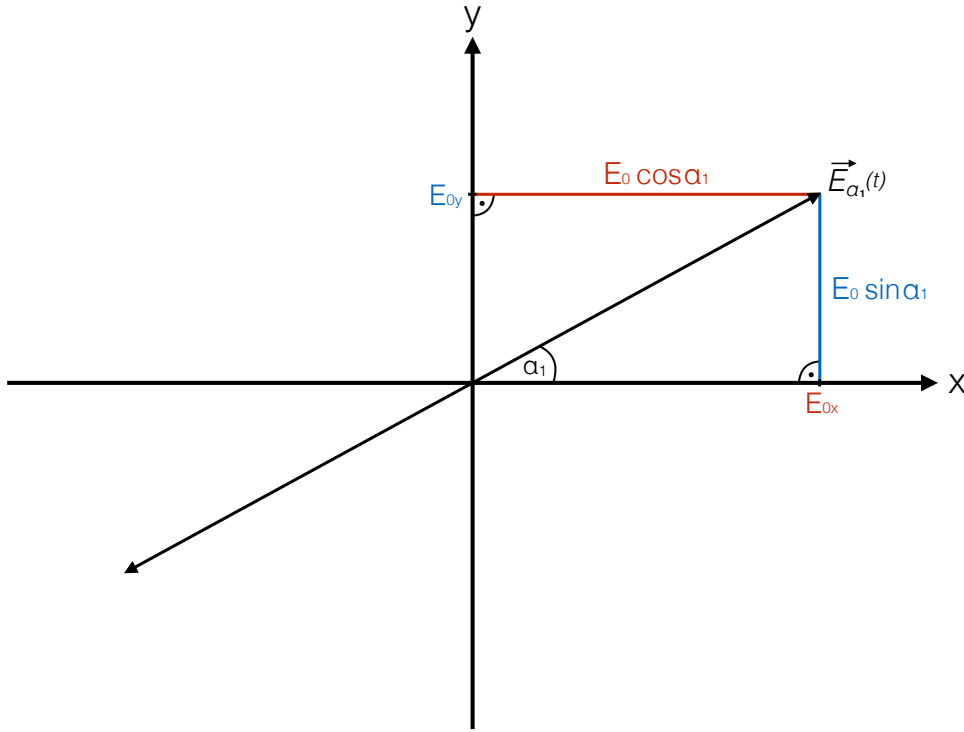


Figure 2.2.: This figure demonstrates a resulting electric field vector $\vec{E}_{\alpha_1}(t)$ of an α_1 -linearly polarized wave. The determination of the amplitudes E_{0x} and E_{0y} is delineated in the coordinate system.

Everything is set up for computing the Stokes vectors \vec{S}_{lin,α_1} and \vec{S}_{lin,α_2} :

$$\vec{S}_{lin,\alpha_1} = \begin{pmatrix} (E_0 \cos \alpha_1)^2 + (E_0 \sin \alpha_1)^2 \\ (E_0 \cos \alpha_1)^2 - (E_0 \sin \alpha_1)^2 \\ 2(E_0 \cos \alpha_1)(E_0 \sin \alpha_1) \\ 0 \end{pmatrix} = I_0 \begin{pmatrix} 1 \\ \cos 2\alpha_1 \\ \sin 2\alpha_1 \\ 0 \end{pmatrix}, \quad (2.47)$$

$$\vec{S}_{lin,\alpha_2} = \begin{pmatrix} (-E_0 \cos \alpha_2)^2 + (E_0 \sin \alpha_2)^2 \\ (-E_0 \cos \alpha_2)^2 - (E_0 \sin \alpha_2)^2 \\ -2(-E_0 \cos \alpha_2)(E_0 \sin \alpha_2) \\ 0 \end{pmatrix} = I_0 \begin{pmatrix} 1 \\ \cos 2\alpha_2 \\ \sin 2\alpha_2 \\ 0 \end{pmatrix}. \quad (2.48)$$

The Stokes vector $\vec{S}_{lin,\alpha}$ of an α -linearly polarized wave is

$$\vec{S}_{lin,\alpha} = I_0 \begin{pmatrix} 1 \\ \cos 2\alpha \\ \sin 2\alpha \\ 0 \end{pmatrix}, \quad (2.49)$$

where $0 \leq \alpha \leq \pi$. The Stokes vector yields to

$$\vec{S}_{\text{lin,hor}} = I_0 \begin{pmatrix} 1 \\ 1 \\ 0 \\ 0 \end{pmatrix}, \vec{S}_{\text{lin,ver}} = I_0 \begin{pmatrix} 1 \\ -1 \\ 0 \\ 0 \end{pmatrix} \text{ and } \vec{S}_{\text{lin,}\pm 45^\circ} = I_0 \begin{pmatrix} 1 \\ 0 \\ \pm 1 \\ 0 \end{pmatrix} \quad (2.50)$$

for linear horizontal ($\alpha = 0$), linear vertical ($\alpha = \frac{\pi}{2}$) and linear $\pm 45^\circ$ polarization ($\alpha = \pm \frac{\pi}{4}$), respectively [7].

The next task is to calculate the Stokes vector $\vec{S}_{\text{ell},\alpha}$ of an α -elliptically polarized wave. The shape and orientation of the ellipse depends on the arbitrary phase difference $\delta \in [0, 2\pi]$ and the predetermined amplitudes $E_{0x} = E_0 \cos \alpha$ and $E_{0y} = E_0 \sin \alpha$. This implies that Equation 2.19 results in

$$\vec{S}_{\text{ell},\alpha} = \begin{pmatrix} (E_0 \cos \alpha)^2 + (E_0 \sin \alpha)^2 \\ (E_0 \cos \alpha)^2 - (E_0 \sin \alpha)^2 \\ 2(E_0 \cos \alpha)(E_0 \sin \alpha) \cos \delta \\ 2(E_0 \cos \alpha)(E_0 \sin \alpha) \sin \delta \end{pmatrix} = I_0 \begin{pmatrix} 1 \\ \cos 2\alpha \\ \sin(2\alpha) \cos \delta \\ \sin(2\alpha) \sin \delta \end{pmatrix}. \quad (2.51)$$

Special forms of elliptical polarization are the right circular polarization ($\delta = \frac{\pi}{2}$, $E_{0x} = E_{0y} = E_0$) and the left circular polarization ($\delta = \frac{3\pi}{2}$, $E_{0x} = E_{0y} = E_0$). The Stokes vector yields to

$$\vec{S}_{\text{right circ (+), left circ (-)}} = \begin{pmatrix} E_0^2 + E_0^2 \\ E_0^2 - E_0^2 \\ 2E_0^2 \cos \delta \\ 2E_0^2 \sin \delta \end{pmatrix} = I_0 \begin{pmatrix} 1 \\ 0 \\ 0 \\ \pm 1 \end{pmatrix} \quad (2.52)$$

for these two cases [7].

The intensity of the light beam is given by

$$I = |E|^2 = EE^*. \quad (2.53)$$

The amplitude of a linearly polarized light beam in the x and the y direction is E_x and E_y , respectively. Rotating the coordinate system by -45° leads to the amplitudes E_{-45° and E_{+45° of a $\mp 45^\circ$ linearly polarized light beam. Expressing the amplitudes in terms of E_x and E_y :

$$\begin{pmatrix} E_{-45^\circ} \\ E_{+45^\circ} \end{pmatrix} = \begin{pmatrix} \cos(-45^\circ) & \sin(-45^\circ) \\ -\sin(-45^\circ) & \cos(-45^\circ) \end{pmatrix} \begin{pmatrix} E_x \\ E_y \end{pmatrix} = \frac{1}{\sqrt{2}} \begin{pmatrix} E_x - E_y \\ E_x + E_y \end{pmatrix}. \quad (2.54)$$

The amplitudes E_{LC} and E_{RC} of a left and right circularly polarized light beam in terms of E_x and E_y are determined by

$$\begin{pmatrix} E_{LC} \\ E_{RC} \end{pmatrix} = \frac{1}{\sqrt{2}} \begin{pmatrix} 1 & i \\ 1 & -i \end{pmatrix} \begin{pmatrix} E_x \\ E_y \end{pmatrix} = \frac{1}{\sqrt{2}} \begin{pmatrix} E_x + iE_y \\ E_x - iE_y \end{pmatrix}. \quad (2.55)$$

The Stokes parameters are defined in terms of intensities using Equations 2.53, 2.54 and 2.55 as follows:

$$\begin{aligned} S_0 &= I_x + I_y \\ &= E_x E_x^* + E_y E_y^*, \end{aligned} \tag{2.56}$$

$$\begin{aligned} S_1 &\equiv I_x - I_y \\ &= E_x E_x^* - E_y E_y^*, \end{aligned} \tag{2.57}$$

$$\begin{aligned} S_2 &\equiv I_{+45^\circ} - I_{-45^\circ} \\ &= E_{+45^\circ} E_{+45^\circ}^* - E_{-45^\circ} E_{-45^\circ}^* \\ &= \frac{1}{2} [(E_x + E_y)(E_x^* + E_y^*) - (E_x - E_y)(E_x^* - E_y^*)] \\ &= E_x E_y^* + E_y E_x^*, \end{aligned} \tag{2.58}$$

$$\begin{aligned} S_3 &\equiv I_{RC} - I_{LC} \\ &= E_{RC} E_{RC}^* - E_{LC} E_{LC}^* \\ &= \frac{1}{2} [(E_x - iE_y)(E_x^* + iE_y^*) - (E_x + iE_y)(E_x^* - iE_y^*)] \\ &= i(E_x E_y^* - E_y E_x^*). \end{aligned} \tag{2.59}$$

This implies the Stokes vector

$$\vec{S} = \begin{pmatrix} S_0 \\ S_1 \\ S_2 \\ S_3 \end{pmatrix} = \begin{pmatrix} I \\ Q \\ U \\ V \end{pmatrix} = \begin{pmatrix} I_x + I_y \\ I_x - I_y \\ I_{+45^\circ} - I_{-45^\circ} \\ I_{RC} - I_{LC} \end{pmatrix} \tag{2.60}$$

in terms of intensities, where I is the total intensity, $L = \sqrt{Q^2 + U^2}$ is the linearly polarized intensity and V is the circularly polarized intensity [7].

2.5. Orientation angle of the polarization ellipse

In the next chapter, the *rotating vector model* (RVM) is described with a huge impact of the position angle of linear polarization ψ , which is identified with the orientation angle of the polarization ellipse. In Figure 2.3 the rotated ellipse is illustrated. The orientation angle ψ ($0 \leq \psi \leq \pi$) is the angle between x and the direction x' of the major axis of the ellipse. Thus, the components E'_x and E'_y are

$$E_{x'} = E_x \cos \psi + E_y \sin \psi, \tag{2.61}$$

$$E_{y'} = -E_x \sin \psi + E_y \cos \psi. \tag{2.62}$$

Let $2a$ and $2b$ ($a \geq b$) be the lengths of the major and minor axes, respectively. In terms of x' and y' the Equations 2.61 and 2.62 can be written as

$$E_{x'} = a \cos(\tau + \delta'), \tag{2.63}$$

$$E_{y'} = \pm b \sin(\tau + \delta'), \tag{2.64}$$

where τ is a propagator and δ' is an arbitrary phase. In Equation 2.64, the \pm sign describes the two possible senses, in which the endpoint of the field vector is able to describe the ellipse [7].

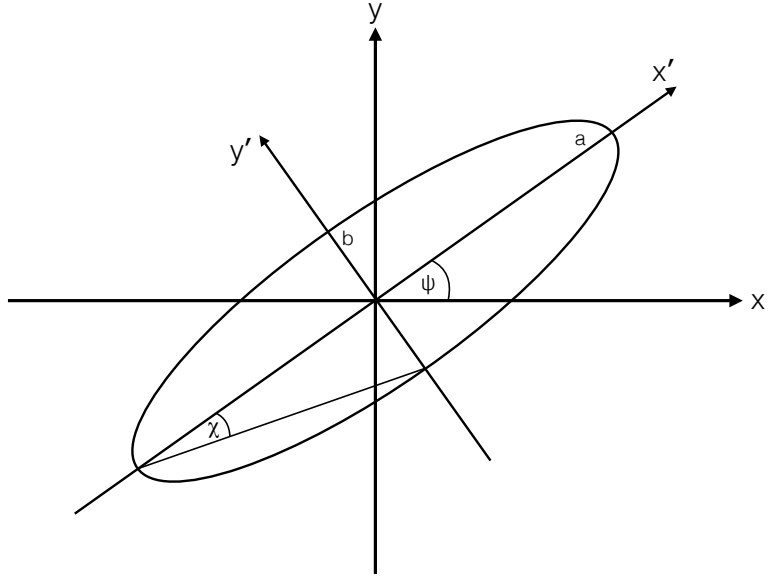


Figure 2.3.: The polarization ellipse is rotated by the orientation angle ψ . The resulting coordinate system is delineated as $(x'; y')$. The length of the major axis is $2a$ and the length of the minor axis is $2b$. The shape of the polarization ellipse depends on the ellipticity angle χ , which modifies the length of the minor axis b .

Substituting Equations 2.63, 2.64, 2.4 and 2.5 into Equations 2.61 and 2.62 leads to

$$a(\cos \tau \cos \delta' - \sin \tau \sin \delta') = E_{0x}(\cos \tau \cos \delta_x - \sin \tau \sin \delta_x) \cos \psi + E_{0y}(\cos \tau \cos \delta_y - \sin \tau \sin \delta_y) \sin \psi, \quad (2.65)$$

$$\pm b(\sin \tau \cos \delta' + \cos \tau \sin \delta') = -E_{0x}(\cos \tau \cos \delta_x - \sin \tau \sin \delta_x) \sin \psi + E_{0y}(\cos \tau \cos \delta_y - \sin \tau \sin \delta_y) \cos \psi. \quad (2.66)$$

By equating the coefficients of $\cos \tau$ and $\sin \tau$ the following equations are obtained:

$$a \cos \delta' = E_{0x} \cos \delta_x \cos \psi + E_{0y} \sin \delta_x \sin \psi, \quad (2.67)$$

$$a \sin \delta' = E_{0x} \sin \delta_x \cos \psi + E_{0y} \sin \delta_y \sin \psi, \quad (2.68)$$

$$\pm b \cos \delta' = E_{0x} \sin \delta_x \sin \psi - E_{0y} \sin \delta_y \cos \psi, \quad (2.69)$$

$$\pm b \sin \delta' = -E_{0x} \cos \delta_x \sin \psi + E_{0y} \cos \delta_y \cos \psi. \quad (2.70)$$

The goal is to express the orientation angle ψ in terms of the Stokes parameters. Therefore Equation 2.67 is divided by 2.68 and Equation 2.69 is divided by 2.70. In Appendix

B, the additional calculation B.1 results in

$$\tan 2\psi = \frac{2E_{0x}E_{0y} \cos \delta}{E_{0x}^2 - E_{0y}^2}. \quad (2.71)$$

The numerator is the second Stokes parameter S_2 and the denominator is the first Stokes parameter S_1 (Equation 2.19). This implies that the position angle of linear polarization can be computed as

$$\psi = \frac{1}{2} \arctan \left(\frac{U}{Q} \right), \quad (2.72)$$

where U and Q are the second Stokes parameter S_2 and the first Stokes parameter S_1 , respectively [7].

3. Theoretical background

After the discovery of the first pulsar PSR B1919+21 in 1967 by J. Bell and A. Hewish [8], many pulsar models have been introduced by several authors. In this chapter, the theoretical background of radio pulsar astronomy is elaborated and the most common pulsar models are presented.

In Section 3.1, the fundamental concept of pulsar radiation is described by taking the studies of polarization properties of the pulsar PSR B0833-45 by V. Radhakrishnan and D. J. Cooke [18] into account. Radhakrishnan and Cooke show that instead of a pulsating source of radiation, the radiation is caused by a steady source at particular regions around the neutron star, which the observer periodically sees. Moreover, they argue that it is reasonable to assume that the magnetic field lines and not the differential Faraday-rotation effects are responsible for the observed pattern of polarization [18].

In 1969, P. Goldreich and W. H. Julian specified the pulsar electrodynamics by showing that the neutron star is not rotating in vacuo [6]. The extraction of plasma from the neutron star surface leads to a plasma-filled surrounding, known as the pulsar magnetosphere, which is derived in Section 3.2 [12]. In 1971, L. Mestel showed that the arguments of Goldreich and Julian for a dense pulsar magnetosphere can be extended to apply to the oblique rotator model [14].

M. M. Komesaroff extended the *rotating vector model* (RVM) by Radhakrishnan and Cooke quantitatively in 1970. The RVM is a quantitative prediction of the polarization position angle ψ and is derived in Section 3.3. As the pulsar rotates, the observer's line of sight encounters different magnetic field lines, which causes the "S"-shaped ψ swing determined by the emission beam geometry of the pulsar [12].

The curvature radiation model, which is a conceivable radiation mechanism for the radio emission, is introduced in Section 3.4. A relativistic flow of plasma moves along the open magnetic field lines and emits radiation in the direction of the plasma velocity. The polarization of the radiation is determined completely by the velocity and acceleration of the radiating particles [1, 3].

3.1. Early polarization studies

The first polarization studies of pulsar radiation were carried out by V. Radhakrishnan and D. J. Cooke [17, 18]. They observed the pulsar PSR B0833-45 at frequencies of 1420, 1720 and 2700 MHz. This pulsar is identified as a possible candidate of the supernova remnant Vela X and is remarkable for its high and constant intensity and complete linear polarization [17, 18].

The polarization of the radiation from pulsars reflects the magnetic field in the region of generation, which will be elucidated later on. The smooth variation over the entire

pulse and the characteristically up and down oscillating amplitude, as sketched in Figure 3.1, is caused by the magnetic field lines. The whole pulse is almost completely linear polarized, which implies that all of the radiation in the pulse was generated in passage through a small region where the field was essentially homogeneous [18].

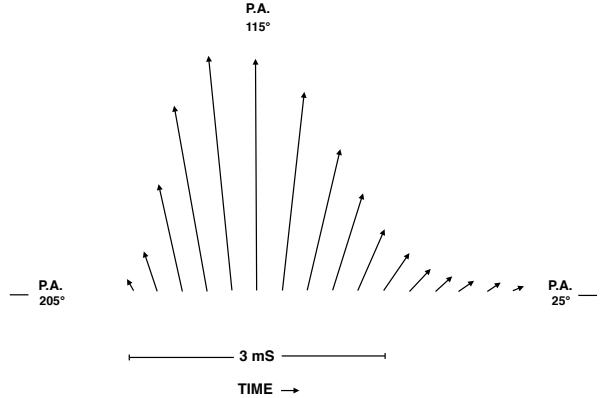


Figure 3.1.: This sketch shows that the plane of polarization shifts uniformly from a position angle PA or ψ (see Section 3.3) near 140° on one edge of the pulse to less than 90° on the other. The length and orientation of the arrows represent the polarized flux and the position angle. This figure originates from [18].

Measuring almost the same polarization for all successive pulses over different days indicates that the same locality in the magnetosphere of the pulsar (see Section 3.2) emits strong radio signals. Either a pulsating source of radiation or a "window", through which one periodically glimpses at a steady source of radiation, is permanently linked to one region in the magnetic field of the neutron star. Due to geometrical circumstances and symmetry considerations, it is very unlikely to associate the radio pulse with a radial oscillation of the star. Even though the period of successive pulses increases with time, which supports the rotation hypothesis [18].

Whenever an electromagnetic wave propagates from its origin through the interstellar medium to the Earth, the polarization of the wave is shifted by

$$\xi = RM \cdot \lambda^2. \quad (3.1)$$

This is referred to as the Faraday rotation and has a dependence on the wavelength(λ)/frequency(f) of the electromagnetic radiation and the rotation measure (RM) of the medium. The rotation measure is given by

$$RM = \frac{e^3}{2\pi m_e^2 c^4} \int_0^d n_e B_{\parallel} dl, \quad (3.2)$$

where B_{\parallel} is the Galactic magnetic field along the line of sight, n_e is the electron number

density, while e and m_e are the charge and mass of an electron, respectively. c is the speed of light and d is the distance from the pulsar to Earth [12, 13].

V. Radhakrishnan and D. J. Cooke [17] stated that the rotation measure RM of PSR B0833-45 is $+42 \text{ rad} \cdot \text{m}^2$. After converting to the same units, the Faraday rotation of the pulsar PSR B0833-45 at 1420 and 1720 MHz yields to $\xi_{1420 \text{ MHz}} = 107^\circ$ and $\xi_{1720 \text{ MHz}} = 73^\circ$. All frequencies were generated with an intrinsic position angle $\psi_{int} = 47^\circ$, hence the position angles of the pulse peak are

$$\psi_{1420 \text{ MHz}} = \psi_{int} + \xi_{1420 \text{ MHz}} = 154^\circ, \quad (3.3)$$

$$\psi_{1720 \text{ MHz}} = \psi_{int} + \xi_{1720 \text{ MHz}} = 120^\circ. \quad (3.4)$$

The difference of 34° in the position angles of polarization at 1420 and 1720 MHz is caused by the Faraday rotation. By removing the 34° mean difference, the effect of the Faraday rotation is eliminated. Figure 3.2 depicts that the difference is constant and close to 34° for the duration of the pulse. It seems reasonable to assume that the magnetic field lines and not the differential Faraday rotation effects were responsible for the observed pattern of polarization. Only the change of the polarization angle with frequency in pulsars is explained by these effects [17].

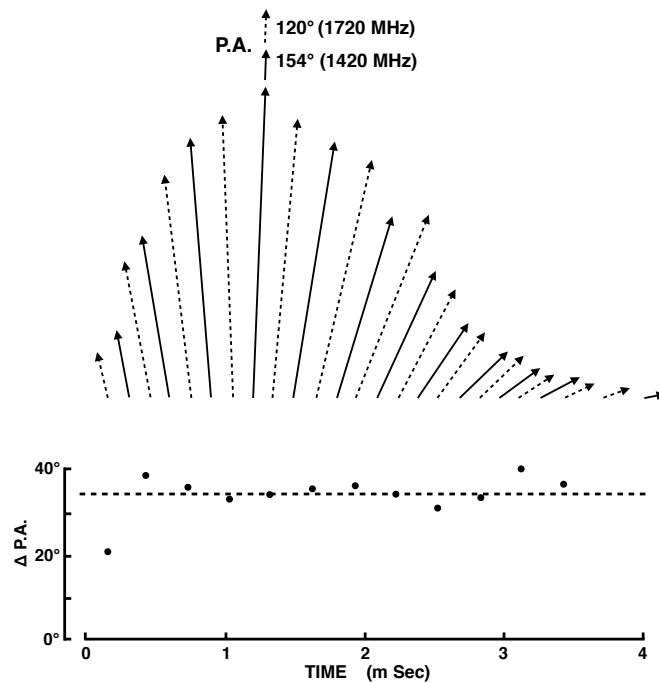


Figure 3.2.: The lower figure shows the difference in position angle at 1420 and 1720 MHz as a function of time. In the upper figure, the plane of polarization at 1420 and 1720 MHz are interleaved by removing the 34° mean difference in the position angle at the two frequencies. This figure originates from [17].

Figure 3.3 depicts a possible model for the pulsar PSR B0833-45. There are two important angles, which influence the structure of the pulse. The first one is the inclination of the magnetic dipole to the rotational axis and declared by α . The second one is declared by β and is the inclination of the line of sight (the line joining the observer) to the magnetic dipole at one particular point, which will be elucidated in Section 3.3. For PSR B0833-45 the angle β is less than 10° . Since there is no interpulse from the other cone in the pattern of the pulse, it is required that α is less than 80° [17].

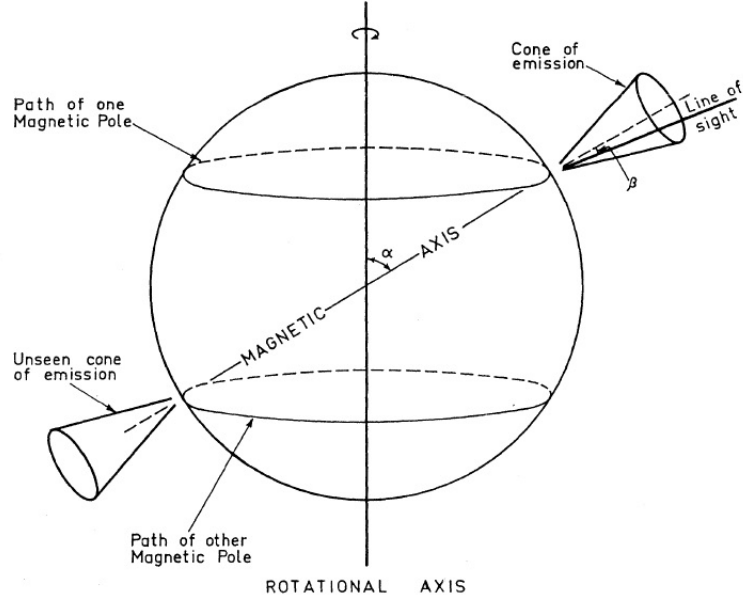


Figure 3.3.: This is a possible model for PSR B0833-45. The magnetic axis differs from the rotational axis by the angle α . Furthermore, the two emission cones (see Section 3.3) are delineated in close proximity to the magnetic dipole. The line of sight is merely included to indicate β . This figure originates from [17].

3.2. Pulsar magnetosphere

3.2.1. Goldreich-Julian model

The first attempt to describe the pulsar magnetosphere was the Goldreich-Julian model. P. Goldreich and W. H. Julian [6] had shown that the Lorentz force on charged particles at the neutron star surface exceeds the gravitational force enormously. As a consequence, plasma from the neutron star surface is extracted.

For simplification, the model makes the following assumptions:

1. The neutron star, if non-rotating, would have a dipolar magnetic field, which is continuous at the stellar surface. In spherical coordinates (r, θ, ϕ) , the magnetic

field is

$$\vec{B}_{al} = \frac{B_0}{2} \left(\frac{R}{r} \right)^3 (2 \cos \theta \vec{e}_r + \sin \theta \vec{e}_\theta), \quad (3.5)$$

where B_0 is the polar magnetic field and R is the radius of the sphere. The "al" stands for the aligned rotator [6, 10].

2. The neutron star is an aligned rotator. There is no obliquity between the rotation axis

$$\vec{\Omega} = \Omega \vec{e}_z = \Omega (\cos \theta \vec{e}_r - \sin \theta \vec{e}_\theta) \quad (3.6)$$

and the dipole axis. Ω is the angular velocity and $P = \frac{2\pi}{\Omega}$ is the period [6, 10].

3. The neutron star can be viewed as a highly magnetized, rotating superconducting sphere. The presence of the magnetic field \vec{B} induces an electric field $\frac{1}{c}(\vec{\Omega} \times \vec{r}) \times \vec{B}$ inside the sphere. This will balance by a distribution of charge giving an electric field \vec{E} , so that at any point \vec{r} inside the sphere a force-free state

$$\vec{E} + \frac{1}{c} (\vec{\Omega} \times \vec{r}) \times \vec{B} = 0, \quad (3.7)$$

where c is the speed of light, is obtained [12].

Inside the neutron star ($r < R$), the particles are moving with a velocity

$$\begin{aligned} \vec{v} &= \frac{1}{c} \begin{pmatrix} 0 \\ 0 \\ \Omega \end{pmatrix} \times \begin{pmatrix} r \sin \theta \cos \phi \\ r \sin \theta \sin \phi \\ r \cos \theta \end{pmatrix} \\ &= \frac{\Omega}{c} r \sin \theta (-\sin \phi \vec{e}_x + \cos \phi \vec{e}_y) \\ &= \frac{\Omega}{c} r \sin \theta \vec{e}_\phi. \end{aligned} \quad (3.8)$$

Taking the assumptions above into account, the electric field is

$$\begin{aligned} \vec{E}_{al}^{int} &= -\frac{1}{c} (\vec{\Omega} \times \vec{r}) \times \vec{B}_{al} \\ &= -\frac{\Omega B_0}{2c} \frac{R^3}{r^2} \begin{pmatrix} 0 \\ 0 \\ \sin \theta \end{pmatrix} \times \begin{pmatrix} 2 \cos \theta \\ \sin \theta \\ 0 \end{pmatrix} \\ &= \frac{\Omega B_0}{2c} \frac{R^3}{r^2} (\sin^2 \theta \vec{e}_r - 2 \sin \theta \cos \theta \vec{e}_\theta) \end{aligned} \quad (3.9)$$

inside the neutron star [10].

The scalar product of the electric field inside the neutron star (Equation 3.9) and the magnetic field (Equation 3.5) gives

$$\vec{E}_{al}^{int} \cdot \vec{B}_{al} = \frac{\Omega B_0^2}{4c} \frac{R^6}{r^5} \begin{pmatrix} \sin^2 \theta \\ -2 \sin \theta \cos \theta \\ 0 \end{pmatrix} \cdot \begin{pmatrix} 2 \cos \theta \\ \sin \theta \\ 0 \end{pmatrix} = 0. \quad (3.10)$$

Thus, the Lorentz invariant $\vec{E}_{al}^{int} \cdot \vec{B}_{al}$ vanishes in the stellar interior [6].

Since \vec{B}_{al} is time independent, the curl of \vec{E}_{al}^{int} has to be

$$\nabla \times \vec{E}_{al}^{int} = -\frac{\partial}{\partial t} \vec{B}_{al} = 0. \quad (3.11)$$

This implies that \vec{E}_{al}^{int} is a conservative vector field. Without derivation the corresponding electrostatic potential is assumed by

$$\Phi_{al}^{int} = \frac{\Omega B_0 R^3}{2c} \frac{r^3}{r} \sin^2 \theta + \Phi_c, \quad (3.12)$$

where Φ_c is a constant independent of (r, θ, ϕ) . To verify the assumption above, $\vec{E}_{al}^{int} = -\nabla \Phi_{al}^{int}$ must be satisfied. The negative gradient of the electrostatic potential (Equation 3.12) gives

$$\begin{aligned} -\nabla \Phi_{al}^{int} &= - \left(\begin{array}{c} \frac{\partial}{\partial r} \\ \frac{1}{r} \frac{\partial}{\partial \theta} \\ \frac{1}{r \sin \theta} \frac{\partial}{\partial \phi} \end{array} \right) \frac{\Omega B_0 R^3}{2c} \frac{r^3}{r} \sin^2 \theta + \Phi_c \\ &= \frac{\Omega B_0 R^3}{2c} \frac{r^2}{r^2} \begin{pmatrix} \sin^2 \theta \\ -2 \sin \theta \cos \theta \\ 0 \end{pmatrix} \\ &= \vec{E}_{al}^{int}. \end{aligned} \quad (3.13)$$

Φ_{al}^{int} is the electrostatic potential in the stellar interior. The external electrostatic potential will be elucidated later on. On the surface the internal and external electrostatic potential must be equal [10].

To show that the neutron star is surrounded by plasma, a proof by contradiction is used. Suppose the neutron star is surrounded by a vacuum. Due to the fact that there are no charged particles outside of the sphere $\nabla \vec{E}_{al}^{ext} = \frac{\rho}{\epsilon_0} = 0$, the external electrostatic potential Φ_{al}^{ext} satisfies the Laplace Equation

$$\Delta \Phi_{al}^{ext} = 0. \quad (3.14)$$

The general solution of Equation 3.14 in an azimuthal symmetry case with boundary condition $\Phi_{al}^{ext} = 0$ for $r \rightarrow \infty$ is the expansion in the Legendre polynomials:

$$\Phi_{al}^{ext} = \sum_{n=0}^{\infty} \frac{a_n}{r^{n+1}} P_n(\cos \theta). \quad (3.15)$$

The Goldreich-Julian model neglects the existence of a central charge of the neutron star. Therefore, the monopole term ($n = 0$) vanishes. Since the two electrostatic potentials have to be equal on the surface and $\Phi_{al}^{int} \sim \sin^2 \theta$, the quadrupole term ($n = 2$) is the only nonzero term. Thus,

$$\Phi_{al}^{ext} = \frac{a_2}{r^3} P_2(\cos \theta), \quad (3.16)$$

where $P_2(\cos \theta)$ is the second Legendre polynomial and a_2 is a coefficient [10].

By using the boundary condition on the surface

$$\Phi_{al}^{int}(r = R, \theta) = \Phi_{al}^{ext}(r = R, \theta), \quad (3.17)$$

Φ_c and a_2 can be determined. In the following calculation, the relation $P_2(\cos \theta) = \frac{3}{2} \cos^2 \theta - \frac{1}{2} \iff \sin^2 \theta = \frac{2}{3} - \frac{2}{3} P_2(\cos \theta)$ is used. On the surface, the electrostatic potentials are

$$\Phi_{al}^{ext}(r = R, \theta) = \frac{a_2}{R^3} P_2(\cos \theta), \quad (3.18)$$

$$\begin{aligned} \Phi_{al}^{int}(r = R, \theta) &= \frac{\Omega B_0 R^2}{2c} \sin^2 \theta + \Phi_c \\ &= \frac{\Omega B_0 R^2}{3c} - \frac{\Omega B_0 R^2}{3c} P_2(\cos \theta) + \Phi_c. \end{aligned} \quad (3.19)$$

The comparison of the coefficients leads to

$$a_2 = -\frac{\Omega B_0 R^5}{3c}, \quad (3.20)$$

$$\Phi_c = -\frac{\Omega B_0 R^2}{3c}. \quad (3.21)$$

The resulting electrostatic potentials are

$$\Phi_{al}^{ext}(r, \theta) = -\frac{\Omega B_0}{3c} \frac{R^5}{r^3} P_2(\cos \theta), \quad (3.22)$$

$$\Phi_{al}^{int}(r, \theta) = \frac{\Omega B_0 R^2}{2c} \left(\frac{R}{r} \sin^2 \theta - \frac{2}{3} \right). \quad (3.23)$$

Note that Φ_{al}^{ext} and Φ_{al}^{int} are continuous at the stellar surface [10].

By taking the negative gradient of the electrostatic potential (Equation 3.22), the electric field on the outside of the sphere yields to

$$\begin{aligned} \vec{E}_{al}^{ext} &= -\nabla \Phi_{al}^{ext} \\ &= \begin{pmatrix} \frac{\partial}{\partial r} \\ \frac{1}{r} \frac{\partial}{\partial \theta} \\ \frac{1}{r \sin \theta} \frac{\partial}{\partial \phi} \end{pmatrix} \frac{\Omega B_0}{6c} \frac{R^5}{r^3} (3 \cos^2 \theta - 1) \\ &= \frac{\Omega B_0}{2c} \frac{R^5}{r^4} \begin{pmatrix} 1 - 3 \cos^2 \theta \\ -2 \sin \theta \cos \theta \\ 0 \end{pmatrix}. \end{aligned} \quad (3.24)$$

The scalar product of the electric field outside of the neutron star (Equation 3.24) and

the magnetic field (Equation 3.5) gives

$$\begin{aligned}
\vec{E}_{al}^{ext} \cdot \vec{B}_{al} &= -\frac{\Omega B_0^2 R}{c} \left(\frac{R}{r}\right)^7 \begin{pmatrix} \frac{3}{2} \cos^2 \theta - \frac{1}{2} \\ \sin \theta \cos \theta \\ 0 \end{pmatrix} \cdot \begin{pmatrix} \cos \theta \\ \frac{1}{2} \sin \theta \\ 0 \end{pmatrix} \\
&= -\frac{\Omega B_0^2 R}{c} \left(\frac{R}{r}\right)^7 \left[\frac{3}{2} \cos^3 \theta - \frac{1}{2} \cos \theta + \frac{1}{2} \frac{\sin^2 \theta}{1 - \cos^2 \theta} \cos \theta \right] \\
&= -\frac{\Omega B_0^2 R}{c} \left(\frac{R}{r}\right)^7 \cos^3 \theta.
\end{aligned} \tag{3.25}$$

The fact that $\vec{E}_{al}^{ext} \cdot \vec{B}_{al} \neq 0$ would not, in itself, be a contradiction to the assumption that there are no charged particles outside the neutron star [6]. The electric field parallel to the magnetic field on the stellar surface

$$E_{||} \equiv \frac{\vec{E}_{al}^{ext} \cdot \vec{B}_{al}}{|\vec{B}_{al}|} \Big|_{r=R} = \frac{-2\Omega B_0 R}{c} \frac{\cos^3 \theta}{\sqrt{3 \cos^2 \theta + 1}} \tag{3.26}$$

is of particular importance because it causes a Lorentz force ($F_L = qE_{||}$) on the charged particles on the neutron star surface, which exceeds gravity by more than 10 orders of magnitude for typical pulsar parameters [12]. As a consequence, plasma from the surface is extracted, which leads to the pulsar magnetosphere, a plasma-filled surrounding of the neutron star. This is a contradiction to the assumption that a pulsar is surrounded by a vacuum [6, 12].

The radial component of the electric field has a discontinuity on the neutron star surface, which implies that the surface charge density

$$\begin{aligned}
\sigma_{al} &= \frac{1}{4\pi} \left(E_{al,r}^{ext} \Big|_{r=R} - E_{al,r}^{int} \Big|_{r=R} \right) \\
&= -\frac{\Omega B_0 R}{8\pi c} \left(3 \cos^2 \theta - 1 + \frac{\sin^2 \theta}{1 - \cos^2 \theta} \right) \\
&= -\frac{\Omega B_0 R}{4\pi c} \cos^2 \theta.
\end{aligned} \tag{3.27}$$

The outer electric field \vec{E} will separate the charges in the pulsar magnetosphere until it is shielded and the force-free state of Equation 3.7 is also maintained outside the neutron star. Similar to Equation 3.9, the electric field turns out to be $\vec{E} = -\frac{1}{c} (\vec{\Omega} \times \vec{r}) \times \vec{B}_{al} = \frac{\Omega B_0}{2c} \frac{R^3}{r^2} (\sin^2 \theta \vec{e}_r - 2 \sin \theta \cos \theta \vec{e}_\theta)$. Taking the gradient of the compensated electric field

\vec{E} gives the resulting charge distribution

$$\begin{aligned}
\rho_{GJ} &= \frac{1}{4\pi} \nabla \cdot \vec{E} \\
&= \frac{1}{4\pi} \left[\frac{1}{r^2} \frac{\partial}{\partial r} (r^2 E_r) + \frac{1}{r \sin \theta} \frac{\partial}{\partial \theta} (\sin \theta E_\theta) + \frac{1}{r \sin \theta} \frac{\partial}{\partial \phi} E_\phi \right]_{=0} \\
&= \frac{1}{4\pi r \sin \theta} \left[\frac{\Omega B_0}{2c} \frac{R^3}{r^2} (-4 \sin \theta \cos^2 \theta + \sin^3 \theta) \right] \\
&= -\frac{\Omega B_0}{4\pi c} \frac{R^3}{r^3} (2 \cos^2 \theta - \sin^2 \theta) \\
&= -\frac{\vec{\Omega} \cdot \vec{B}_{al}}{2\pi c}.
\end{aligned} \tag{3.28}$$

ρ_{GJ} is called the *Goldreich-Julian charge density* and the *null line* $\vec{\Omega} \cdot \vec{B}_{al} = 0$ separates the charge areas of different signs [10, 12].

3.2.2. Orthogonal rotator

Suppose the dipole axis and spin axis $\vec{\Omega}$ are orthogonal. F. C. Michel has shown in [15] that tilting the magnetic field through 90° gives

$$\vec{B}_{or} = \frac{B_0}{2} \left(\frac{R}{r} \right)^3 \begin{pmatrix} 2 \sin \theta \cos \phi_s \\ -\cos \theta \cos \phi_s \\ \sin \phi_s \end{pmatrix}, \tag{3.29}$$

where $\phi_s = \phi - \Omega t$ is the instantaneous phase at time t [16].

A general solution of *Maxwell's equations* for the electric field is

$$\vec{E} = -\nabla \Phi - \frac{1}{c} \frac{\partial \vec{A}}{\partial t}, \tag{3.30}$$

where Φ is a scalar potential and \vec{A} is a vector potential for the magnetic field $\vec{B} = \nabla \times \vec{A}$ [9]. The time dependence of Equation 3.29 induces the right term of Equation 3.30 as follows

$$\vec{E}_I = -\frac{1}{c} \frac{\partial \vec{A}}{\partial t} = -\frac{\Omega B_0}{2c} \frac{R^3}{r^2} \begin{pmatrix} 0 \\ \cos \phi_s \\ -\cos \theta \sin \phi_s \end{pmatrix}. \tag{3.31}$$

Note that the induced field \vec{E}_I is not the full solution of *Maxwell's equations* [9, 16].

Extending beyond the electrostatic fields \vec{E}_S^{int} and \vec{E}_S^{ext} have to be determined with the aid of the left term of Equation 3.30. In [16] the required quadrupole potential inside the neutron star is given by

$$\Phi_{or}^{int} = -\frac{\Omega B_0}{2c} \frac{R^3}{r} \sin \theta \cos \theta \cos \phi_s, \tag{3.32}$$

while the potential outside the neutron star is given by

$$\Phi_{or}^{ext} = -\frac{\Omega B_0}{2c} \frac{R^5}{r^3} \sin \theta \cos \theta \cos \phi_s. \quad (3.33)$$

Since Φ_{or}^{int} and Φ_{or}^{ext} only differ in the power of $(\frac{R}{r})$, the two potentials are continuous at the stellar surface [9, 16].

By taking the negative gradient of the quadrupole potentials, the electrostatic fields yield to

$$\vec{E}_S^{int} = -\nabla \Phi_{or}^{int} = -\frac{\Omega B_0}{2c} \frac{R^3}{r^2} \begin{pmatrix} \sin \theta \cos \theta \cos \phi_s \\ (\sin^2 \theta - \cos^2 \theta) \cos \phi_s \\ \cos \theta \sin \phi_s \end{pmatrix}, \quad (3.34)$$

$$\vec{E}_S^{ext} = -\nabla \Phi_{or}^{ext} = -\frac{\Omega B_0}{2c} \frac{R^5}{r^4} \begin{pmatrix} \sin \theta \cos \theta \cos \phi_s \\ (\sin^2 \theta - \cos^2 \theta) \cos \phi_s \\ \cos \theta \sin \phi_s \end{pmatrix}. \quad (3.35)$$

The electrostatic fields \vec{E}_S^{int} and \vec{E}_S^{ext} are continuous at the stellar surface as well [9, 16].

The total electric field inside and outside the neutron star is the sum of the induction field (Equation 3.31) and the electrostatic field inside (Equation 3.34) and outside (Equation 3.35), respectively. Hence,

$$\vec{E}_{or}^{int} = \left(\vec{E}_S^{int} + \vec{E}_I \right) = -\frac{\Omega B_0}{2c} \frac{R^3}{r^2} \begin{pmatrix} \sin \theta \cos \theta \cos \phi_s \\ 2 \sin^2 \theta \cos \phi_s \\ 0 \end{pmatrix}, \quad (3.36)$$

$$\vec{E}_{or}^{ext} = \left(\vec{E}_S^{ext} + \vec{E}_I \right) = -\frac{\Omega B_0 R}{2c} \begin{pmatrix} \frac{3R^4}{r^4} \sin \theta \cos \theta \cos \phi_s \\ \left(\frac{R^2}{r^2} + \frac{R^4}{r^4} (\sin^2 \theta - \cos^2 \theta) \right) \cos \phi_s \\ - \left(\frac{R^2}{r^2} - \frac{R^4}{r^4} \right) \cos \theta \sin \phi_s \end{pmatrix}. \quad (3.37)$$

The understanding of Equations 3.29, 3.36 and 3.37 has a huge impact in solving the oblique rotator in Section 3.2.3 [9, 16].

3.2.3. Oblique rotator

L. Mestel extended the Goldreich-Julian model to apply to an oblique rotator in [14]. The second assumption in Section 3.2.1 is modified by admitting an obliquity α between the rotation axis and the magnetic axis. The rotation axis $\vec{\Omega}$ (Equation 3.6) remains the same, while the magnetic axis is offset by an angle α with respect to $\vec{\Omega}$. The dipole magnetic field is simply a linear superposition of the aligned and orthogonal limits and results in

$$\begin{aligned} \vec{B}_{ob} &= \cos \alpha \cdot \vec{B}_{al} + \sin \alpha \cdot \vec{B}_{or} \\ &= \frac{B_0}{2} \left(\frac{R}{r} \right)^3 \begin{pmatrix} 2(\cos \theta \cos \alpha + \sin \theta \sin \alpha \cos \phi_s) \\ \sin \theta \cos \alpha - \cos \theta \sin \alpha \cos \phi_s \\ \sin \alpha \sin \phi_s \end{pmatrix}. \end{aligned} \quad (3.38)$$

Note that the inclination angle α is fixed as ϕ_s changes [9, 16].

The electric field inside the neutron star in the oblique rotator model is a linear superposition of \vec{E}_{al}^{int} (Equation 3.9) and \vec{E}_{or}^{int} (Equation 3.36). Hence, the electric field results in

$$\begin{aligned}\vec{E}_{ob}^{int} &= \cos \alpha \cdot \vec{E}_{al}^{int} + \sin \alpha \cdot \vec{E}_{or}^{int} \\ &= \frac{\Omega B_0}{2c} \frac{R^3}{r^2} \begin{pmatrix} \sin^2 \theta \cos \alpha - \sin \theta \cos \theta \sin \alpha \cos \phi_s \\ -2(\sin \theta \cos \theta \cos \alpha + \sin^2 \theta \sin \alpha \cos \phi_s) \\ 0 \end{pmatrix}. \end{aligned} \quad (3.39)$$

It is shown in Calculation B.2 (Appendix B) that in the oblique rotator model, the scalar product of the electric field inside the neutron star and the magnetic field gives

$$\vec{E}_{ob}^{int} \cdot \vec{B}_{ob} = 0. \quad (3.40)$$

Thus, $\vec{E}_{ob}^{int} \cdot \vec{B}_{ob}$ vanishes in the stellar interior [9, 16].

Repeating the linear superposition procedure of Equation 3.39 for \vec{E}_{al}^{ext} (Equation 3.24) and \vec{E}_{or}^{ext} (Equation 3.37) yields to the external electric field

$$\begin{aligned}\vec{E}_{ob}^{ext} &= \cos \alpha \cdot \vec{E}_{al}^{ext} + \sin \alpha \cdot \vec{E}_{or}^{ext} \\ &= \frac{\Omega B_0 R}{2c} \begin{pmatrix} \frac{R^4}{r^4}(1 - 3 \cos^2 \theta) \cos \alpha - 3 \frac{R^4}{r^4} \sin \theta \cos \theta \sin \alpha \cos \phi_s \\ -2 \frac{R^4}{r^4} \sin \theta \cos \theta \cos \alpha - \left(\frac{R^2}{r^2} + \frac{R^4}{r^4} (\sin^2 \theta - \cos^2 \theta) \right) \sin \alpha \cos \phi_s \\ \left(\frac{R^2}{r^2} - \frac{R^4}{r^4} \right) \cos \theta \sin \alpha \sin \phi_s \end{pmatrix} \end{aligned} \quad (3.41)$$

in the oblique rotator model [16].

The electric field parallel to the magnetic field on the stellar surface is determined in Calculation B.3 (Appendix B) as follows:

$$\begin{aligned}E_{\parallel} &= \left. \left(\vec{E}_{ob}^{ext} \cdot \vec{B}_{ob} \right) \right|_{r=R} = -\frac{\Omega B_0^2 R}{c} \cdot \cos \theta \left[\cos^2 \theta \cos^2 \alpha + \sin^2 \theta \sin^2 \alpha \cos^2 \phi_s \right. \\ &\quad \left. + 2 \sin \theta \cos \theta \sin \alpha \cos \alpha \cos \phi_s \right]. \end{aligned} \quad (3.42)$$

Similar to the Goldreich-Julian model, the Lorentz force ($F_L = qE_{\parallel}$) extracts charged particles from the surface. This leads to a pulsar magnetosphere, a plasma-filled surrounding of the neutron star [14].

As seen in the Goldreich-Julian model, the radial component of the electric field has a discontinuity on the neutron star surface, which results in a surface charge density (Equation 3.27). In the oblique rotator model, the discontinuity of the radial component

yields to the surface charge density

$$\begin{aligned}
\sigma_{ob} &= \frac{1}{4\pi} \left(E_{ob,r}^{ext} \Big|_{r=R} - E_{ob,r}^{int} \Big|_{r=R} \right) \\
&= -\frac{\Omega B_0 R}{8\pi c} \left[(3 \cos^2 \theta - 1) \cos \alpha + 3 \sin \theta \cos \theta \sin \alpha \cos \phi_s \right. \\
&\quad \left. + \frac{\sin^2 \theta}{1 - \cos^2 \theta} \cos \alpha - \sin \theta \cos \theta \sin \alpha \cos \phi_s \right] \\
&= -\frac{\Omega B_0 R}{4\pi c} [\cos^2 \theta \cos \alpha + \sin \theta \cos \theta \sin \alpha \cos \phi_s].
\end{aligned} \tag{3.43}$$

Note that $\sigma_{ob}(\alpha = 0) = \sigma_{al}$ [14].

Similar to the Goldreich-Julian model, the outer electric field \vec{E} will separate the charges in the pulsar magnetosphere until it is shielded and the force-free state of Equation 3.7 is also maintained outside the neutron star. The electric field is

$$\begin{aligned}
\vec{E} &= -\frac{1}{c} (\vec{\Omega} \times \vec{r}) \times \vec{B}_{ob} \\
&= \frac{\Omega B_0}{2c} \frac{R^3}{r^2} \begin{pmatrix} \sin^2 \theta \cos \alpha - \sin \theta \cos \theta \sin \alpha \cos \phi \\ -2(\sin \theta \cos \theta \cos \alpha + \sin^2 \theta \sin \alpha \cos \phi) \\ 0 \end{pmatrix}.
\end{aligned} \tag{3.44}$$

Taking the gradient of the compensated electric field \vec{E} gives the resulting charge distribution

$$\begin{aligned}
\rho_{ob} &= \frac{1}{4\pi} \nabla \cdot \vec{E} \\
&= \frac{1}{4\pi r \sin \theta} \left[\frac{\Omega B_0}{2c} \frac{R^3}{r^2} (-4 \sin \theta \cos^2 \theta \cos \alpha + 2 \sin^3 \theta \cos \alpha - 6 \sin^2 \theta \cos \theta \cos \phi_s) \right] \\
&= -\frac{\Omega B_0}{4\pi c} \frac{R^3}{r^3} (3 \cos^2 \theta \cos \alpha - \cos \alpha + 3 \sin \theta \cos \theta \sin \alpha \cos \phi_s) \\
&= -\frac{\vec{\Omega} \cdot \vec{B}_{ob}}{2\pi c}.
\end{aligned} \tag{3.45}$$

Note that ρ_{ob} has a similar form as ρ_{GJ} (Equation 3.28) and the resulting *null line* $\vec{\Omega} \cdot \vec{B}_{ob} = 0$, which separates the charge areas of different signs, are time dependent [14].

3.3. Rotating vector model

One of the most important conclusion of the studies of PSR B0833-45 by Radhakrishnan and Cooke is the *rotating vector model* (RVM), which implies a quantitative prediction of the polarization position angle ψ , as a function of rotational phase ϕ .

The geometrical factors are presented in Figure 3.4. \hat{m} represents the unit vector along the magnetic axis, which is inclined to the rotation axis at angle α . As the star rotates with rotational phase ϕ ,

$$\hat{m} = (\hat{x} \cos \phi + \hat{y} \sin \phi) \sin \alpha + \hat{z} \cos \alpha \tag{3.46}$$

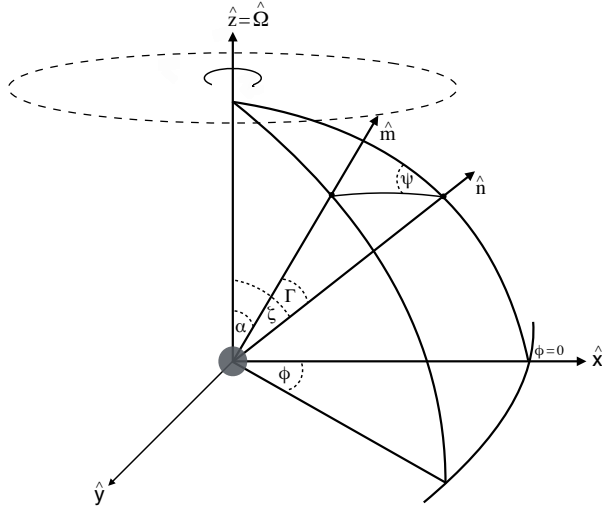


Figure 3.4.: The gray ball, centered in the origin of the coordinate system, represents the pulsar itself. $\hat{\Omega}$ is the unit vector in direction of the rotation axis $\vec{\Omega}$, which is equal to the z -axis of the coordinate system. All angles described in Section 3.3 are delineated for one particular moment, where $\phi \neq 0$. The pulsar and its magnetic axis \hat{m} rotate counter clockwise.

describes the conical motion of the magnetic axis. The unit vector along the line of sight to the observer is represented by \hat{n} . It lies permanently in the xz -plane with an inclination ζ to the rotation axis, thus

$$\hat{n} = \hat{z} \cos \zeta + \hat{x} \sin \zeta. \quad (3.47)$$

ζ can be expressed as $\zeta = \alpha + \beta$, where β is the *impact parameter* of Figure 3.3, which represents the closest approach of the magnetic axis to the line of sight. This is the case when \hat{m} also lies in the xz -plane ($\phi = 0$) [5, 12].

The angle Γ formed by \hat{n} with respect to \hat{m} at any ϕ is given by

$$\begin{aligned} \cos \Gamma &= \frac{\hat{m} \cdot \hat{n}}{|\hat{m}| \cdot |\hat{n}|} \\ &= \cos \zeta \cos \alpha + \sin \zeta \sin \alpha \cos \phi. \end{aligned} \quad (3.48)$$

Note that Equation 3.48 leads to $\Gamma = \beta$ at the rotational phase $\phi = 0$ (see Figure 3.5). The generally accepted model of the stable pulsar radio beam is a cone-shaped beam centered on the magnetic axis, which is provided by the open field line regions [12]. The cones of PSR B0833-45 are delineated in Figure 3.3. If the emission cone is confined by the last open magnetic field lines, the emission cone half-opening angle ρ can be calculated. The edge of the cone intersects the line of sight to the observer, when ϕ is half of the width W of the observed pulse (see Figure 3.5). As a result, the angle Γ

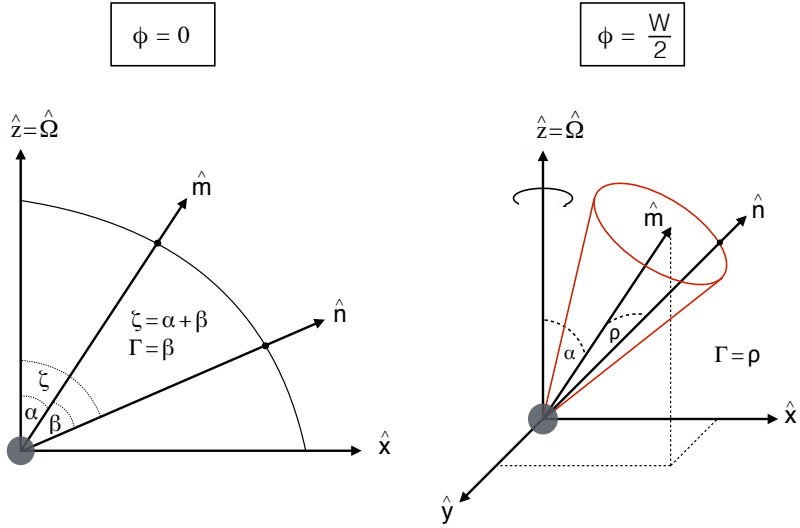


Figure 3.5.: The left figure depicts the unique inclination $\zeta = \alpha + \beta$ of the unit vector \hat{n} to the rotational axis at rotational phase $\phi = 0$. The geometry of the emission cone (red) is delineated in the right figure. The angles in these two figures are explained in detail in Section 3.3.

between \hat{m} and \hat{n} becomes the emission cone half-opening angle ρ . Using Equation 3.48, leads to

$$\cos \rho = \cos \zeta \cos \alpha + \sin \zeta \sin \alpha \cos \left(\frac{W}{2} \right), \quad (3.49)$$

where $\Gamma = \rho$ and $\phi = \frac{W}{2}$ [5, 12].

Up to this point all necessary angles, except the most important polarization position angle, had been elucidated. The idea of the determination of polarization position angle is first worked out by M. M. Komesaroff [11]. The E -vector of the radiation, which is equal to the polarization, received at any particular moment will be approximately in the plane of the sky from the viewpoint of the observer. The standard basis vectors \hat{n}_1 and \hat{n}_2 of this plane are constructed as follows

$$\hat{n}_1 = \frac{\hat{z} \times \hat{n}}{|\hat{z} \times \hat{n}|} = \hat{y}, \quad (3.50)$$

$$\hat{n}_2 = \frac{\hat{n} \times \hat{y}}{|\hat{n} \times \hat{y}|} = -\hat{x} \cos \zeta + \hat{z} \sin \zeta. \quad (3.51)$$

The projection of the magnetic axis into the plane of the sky is

$$\hat{m}_p = \underbrace{(\hat{m} \cdot \hat{n}_1)}_{= \sin \psi} \hat{n}_1 + \underbrace{(\hat{m} \cdot \hat{n}_2)}_{= \cos \psi} \hat{n}_2. \quad (3.52)$$

and delineated in Figure 3.6. The inclination ψ of the projection of the magnetic axis \hat{m}_p to the axis \hat{n}_2 is essentially the position angle of the magnetic field vector. Assuming

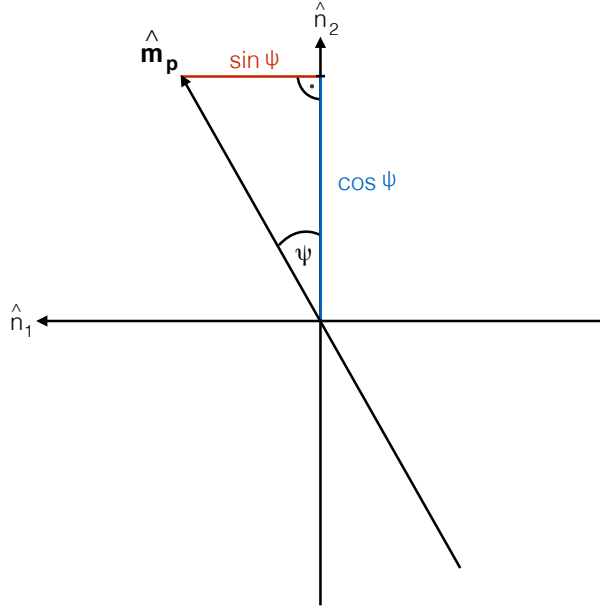


Figure 3.6.: The plane of the sky from the perspective of the observer is delineated. The unit vector of the projection of the magnetic axis \hat{m}_p is inclined at position angle ψ to the axis \hat{n}_2 . Like the usual astronomical convention, ψ increases counter clockwise on the sky. The component of Equation 3.52 is marked in this plane.

ψ to be the position angle of the \vec{E} -vector of the radiation, one can compute the RVM as follows

$$\begin{aligned}\tan \psi &= \frac{(\hat{m} \cdot \hat{n}_1)}{(\hat{m} \cdot \hat{n}_2)} \\ &= \frac{\sin \alpha \sin \phi}{\sin \zeta \cos \alpha - \cos \zeta \sin \alpha \cos \phi}.\end{aligned}\quad (3.53)$$

This assumption is only durable, if the radiation is assumed to be beamed outward radially along the magnetic field lines. Adding two offset parameters (ϕ_0 and ψ_0) to Equation 3.53, the polarization position angle ψ_{RVM} becomes

$$\tan(\psi_{\text{RVM}} - \psi_0) = \frac{\sin \alpha \sin(\phi - \phi_0)}{\sin \zeta \cos \alpha - \cos \zeta \sin \alpha \cos(\phi - \phi_0)}, \quad (3.54)$$

where α is the angle from the rotation axis to the magnetic axis, $\zeta \equiv \alpha + \beta$ is the angle from the rotation axis to the line of sight and ϕ is the rotational phase of the pulsar. ψ_0 is the polarization position angle at pulsar rotation phase ϕ_0 [11, 12, 15].

In principle, the ψ swing enables a determination of the angles α and β , but in practice the range of the pulse longitudes ϕ with well-defined position angles is usually limited by

the small pulse duty cycle. However, the steepest gradient of Equation 3.54 is determined by

$$\left(\frac{d\psi}{d\phi} \right)_{max} = \frac{\sin \alpha}{\sin \beta}, \quad (3.55)$$

which is measured at the fiducial point $\phi = \phi_0$ [12].

3.4. Curvature radiation

In general, the pulsar radio emission is believed to be generated by relativistic particle bunches streaming out along the open magnetic field lines in pulsar magnetosphere. One of the most possible emission mechanisms for pulsar radio emission is curvature radiation, which is elaborated in this section.

In Section 3.2, it is shown that charged particles (electrons or positrons) are extracted from the neutron star surface and accelerated at the polar cap by the electric field parallel to the magnetic field Equation 3.26 (Equation 3.42 for the oblique rotator) up to relativistic energies [1]. This results in a relativistic flow of plasma moving along the curved magnetic field lines and emitting electromagnetic radiation [6].

The geometry of the coherent curvature radiation mechanism is delineated in Figure 3.7. The unit vector \hat{m} indicates the magnetic axis and is described by Equation 3.46. The line of sight \vec{n} is inclined at angle ζ to the rotation axis $\hat{\Omega}$ and its unit vector is given by Equation 3.47. The plasma, which moves along the open field line (red line), is marked as black tube. ζ_c is the angle between $\hat{\Omega}$ and the center of momentum (CM) velocity of the plasma

$$\hat{v}_c = v_{\parallel} \hat{b} + \hat{\Omega} \times \hat{r}, \quad (3.56)$$

where v_{\parallel} is the velocity of the CM parallel to \hat{b} , the unit vector tangent to the dipolar magnetic field lines and \hat{r} is the unit vector towards the emission point [1, 3].

The line of sight \vec{n} and CM velocity \hat{v}_c are depicted to be aligned ($\zeta \simeq \zeta_c$) in Figure 3.7. This is the approximate condition for the observer to receive radiation, since the particle radiation beam is in direction of \hat{v}_c . With the help of the condition $\zeta \simeq \zeta_c$, Equation 3.56 can be expressed as

$$\hat{v}_c = (\hat{x} \cos \phi' + \hat{y} \sin \phi') \sin \zeta + \hat{z} \cos \zeta, \quad (3.57)$$

since $|\hat{v}_c - \hat{m}|$, $|\hat{v}_c - \hat{r}|$ and $|\hat{m} - \hat{r}|$ lie inside the open field line region and all of them are of the order of $w = (\frac{\Omega r}{c})^{1/2}$, which is the angular width of the open field line region [1, 3].

M. Blaskiewicz, J. M. Cordes and I. Wassermann [3] derived the acceleration of the plasma

$$\hat{a} = -\frac{1}{2r} [\hat{m} c^2 - \hat{v}_c (\hat{v}_c \cdot \hat{m}) c^2 - 3cr\Omega(\hat{z} \times \hat{v}_c)] + \mathcal{O}(w^3) \quad (3.58)$$

by differentiating Equation 3.56 with respect to time. Finding the acceleration of the plasma at the emission point is essential for calculating the polarization position angle, which is the angle between the electric field of radiation and the projected spin axis \hat{n}_2

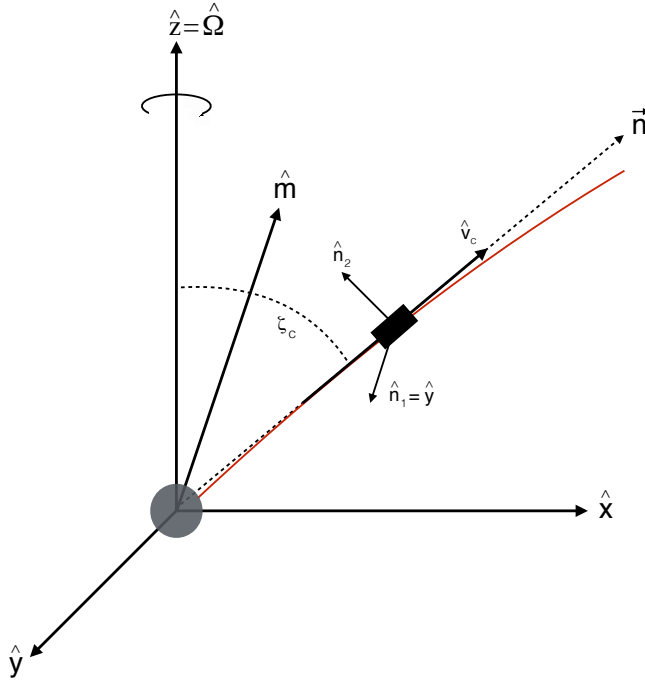


Figure 3.7.: This figure shows the geometry of the coherent curvature radiation mechanism. The black tube, representing the plasma, moves along the open magnetic field line (red). At the emission point, which is the current position of the tube in this simplified sketch, the particles emit radiation in the direction of the CM plasma velocity \hat{v}_c towards the observer. The standard basis vectors \hat{n}_1 and \hat{n}_2 of the plane of sky are delineated at the CM.

on the plane of sky (see Section 3.3), because the plasma acceleration at the emission point is parallel to electric field vector \vec{E} of the radiation. Since the observer receives radiation, the CM velocity at the emission point is $\hat{v}_c = \hat{n}$. Substituting this in Equation 3.58, the acceleration of plasma becomes

$$\begin{aligned}\hat{a}' &= -\frac{1}{2r} [\hat{m}c^2 - \hat{n}(\hat{n} \cdot \hat{m})c^2 - 3cr\Omega(\hat{z} \times \hat{n})] + \mathcal{O}(w^3) \\ &= -\frac{c^2}{2r} \begin{pmatrix} \sin \alpha \cos \phi - \sin \alpha \sin^2 \zeta \cos \phi - \cos \alpha \sin \zeta \cos \zeta \\ \sin \alpha \sin \phi - \frac{3\Omega r}{c} \sin \zeta \\ \cos \alpha - \sin \alpha \sin \zeta \cos \zeta \cos \phi - \cos \alpha \cos^2 \zeta \end{pmatrix} + \mathcal{O}(w^3),\end{aligned}\quad (3.59)$$

at the emission point [1, 3].

The plane of sky was constructed in Section 3.3. The standard basis vectors \hat{n}_1 and \hat{n}_2 , delineated in Figure 3.7, are given by Equation 3.50 and 3.51. In contrast to Section 3.3, where the polarization of the radiation is assumed to be parallel to the projection of the magnetic axis \hat{m}_p (Equation 3.52), the proceeding of deriving the polarization position angle curve is made with the plasma acceleration at the emission point \hat{a}' (Equation

3.59). With the auxiliary calculations

$$\hat{a}' \cdot \hat{n}_1 = -\frac{c^2}{2r} \sin \alpha \sin \phi + \frac{3\Omega c}{2} \sin \zeta, \quad (3.60)$$

$$\begin{aligned} \hat{a}' \cdot \hat{n}_2 &= -\frac{c^2}{2r} \left(-\sin \alpha \cos \zeta \cos \phi + \sin \alpha \sin^2 \zeta \cos \zeta \cos \phi + \cos \alpha \sin \zeta \cos^2 \zeta \right. \\ &\quad \left. + \cos \alpha \sin \zeta - \sin \alpha \sin^2 \zeta \cos \zeta \cos \phi - \cos \alpha \sin \zeta \cos^2 \zeta \right) \\ &= -\frac{c^2}{2r} (\cos \alpha \sin \zeta - \sin \alpha \cos \zeta \cos \phi), \end{aligned} \quad (3.61)$$

the polarization position angle ψ can be estimated as follows

$$\begin{aligned} \tan \psi &= \frac{(\hat{a}' \cdot \hat{n}_1)}{(\hat{a}' \cdot \hat{n}_2)} \\ &= \frac{\sin \alpha \sin \phi - \frac{3\Omega r}{c} \sin \zeta}{\sin \zeta \cos \alpha - \cos \zeta \sin \alpha \cos \phi}. \end{aligned} \quad (3.62)$$

Note that Equation 3.62 is almost equivalent to the standard RVM (Equation 3.53). The observed ψ -curve is unchanged, but it is shifted by a value of $3\Omega r$ in the rotational phase. The rotation of the pulsar is neglected in the standard RVM (Section 3.3). However, this shift does not have any relevance, because the RVM fit (see Section 4.1.2) uses an offset parameter in rotational phase. Both models results in the same RVM fit [1, 3].

3.5. Interpulse studies

In Figure 3.8, the plasma velocity (Equation 3.56) and the plasma acceleration (Equation 3.58) of two particular emission regions, which are located in different emission cones, are illustrated. At the appropriate rotational phase of the sketch, the plasma velocity \hat{v}_1 is aligned with the observer's line of sight \vec{n} , so that the observer receives radiation, which is polarized along the plasma acceleration \hat{a}_1 . After a rotational phase shift of 180° the plasma velocity \hat{v}_2 is aligned with the observer's line of sight \vec{n} and the observer will receive radiation from the opposite cone, which is polarized along the plasma acceleration \hat{a}_2 . The plasma acceleration \hat{a}_2 points in the exact opposite direction to \hat{a}_1 . However, the resulting \vec{E} -vectors of the radiation of the two particular regions are indistinguishable, because they are parallel to each other. This is depicted in Figure 3.8 and mathematically shown by Equation 3.67.

If the pulse profile of pulsars contains emission of both cones, the profile is divided into the mainpulse (MP) and the interpulse (IP). Each pulse structure is identified with the emission of one cone. The cone with the strongest emission is assigned to the MP. The two pulses are separated in pulse phase by around 180° . The position angle of the MP is indistinguishable from the position angle of the IP. The geometrical values of the

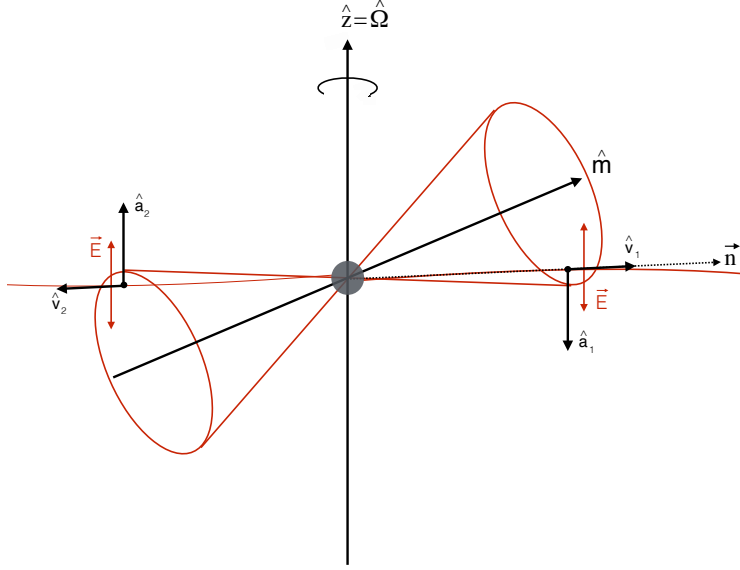


Figure 3.8.: As before, the gray ball represents the pulsar. The open magnetic field lines, which the plasma bunches are moved along, are represented by the red lines inside the red emission cones. Two particular emission regions and the corresponding plasma velocity and acceleration vectors are depicted. The resulting \vec{E} -vectors of the radiation of each emission region are along the plasma accelerations.

IP are determined by

$$\alpha^{IP} = 180^\circ - \alpha^{MP}, \quad (3.63)$$

$$\zeta^{IP} = \zeta^{MP}, \quad (3.64)$$

$$\phi_0^{IP} = \phi_0^{MP} + 180^\circ, \quad (3.65)$$

$$\psi_0^{IP} = \psi_0^{MP}. \quad (3.66)$$

Substitute Equations 3.63, 3.64, 3.65 and 3.66 into the RVM (Equation 3.54) gives

$$\begin{aligned} \psi^{IP} &= \arctan \left(\frac{\sin \alpha^{IP} \sin(\phi - \phi_0^{IP})}{\sin \zeta^{IP} \cos \alpha^{IP} - \cos \zeta^{IP} \sin \alpha^{IP} \cos(\phi - \phi_0^{IP})} \right) + \psi_0^{IP} \\ &= \arctan \left(\frac{-\sin \alpha^{MP} \sin(\phi - \phi_0^{MP})}{-\sin \zeta^{MP} \cos \alpha^{MP} + \cos \zeta^{MP} \sin \alpha^{MP} \cos(\phi - \phi_0^{MP})} \right) + \psi_0^{MP} \quad (3.67) \\ &= \psi^{MP}, \end{aligned}$$

where $\psi^{IP} = \psi_{RVM}(\alpha^{IP}, \zeta^{IP}, \phi_0^{IP}, \psi_0^{IP})$ and $\psi^{MP} = \psi_{RVM}(\alpha^{MP}, \zeta^{MP}, \phi_0^{MP}, \psi_0^{MP})$.

4. Emission beam geometry of PSR J2007+2722

B. Allen and B. Knispel [2] analyzed the pulse polarization data of PSR J2007+2722 explicitly. In Section 4.1, the results of B. Allen and B. Knispel are reproduced using the same pulse polarization data and the same methods. Up to small variations, the following results are consistent with the results of B. Allen and B. Knispel. The programming code for processing the data and the display of the results are shown in the Appendix C.

Since the RVM only describes the pulse polarization data of PSR J2007+2722 to a certain degree, several new attempts are conducted in Section 4.2. One successful attempt is to disregard the data points of the almost completely depolarized part at 2000 MHz for the RVM fitting (see Section 4.2.1). In Section 4.2.3, the *background radiation model* (BRM), which uses the superposition of the pulsar radiation and a fixed linearly polarized radiation, is developed. This model is able to describe the data well.

4.1. Previous studies of PSR J2007+2722

The isolated pulsar PSR J2007+2722 is located in the Vulpecula constellation at *right ascension* $\alpha = 20^{\text{h}}07^{\text{m}}15^{\text{s}}.83$, *declination* $\delta = +27^{\circ}22'47''.91$ (J2000) with an angular frequency $\nu = 40.821$ Hz. The dispersion measure $DM = 127 \text{ pc cm}^{-3}$ implies a distance from the pulsar to the earth of approximately 5.4 kpc (≈ 17600 ly) [2].

PSR J2007+2722 was found on 2010 July 11 in radio survey data from the Arecibo Observatory taken in February 2007 via the *Einstein@Home* project. *Einstein@Home* is an ongoing volunteer distributed computing project, where science enthusiasts of the general public can provide idle computing power of their laptops and desktop computers to search for weak astrophysical signals. PSR J2007+2722 was the first discovery of the *Einstein@Home* project. A detailed description of the *Einstein@Home* search for radio pulsars is given by B. Allen and B. Knispel [2].

4.1.1. Pulse profile

On 2010 July 21, follow-up observations on PSR J2007+2722 were executed with the Green Bank Telescope (GBT). The folded pulse profile at the observation frequencies 820, 1500, 2000, and 8900 MHz are shown in Figure 4.1. The observations at 1500, 2000 and 8900 MHz also provided full Stokes polarization parameters I , Q , U and V (see Figure 4.2). For a detailed derivation and description of the Stokes polarization parameters, see Section 2.2 - 2.4.

The pulse profile of PSR J2007+2722 has remarkable characteristics. At all four observation frequencies, the pulse profile is unusually broad and contains two clearly separated peaks. The peaks are connected by an emission "bridge", which flattens with increasing observation frequency. The location of the emission bridge shifts to the outside of the peaks at the highest frequency. At 820, 1500 and more or less 2000 MHz, the emission bridge is in between the peaks. This indicates that the pulsar is "always on", which means that some radio emission of PSR J2007+2722 is present at all rotational phases.

Another specialty of the pulse profile of PSR J2007+2722 is the evolution of the peak positions at different observing frequencies. The higher the observing frequencies, the wider the gap between the peaks. Assuming that the two peaks originated from the same magnetic pole, then based on the model by M. M. Komesaroff (1970) in [11], the edge of the hollow beam must intersect the line of sight twice. However, the model predicts that emission with greater frequencies will be produced closer to the neutron star surface. As a consequence, the emission cone half-opening angle (Equation 3.49) and the gap between the peaks will decrease, when the observing frequency increases. This is the opposite behavior as observed in Figure 4.1 for PSR J2007+2722.

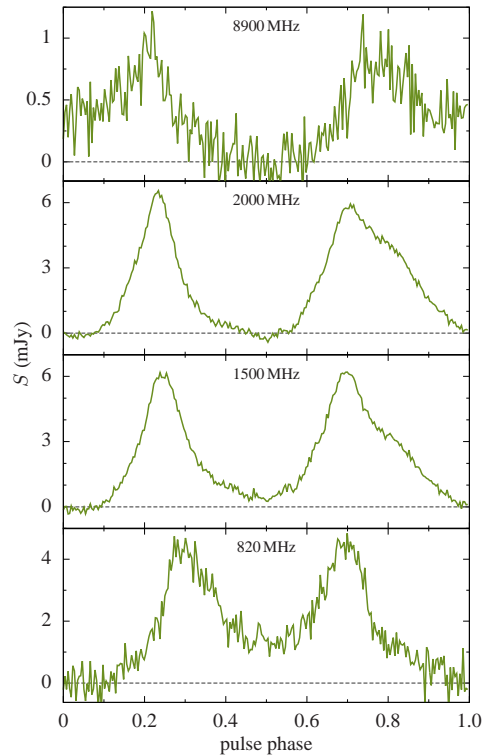


Figure 4.1.: The folded pulse profile of PSR J2007+2722 in mJy at observation frequencies 820, 1500, 2000, and 8900 MHz (bottom-up). This figure originates from [2].

There are even more difficulties in assuming that the two peaks did not originate from the same magnetic pole. Since one peak is then originated from the opposite magnetic pole, the two peaks will be separated in pulse phase by around 180° and the position of the peaks will be independent of the observing frequency, which is not the case in Figure 4.1. It will work out for the pulse profiles at 1500 and 2000 MHz, but not for the pulse profiles at 820 and 8900 MHz. This is the reason why in the following it is assumed that the two peaks originate from the same magnetic pole.

4.1.2. Polarization studies

As mentioned in Section 4.1.1, the GBT follow-up observations provided full Stokes polarization parameters at 1500, 2000 and 8900 MHz. Since the 8900 MHz data was too noisy, only the observations at 1500 and 2000 MHz are used for polarimetry (see Figure 4.2) [2].

By using the Stokes polarization parameters, the polarization position angle

$$\psi = \frac{1}{2} \arctan \left(\frac{U}{Q} \right), \quad (4.1)$$

which is derived in Section 2.5, can be computed as a function of the pulse phase. The top half of Figure 4.2 shows the polarization position angle profiles as a function of the pulse phase, along with estimated measurement uncertainties $\Delta\psi$. The bottom half of each plot of Figure 4.2 shows the radio flux-density profiles [2].

The Rotating Vector Model (RVM) by Radhakrishnan & Cooke with their quantitative prediction of the polarization position angle ψ_{RVM} has been derived in Section 3.3. Solving Equation 3.54 for ψ_{RVM} gives

$$\psi_{\text{RVM}} = \arctan \left(-\frac{\sin \alpha \sin(\phi - \phi_0)}{\sin \zeta \cos \alpha - \cos \zeta \sin \alpha \cos(\phi - \phi_0)} \right) + \psi_0, \quad (4.2)$$

where α is the angle from the rotation axis to the magnetic axis, $\zeta \equiv \alpha + \beta$ is the angle from the rotation axis to the line of sight and ϕ is the rotational phase of the pulsar. ψ_0 is the polarization position angle at pulsar rotation phase ϕ_0 . The conventions of J. E. Everett & J. M. Weisberg [4] are adopted, which cause the minus sign in Equation 4.2 [2, 12].

The four RVM parameters α , ζ , ϕ_0 and ψ_0 define the emission beam geometry of the pulsar. The values of the four RVM parameters are determined by comparing the polarization position angle profiles with the RVM prediction (Equation 4.2) using a least-squares fit. Therefore, the normalized sum of the squared-residuals

$$\chi^2 = \frac{1}{N-4} \sum_{i=1}^N \frac{(\psi(\phi_i) - \psi_{\text{RVM}}(\phi_i))^2}{(\Delta\psi_i)^2} \quad (4.3)$$

between the measured ψ (Equation 4.1) and the theoretical ψ_{RVM} (Equation 4.2) is calculated at each point of the four dimensional parameter space $(\alpha, \zeta, \phi_0, \psi_0)$. Here, N labels the number of measurements of the polarization position angle ψ at different

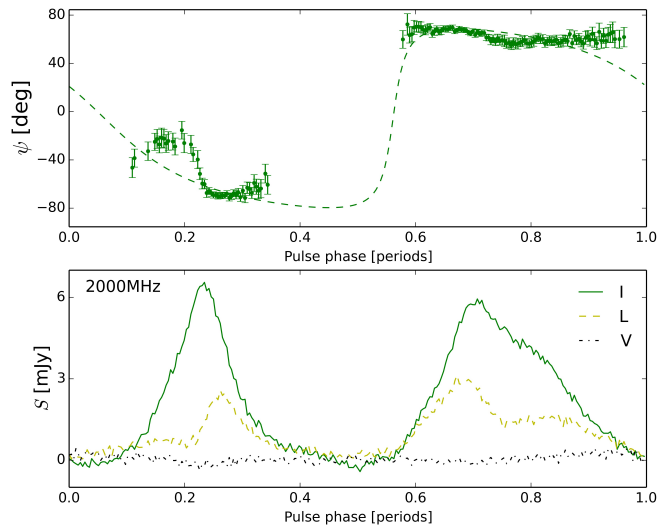
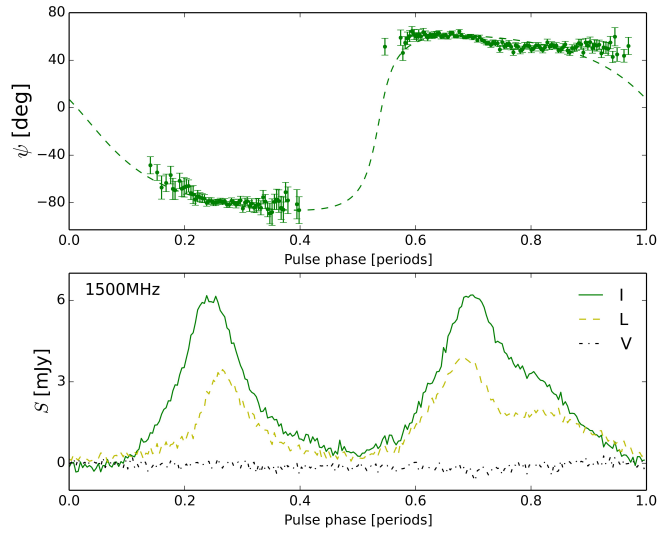


Figure 4.2.: Each Subfigure (1500 MHz (top); 2000 MHz (bottom)) has two separated plots. The bottom half shows the radio flux-density S in intensity I (green solid), linearly polarized component $L = \sqrt{U^2 + Q^2}$ (yellow dashed) and circularly polarized component V (black dash-dotted), while the top half shows the derived polarization position angle ψ of Equation 4.1 as a function of the pulse phase, along with estimated measurement uncertainties $\Delta\psi$. The green dashed line in each top half of the plots depicts the theoretical curve ψ_{RVM} for the best-fit RVM parameters given by Equation 4.2 and Table 4.1. The plots are constructed with the Python code *J2007DisplayData.py*, which is shown in Appendix C.

rotation phase. The 1500 MHz data provides $N = 158$ measurements of ψ , while the 2000 MHz data provides $N = 143$ measurements of ψ . The running index i labels the N distinct pulsar rotation phases ϕ_i for which $\psi_i = \psi(\phi_i)$ was measured. The experimental measurement uncertainty in ψ_i is labeled by $\Delta\psi_i$ in each measurement [2].

χ^2 is a conventionally normalized reduced χ^2 statistic, since the number of degrees of freedom is $N - 4$. The smaller the values for χ^2 , the better the RVM prediction fits the data. The goal is to detect the smallest value for χ^2 in the parameter space $(\alpha, \zeta, \phi_0, \psi_0)$ and conclude the best-fit RVM parameters for determining the emission beam geometry of PSR J2007+2722. The C code *chi_squared.c* will execute the calculation of χ^2 over the whole parameter space or a small area of the parameter space. The output will be a list of χ^2 values as a function of (α, ζ) , which are minimized over ϕ_0 and ψ_0 . The Python code *J2007Heatmap.py* displays χ^2 in form of a heat map. Both codes are shown in Appendix C [2].

ν	α	ζ	β	ϕ_0	ψ_0	ρ	χ^2
1500 MHz	111.6°	104.1°	-7.5°	193°	-12.9°	78.4°	3.137
2000 MHz	115.1°	109.7°	-5.4°	202°	-5.5°	77.5°	3.736

Table 4.1.: The best-fit RVM parameters for PSR J2007+2722 are obtained from the analysis of the 1500 and 2000 MHz data. In the last column, the minimum χ^2 values, which correspond to the best-fit RVM parameters, are listed. The impact parameter β represents the closest approach of the magnetic axis to the line of sight and is calculated with $\beta = \zeta - \alpha$. The emission cone half-opening angle ρ (Equation 4.4) is determined by the best-fit RVM parameters and the peak-to-peak width ($W_{1500} = 165.9^\circ$; $W_{2000} = 107.2^\circ$). As expected, the independent fits at 1500 and 2000 MHz lead to very similar emission beam geometry parameters.

By applying the codes above to the 1500 and 2000 MHz data of PSR J2007+2722, the best-fit parameters, which are listed in Table 4.1, are obtained and the resulting heat maps, which are shown in Figure 4.4 and 4.5, are created. The analysis of each data set is separated in two heat maps, which differ by the grid size and spacing of $(\alpha, \zeta, \phi_0, \psi_0)$. The top heat maps extend over the full range of the $(\alpha, \zeta, \phi_0, \psi_0)$ -space, while the bottom heat maps extend over a small area around the minimum of the top heat maps. The determination of χ^2 over the full range of the parameter space serves as a rough estimation of the minimum. Afterwards, the same procedure is conducted with a finer grid spacing around the minimum in order to increase the accuracy. The best-fit RVM parameters of Table 4.1 are consistent with the best-fit RVM parameters of [2].

Once the best-fit RVM parameters and the observed separation W between the pulse peaks are determined, the radio emission cone half-opening angle

$$\rho = \arccos \left(\cos \alpha \cos \zeta + \sin \alpha \sin \zeta \cos \left(\frac{W}{2} \right) \right), \quad (4.4)$$

which was described in Section 3.3, can be computed. The peak-to-peak width of the pulse profile at 1500 MHz is $W_{1500} = 165.9^\circ$. As mentioned in Section 4.1.1, the pulse

profile shows a dependency on the observing frequency, so that peak-to-peak width increases at 2000 MHz to $W_{2000} = 170.2^\circ$. Using the best-fit α and ζ values from Table 4.1 and the peak-to-peak widths above, the resulting emission cone half-opening angles at 1500 and 2000 MHz yield to $\rho_{1500} = 78.4^\circ$ and $\rho_{2000} = 77.5^\circ$, respectively [2].

The best-fit RVM parameters and the resulting emission cone half-opening angles ρ_{1500} and ρ_{2000} were determined with the assumption that the two peaks of the pulse profiles are originated from the same magnetic pole. The emission geometry of PSR J2007+2722 is depicted in Figure 4.3 using the values at 1500 MHz. Since the values at both observing frequencies are very similar, the emission geometry of PSR J2007+2722 at 2000 MHz would not differ much from Figure 4.3.

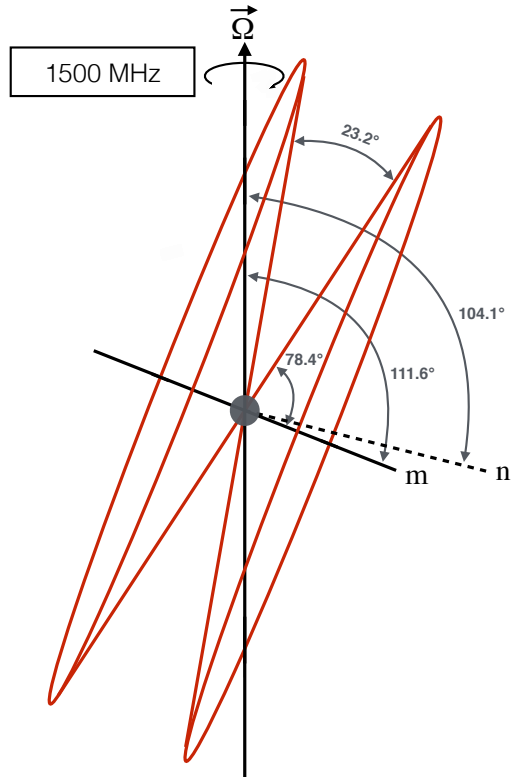


Figure 4.3.: The emission beam geometry of PSR J2007+2722 using the best-fit RVM parameters at 1500 MHz. The gray ball in the center represents the pulsar and $\vec{\Omega}$ declares the rotation axis. The magnetic axis m is inclined at angle $\alpha_{1500} = 111.6^\circ$ to $\vec{\Omega}$, while the line of sight n is inclined at angle $\zeta_{1500} = 104.1^\circ$ to $\vec{\Omega}$. The emission cones are delineated in red with the half-opening angle $\rho_{1500} = 78.4^\circ$. The angle between the two emission cones is 23.2° .

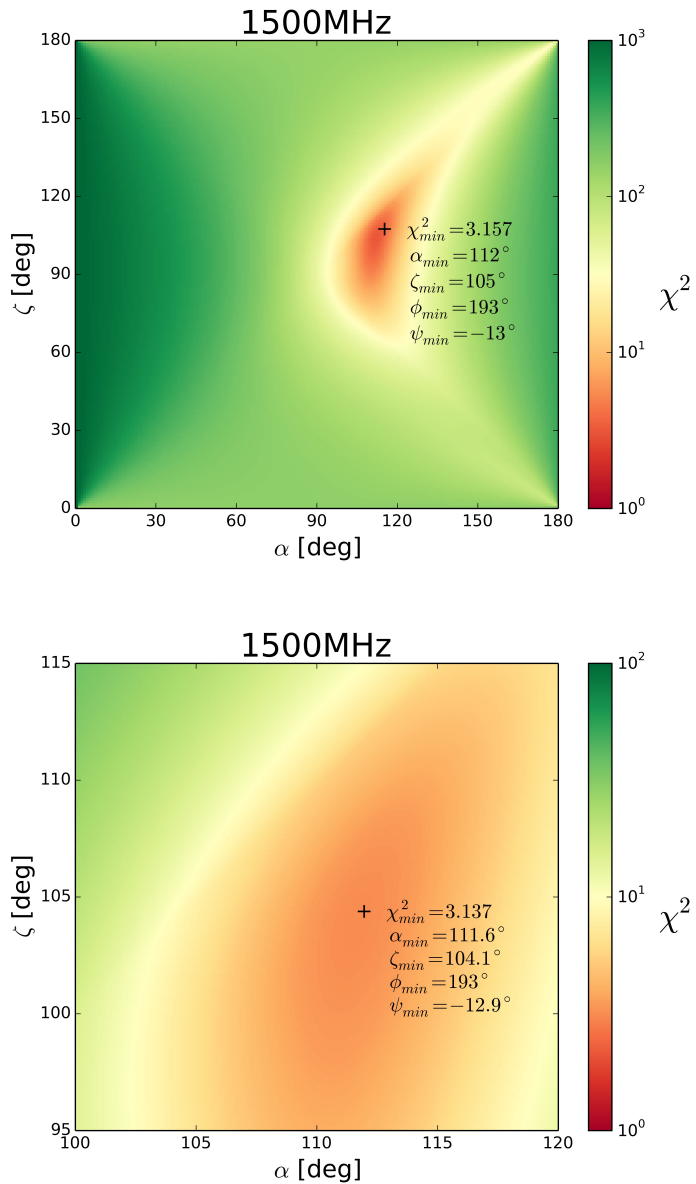


Figure 4.4.: The heat maps show the reduced χ^2 values as a function of (α, ζ) at 1500 MHz. At each point, χ^2 was minimized over the offset parameters ϕ_0 and ψ_0 . The best-fit values are marked by black crosses. Note that the color code for χ^2 has a logarithmic scale. The top heat map extends over the full range of the $(\alpha, \zeta, \phi_0, \psi_0)$ -space with a spacing of 1° . The full ranges of the parameter space are $0^\circ \leq \alpha \leq 180^\circ$, $0^\circ \leq \zeta \leq 180^\circ$, $0^\circ \leq \phi_0 \leq 360^\circ$ and $-90^\circ \leq \psi_0 \leq 90^\circ$. The bottom heat map has a finer spacing and a smaller individual grid size around the minimum of χ^2 . For 1500 MHz the grid size is set to $100^\circ \leq \alpha \leq 120^\circ$, $95^\circ \leq \zeta \leq 115^\circ$, $150^\circ \leq \phi_0 \leq 250^\circ$ and $-30^\circ \leq \psi_0 \leq 10^\circ$. The grid spacing for the parameters α , ζ and ψ_0 reduces to 0.1° . The grid spacing for ϕ_0 remains unchanged at 1° .

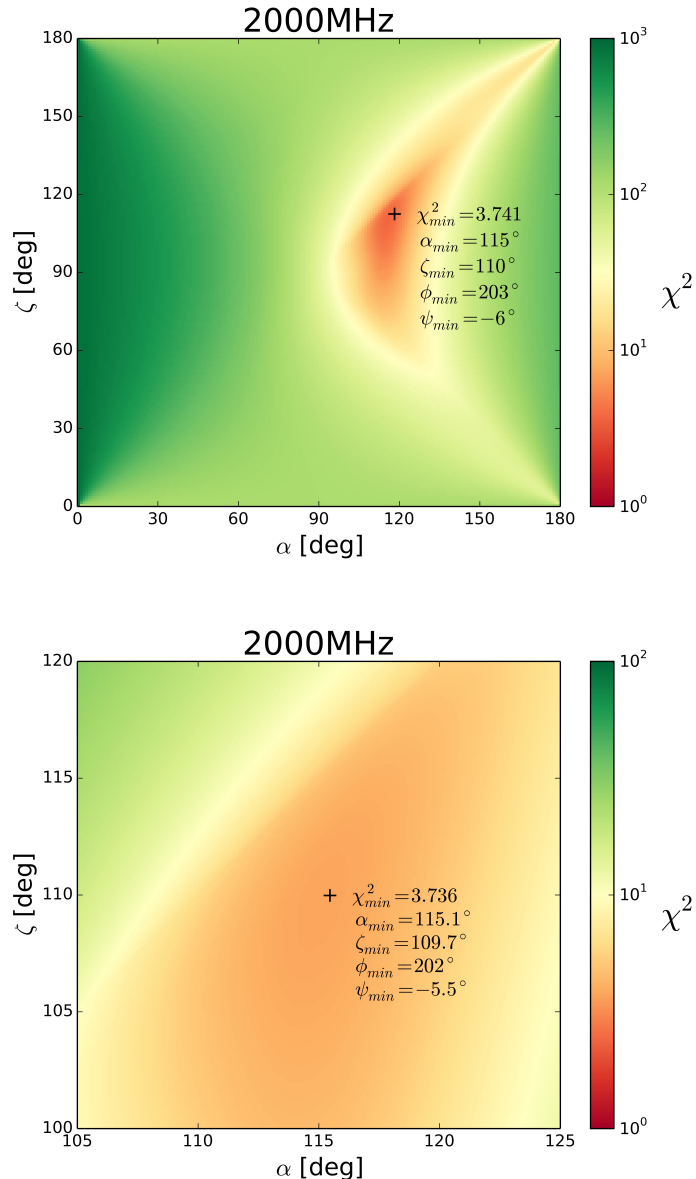


Figure 4.5.: The heat maps show the reduced χ^2 values as a function of (α, ζ) at 2000 MHz. At each point, χ^2 was minimized over the offset parameters ϕ_0 and ψ_0 . The best-fit values are marked by black crosses. Note that the color code for χ^2 has a logarithmic scale. Similar to Figure 4.4, the top heat map extends over the full range of the $(\alpha, \zeta, \phi_0, \psi_0)$ -space with a spacing of 1° . The bottom heat map has a finer spacing and a smaller individual grid size around the minimum of χ^2 . For 2000 MHz the grid size is set to $105^\circ \leq \alpha \leq 125^\circ$, $100^\circ \leq \zeta \leq 120^\circ$, $150^\circ \leq \phi_0 \leq 250^\circ$ and $-20^\circ \leq \psi_0 \leq 20^\circ$. The grid spacing for the parameters α , ζ and ψ_0 reduces to 0.1° . The grid spacing for ϕ_0 remains unchanged at 1° .

4.2. Discussion

Overall, the RVM prediction with the best-fit values reproduced the general form of the observed polarization position angle profiles (see Figure 4.2). The theoretical curve for the 1500 MHz data fits better than the theoretical curve for the 2000 MHz data to each measured polarization position angles, which is also expressed in the minimum χ^2 values of Table 4.1. However, both profiles exhibit deviations at the same pulse phases. The largest deviations are exhibited below pulse phase 0.2 and above pulse phase 0.9, while small visible deviations are exhibited around pulse phase 0.35 and 0.75. The 2000 MHz profile shows a remarkably big "bump" around pulse phase 0.2.

A graphical illustration of the emission beam geometry of PSR J2007+2722 is given in Figure 4.3. The observer expects to receive emission of both cones, when the conditions

$$\alpha^{\text{MP}} - \rho < \zeta < \alpha^{\text{MP}} + \rho, \quad (4.5)$$

$$\alpha^{\text{IP}} - \rho < \zeta < \alpha^{\text{IP}} + \rho. \quad (4.6)$$

are satisfied [19]. In other words, the line of sight should pass within both ends of the emission cone half-opening angle of the two magnetic poles. By using the values of Table 4.1 and the unusually broad emission cone half-opening angles ρ_{1500} and ρ_{2000} , it is straightforward to show that the geometry of PSR J2007+2722 satisfied the conditions (Equations 4.5 and 4.6) for 1500 and 2000 MHz. As a consequence, one would expect four separated peaks in the pulse profiles. However, there are only two peaks in the pulse profiles of PSR J2007+2722 (Figure 4.2), which leads to the conclusion that the emission from one cone should be much weaker than the emission of the other cone.

The radio flux-density S in intensity I of PSR J2007+2722 is described in Section 4.1.1 and its circularly polarized component V is conspicuously around zero. One particularity of the radio flux-density profiles is its linearly polarized component L . It takes a similar curve shape as the total intensity I , but with small variations. The total intensity I is approximately two times bigger than the linearly polarized component L . The position of the peaks of L are shifted to the center of the pulse profile for both observing frequencies, which causes an unusual gap between L and I at the outer edges of the pulse peaks.

4.2.1. Disregard the bump at 2000MHz

As mentioned above, the measured polarization position angle profile at 2000 MHz (see Figure 4.2) shows a remarkable "bump" around pulse phase 0.2. This is the biggest deviation from the theoretical RVM curve. Around pulse phase 0.2, the linearly polarized component L of the radio flux-density profile at 2000 MHz in Figure 4.2 is conspicuously small. In comparison to the rest of the profile, it is comprehensible to claim that the pulse phase region, which corresponds to the "bump", is almost completely depolarized. Similar to the analysis of PSR B1055-52 by S. C. Rookyard, S. Johnston, P. Weltevrede and G. Wright [19, 21], the data of the depolarized part is disregarded for the RVM fitting.

In Figure 4.6, the disregarded data points are marked red and the data points, which are used for the analysis, are marked green. By applying the codes (Appendix C) to the

modified 2000 MHz data of PSR J2007+2722, the best-fit parameters, which are listed in Table 4.2, are obtained and the resulting heat maps, which are shown in Figure 4.7, are created. The procedure of the analysis, which is explained in Section 4.1.2, remains unchanged.

It is not surprising that the minimum χ^2 value decreased from 3.736 to 2.728, since data points, which vary tremendously from the model, were disregarded. The best-fit RVM parameters (see Table 4.2), which are obtained from the analysis of the selected 2000 MHz data set, are remarkable. The inclination α from the rotation axis to the magnetic axis decreased from 115.1° to 113.2° and the inclination ζ from the rotation axis to the line of sight decreased from 109.7° to 104.3° . However, comparing the best-fit RVM parameters of the analysis of the 1500 MHz data set (see Table 4.1) and the best-fit RVM parameters of the analysis of the selected 2000 MHz data set (see Table 4.2) leads to an interesting correlation. The α value differs by $113.2^\circ - 111.6^\circ = 1.6^\circ$, while the ζ value only differs by $104.3^\circ - 104.1^\circ = 0.2^\circ$. The fact that the best-fit RVM parameters match well at different observing frequencies is a major step towards the understanding of the emission beam geometry of PSR J2007+2722.

4.2.2. Extending the RVM with interpulse

The reason why this project has started, was the promising attempt to explain the deviations and particularities of PSR J2007+2722 by extending the RVM with the interpulse (IP). Since the emission geometry of the majority of pulsars are not satisfied by both conditions (Equations 4.5 and 4.6), the conventional RVM (see Section 3.3) are only discussed using one emission cone in most of the literature. In this thesis, the IP and its polarization position angle ψ^{IP} was explicitly elaborated in Section 3.5.

The idea of the attempt is to describe the polarization position angle curve of PSR J2007+2722 with the superposition of the MP and the IP. As mentioned above, it is assumed from the pulse profile (see Figure 4.1) that the emission of the IP is supposed to be much weaker than the emission of the MP. Since the emission cone half-opening angle is approximately 78° , the angle between the two emission cones is 24° . According to the hollow cone model by M. M. Komesaroff [11], the emission intensity is the highest on the edges of the cones. As a consequence, the peaks in the pulse profile are identified with the edges of the MP emission cone. The peak positions of the IP emission cone is supposed to be 24° before the first peak and 24° after the second peak. These positions are deeply interesting, because the largest deviations of the observed polarization position angle profiles appear at these pulse phases.

The indicators above made this attempt so promising. However, it is impossible to describe deviations of the observed polarization position angle profiles with the superposition of the MP and the IP. During the project, it turned out that the polarization position angle ψ^{MP} of the MP is equal to the polarization position angle ψ^{IP} of the IP (see Equation 3.67). The general procedure of the attempt is carried out in Section 4.2.3 using the superposition of the MP and a fixed linear polarization.

ν	α	ζ	β	ϕ_0	ψ_0	ρ	χ^2
2000 MHz	113.2°	104.3°	-8.9°	195°	-3.7°	80.0°	2.728

Table 4.2.: The best-fit RVM parameters for PSR J2007+2722 are obtained from the analysis of a selected 2000 MHz data set (see Figure 4.6). In the last column, the minimum χ^2 values, which correspond to the best-fit RVM parameters, are listed. The impact parameter β represents the closest approach of the magnetic axis to the line of sight and is calculated with $\beta = \zeta - \alpha$. The emission cone half-opening angle ρ (Equation 4.4) is determined by the best-fit RVM parameters and the peak-to-peak width $W_{2000} = 107.2^\circ$.

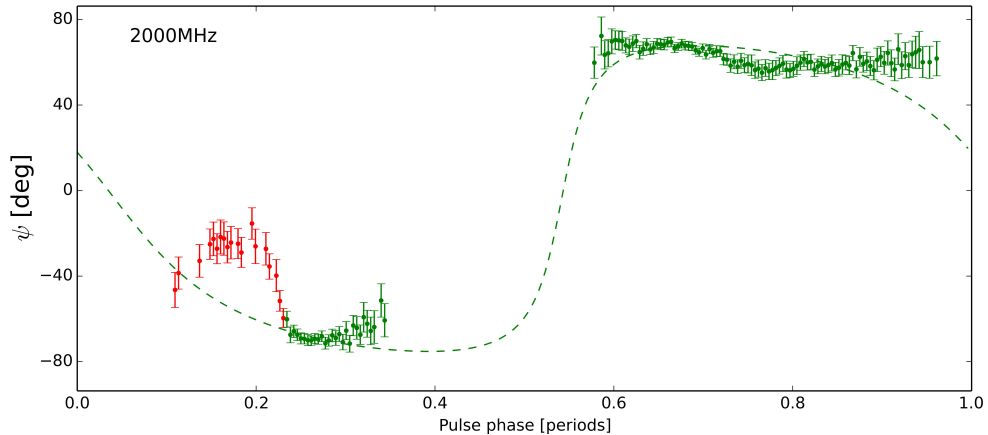


Figure 4.6.: This figure shows the derived polarization position angle ψ of Equation 4.1 as a function of the pulse phase, along with estimated measurement uncertainties $\Delta\psi$. The green dashed line depicts the theoretical curve ψ_{RVM} for the best-fit RVM parameters, given by Equation 4.2 and Table 4.2. The best-fit RVM parameters are obtained from the analysis of a selected data set, which are marked green. The data set, which is marked red, is disregarded for the analysis. The plot is constructed with a modified version of the Python code *J2007DisplayData.py*, which is shown in Appendix C.

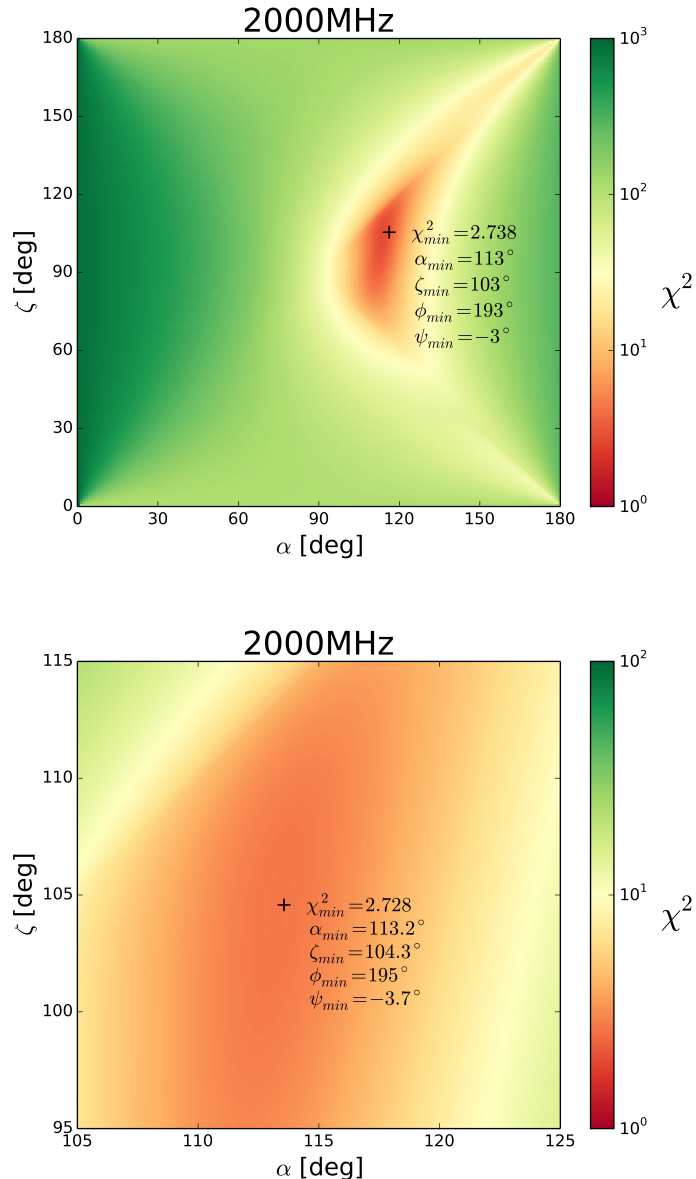


Figure 4.7.: The heat maps show the reduced χ^2 values for a selected data set as a function of (α, ζ) at 2000 MHz. At each point, χ^2 was minimized over the offset parameters ϕ_0 and ψ_0 . The best-fit values are marked by black crosses. Note that the color code for χ^2 has a logarithmic scale. Similar to Figure 4.4 and 4.5, the top heat map extends over the full range of the $(\alpha, \zeta, \phi_0, \psi_0)$ -space with a spacing of 1° . The bottom heat map has a finer spacing and a smaller individual grid size around the minimum of χ^2 . The grid size is set to $105^\circ \leq \alpha \leq 125^\circ$, $95^\circ \leq \zeta \leq 115^\circ$, $150^\circ \leq \phi_0 \leq 250^\circ$ and $-20^\circ \leq \psi_0 \leq 20^\circ$. The grid spacing for the parameters α , ζ and ψ_0 reduces to 0.1° . The grid spacing for ϕ_0 remains unchanged at 1° .

4.2.3. Background radiation model

The promising attempt to explain the deviations and particularities of PSR J2007+2722 with the superposition of the MP and the IP failed. However, the general procedure of the attempt is carried out in this section. In the following, this model is called *background radiation model* (BRM). Therefore the superposition

$$\vec{E}_{\text{Data}} = \vec{E}_{\text{RVM}} + \vec{E}_{\text{BG}} \quad (4.7)$$

of the pure pulsar radiation \vec{E}_{RVM} and a fixed linearly polarized radiation \vec{E}_{BG} from a radiated source behind the pulsar is assumed as background radiation. The observer measures the amplitude of the superposition $|\vec{E}_{\text{Data}}|^2$ and its polarization position angle ψ_{Data} (see Figure 4.2), while the amplitude of the fixed linearly polarized radiation $|\vec{E}_{\text{BG}}|^2$ and its polarization position angle ψ_{BG} are assumed.

The amplitude of the pure pulsar radiation is determined by

$$\begin{aligned} |\vec{E}_{\text{RVM}}|^2 &= |\vec{E}_{\text{Data}} - \vec{E}_{\text{BG}}|^2 \\ &= |\vec{E}_{\text{Data}}|^2 + |\vec{E}_{\text{BG}}|^2 - 2|\vec{E}_{\text{Data}}||\vec{E}_{\text{BG}}| \cos(\eta), \end{aligned} \quad (4.8)$$

where η is the angle between \vec{E}_{Data} and \vec{E}_{BG} . Depending on the sign of ψ_{Data} and assuming a positive ψ_{BG} , the angle η is determined by

$$\eta = \begin{cases} |\psi_{\text{BG}} - \psi_{\text{Data}}| & \text{if } \psi_{\text{Data}} \geq 0^\circ \\ \psi_{\text{BG}} + |\psi_{\text{Data}}| & \text{if } \psi_{\text{Data}} < 0^\circ. \end{cases} \quad (4.9)$$

The electric field vectors and their polarization position angles are depicted at one instant of time in Figure 4.8.

The goal is to set up a theoretical prediction of polarization position angle for the BRM and then to minimize the parameters with the χ^2 method (Equation 4.3) over the parameter space $(\alpha, \zeta, \phi_0, \psi_0, |\vec{E}_{\text{BG}}|^2, \psi_{\text{BG}})$. Taking Figure 4.8 into account, the components of \vec{E}_{Data} yield to

$$|\vec{E}_{\text{Data}}|^2 \sin \psi_{\text{Data}} = |\vec{E}_{\text{RVM}}|^2 \sin \psi_{\text{RVM}} + |\vec{E}_{\text{BG}}|^2 \sin \psi_{\text{BG}}, \quad (4.10)$$

$$|\vec{E}_{\text{Data}}|^2 \cos \psi_{\text{Data}} = |\vec{E}_{\text{RVM}}|^2 \cos \psi_{\text{RVM}} + |\vec{E}_{\text{BG}}|^2 \cos \psi_{\text{BG}}. \quad (4.11)$$

Dividing Equation 4.10 by 4.11 leads to the theoretical prediction of the BRM

$$\psi_{\text{BRM}} = \arctan \left(\frac{|\vec{E}_{\text{RVM}}|^2 \sin \psi_{\text{RVM}} + |\vec{E}_{\text{BG}}|^2 \sin \psi_{\text{BG}}}{|\vec{E}_{\text{RVM}}|^2 \cos \psi_{\text{RVM}} + |\vec{E}_{\text{BG}}|^2 \cos \psi_{\text{BG}}} \right), \quad (4.12)$$

where $|\vec{E}_{\text{RVM}}|^2$ and ψ_{RVM} are determined by Equation 4.8 and 4.2, respectively. By applying the BRM code (Appendix C) to ψ_{Data} , the best-fit parameters, which are listed in Table 4.3, are obtained and the resulting heat maps, which are shown in Figures 4.9 and 4.10, are created. The χ^2 values for the RVM fitting are reduced from 3.137 for 1500 MHz and 3.736 for 2000 MHz to 0.742 and 0.662, respectively.

In comparison to the RVM, the BRM contains two more parameters. Minimizing over the parameter space (α , ζ , ϕ_0 , ψ_0 , $|\vec{E}_{\text{BG}}|^2$, ψ_{BG}) increases the runtime extremely. This is why, the ranges of the parameters were constrained in the BRM code (Appendix C). From the studies of Section 4.1.2, the ranges of the RVM parameters were deducted. The ranges of the constant amplitude of the fixed linearly polarized radiation $|\vec{E}_{\text{BG}}|^2$ and its polarization position angle ψ_{BG} were set by trying multiple values. The ranges of the parameter space are listed in each caption of the Figures 4.9, 4.10 and 4.12.

Since the theoretical prediction of the BRM (Equation 4.12) depends on the amplitude of the pure pulsar radiation $|\vec{E}_{\text{RVM}}|^2$ (Equation 4.8), which depends on the amplitude of the data $|\vec{E}_{\text{Data}}|^2$, the theoretical curve is not smooth. For the Figures 4.11 and 4.13, a moving average was used to smooth the amplitude $|\vec{E}_{\text{RVM}}|^2$ and therewith the theoretical curve. The degree of smoothness varies with the box value. The box value is the number of data points, which are included in the averaging for each data points. For the top plot of Figure 4.11, the box value is 15, while for the bottom plot of Figure 4.11, the box value is 12. The box value for Figure 4.13 is also 12.

As mentioned in Section 4.2.1, the "bump" at 2000 MHz is almost completely depolarized. Disregarding the depolarized part improves the RVM fitting. The same procedure was executed for the BRM fitting. The best-fit parameters, which are obtained from the analysis of a selected data set, are listed in Table 4.4 and their corresponding heat maps are shown in Figure 4.12. Figure 4.13 shows the resulting theoretical curve for the BRM in comparison to the theoretical curve for the RVM of Figure 4.6. Even though the red points are disregarded for the analyses, the theoretical curve for the BRM makes a smaller "bump" at that appropriately pulse phase.

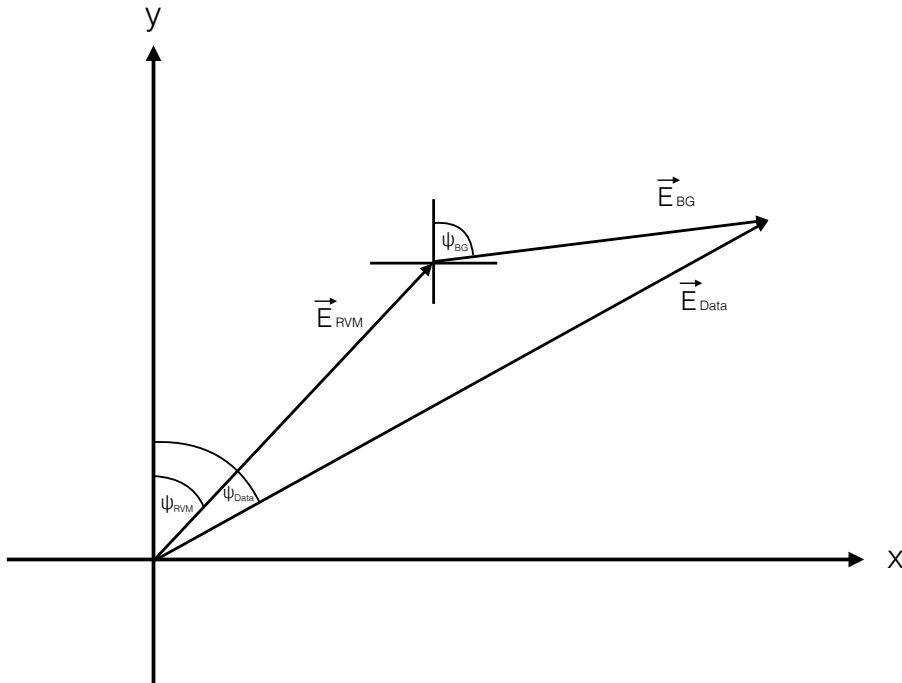


Figure 4.8.: This figure shows the superposition of two electric field vectors (Equation 4.7). The depicted angles ψ_{RVM} , ψ_{BG} and ψ_{Data} are the inclination from the y -axis to the corresponding electric fields.

ν	α	ζ	β	ϕ_0	ψ_0	ρ	$ \vec{E}_{\text{BG}} ^2$	ψ_{BG}	χ^2
1500 MHz	109°	109°	0°	149°	-5°	77.5°	0.8 mJy	54°	0.734
2000 MHz	108°	110°	2°	152°	6°	79.5°	0.85 mJy	60°	0.662

Table 4.3.: The best-fit BRM parameters are obtained from the analysis of the 1500 and 2000 MHz data. As mentioned in this section, a superposition of the pure pulsar radiation and the background radiation is assumed. The impact parameter β represents the closest approach of the magnetic axis to the line of sight and is calculated with $\beta = \zeta - \alpha$. The emission cone half-opening angle ρ (Equation 4.4) is determined by the best-fit parameters and the peak-to-peak width ($W_{1500} = 165.9^\circ$; $W_{2000} = 107.2^\circ$). As expected, the independent fits at 1500 and 2000 MHz lead to similar emission beam geometry parameters.

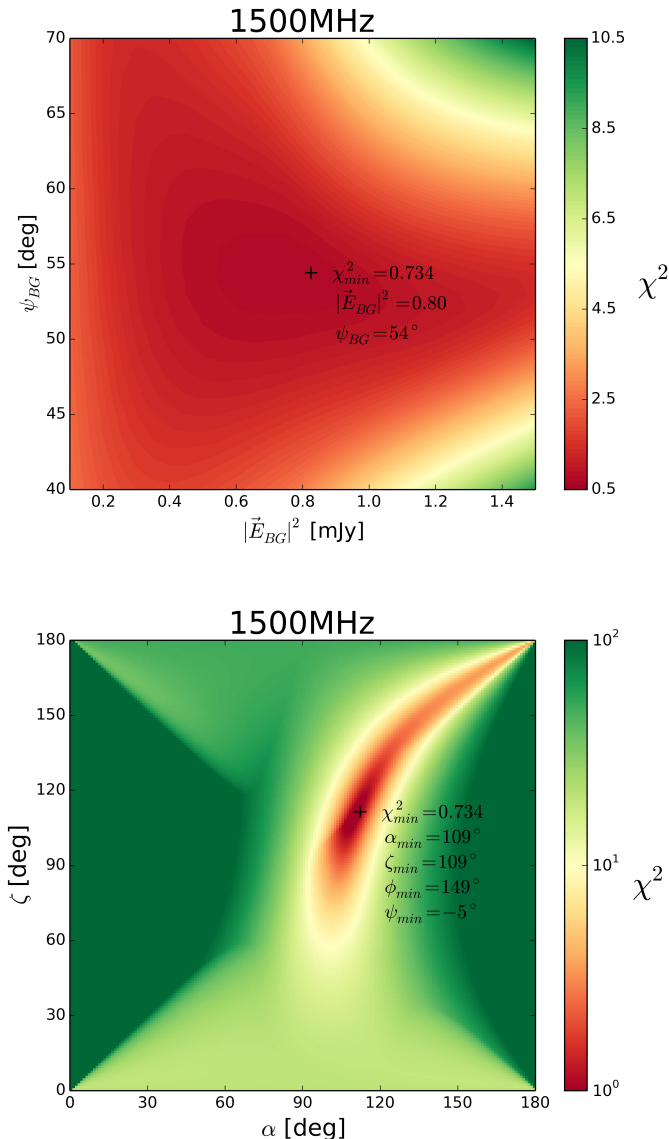


Figure 4.9.: The top heat map shows the reduced χ^2 values for the BRM as a function of $(|\vec{E}_{BG}|^2, \psi_{BG})$ at 1500 MHz. At each point, χ^2 was minimized over the RVM parameters α , ζ , ϕ_0 and ψ_0 . The best-fit value is marked by the black cross. The parameter space of the χ^2 analysis (top heat map) is $0.1 \text{ mJy} \leq |\vec{E}_{BG}|^2 \leq 1.5 \text{ mJy}$, $40^\circ \leq \psi_{BG} \leq 70^\circ$, $100^\circ \leq \alpha \leq 120^\circ$, $100^\circ \leq \zeta \leq 120^\circ$, $100^\circ \leq \phi_0 \leq 200^\circ$ and $-20^\circ \leq \psi_0 \leq 20^\circ$. The bottom heat map shows the reduced χ^2 values for $(|\vec{E}_{BG}|^2 = 0.8, \psi_{BG} = 54^\circ)$ as a function of (α, ζ) at 1500 MHz. At each point, χ^2 was minimized over the offset parameters ϕ_0 and ψ_0 . The best-fit value is marked by the black cross. Note that the color code for χ^2 has a logarithmic scale for the bottom heat map. The bottom heat map extends over the full range of the $(\alpha, \zeta, \phi_0, \psi_0)$ -space.

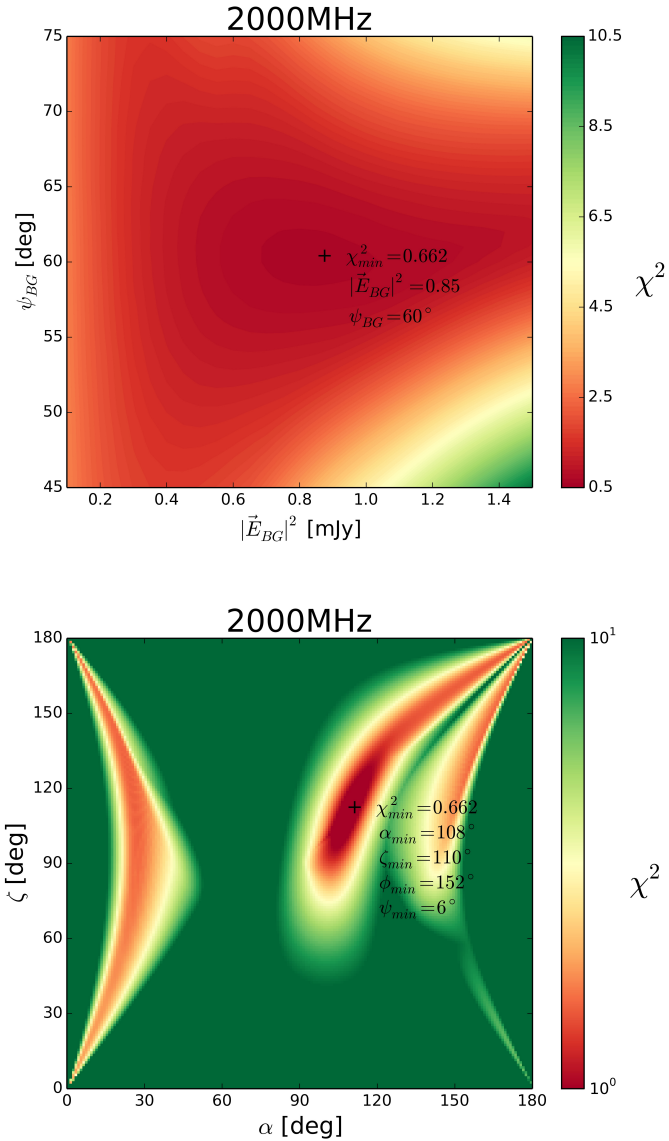


Figure 4.10.: The top heat map shows the reduced χ^2 values for the BRM as a function of $(|\vec{E}_{BG}|^2, \psi_{BG})$ at 2000 MHz. At each point, χ^2 was minimized over the RVM parameters α , ζ , ϕ_0 and ψ_0 . The best-fit value is marked by the black cross. The parameter space of the χ^2 analysis (top heat map) is $0.1 \text{ mJy} \leq |\vec{E}_{BG}|^2 \leq 1.5 \text{ mJy}$, $45^\circ \leq \psi_{BG} \leq 75^\circ$, $100^\circ \leq \alpha \leq 120^\circ$, $100^\circ \leq \zeta \leq 120^\circ$, $100^\circ \leq \phi_0 \leq 200^\circ$ and $-20^\circ \leq \psi_0 \leq 20^\circ$. The bottom heat map shows the reduced χ^2 values for $(|\vec{E}_{BG}|^2 = 0.85, \psi_{BG} = 60^\circ)$ as a function of (α, ζ) at 2000 MHz. At each point, χ^2 was minimized over the offset parameters ϕ_0 and ψ_0 . The best-fit value is marked by the black cross. Note that the color code for χ^2 has a logarithmic scale for the bottom heat map. The bottom heat map extends over the full range of the $(\alpha, \zeta, \phi_0, \psi_0)$ -space.

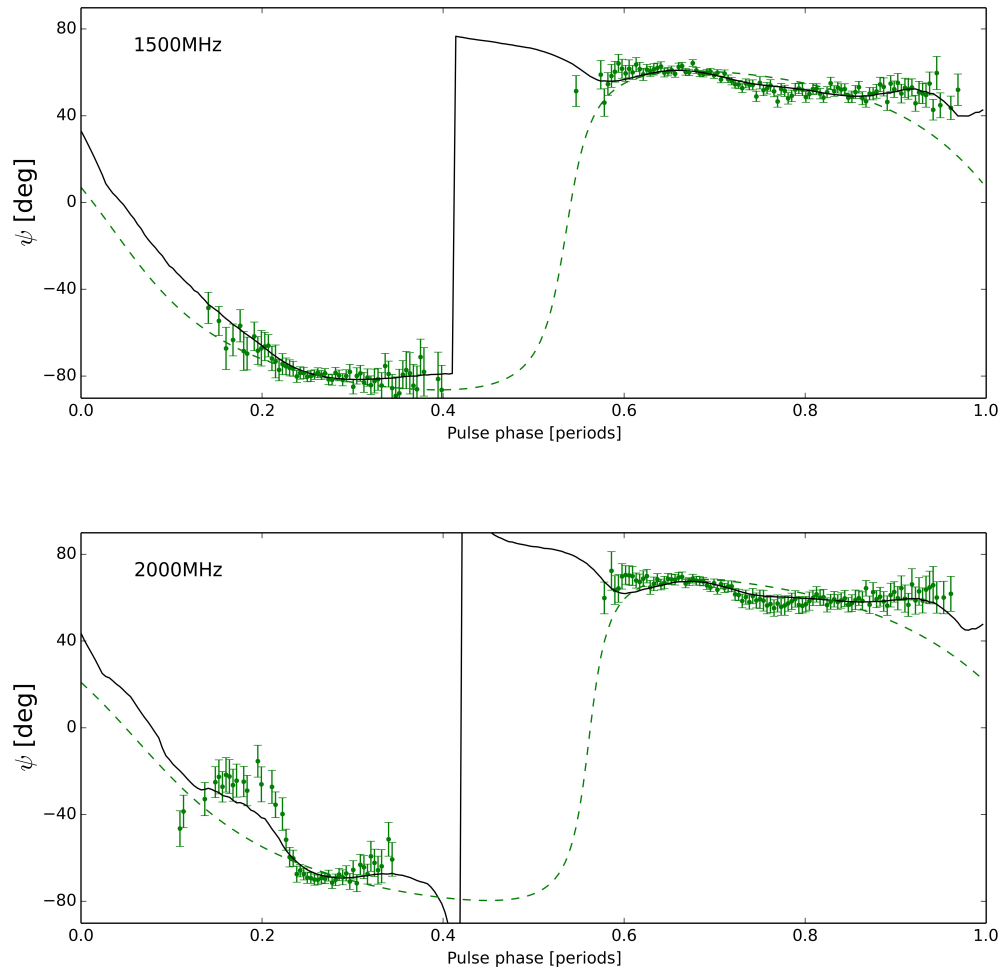


Figure 4.11.: This figure shows the derived polarization position angles ψ of Equation 4.1 at 1500 and 2000 MHz as a function of the pulse phase, along with estimated measurement uncertainties $\Delta\psi$. The green dashed line depicts the old theoretical curve ψ_{RVM} for the best-fit RVM parameters given by Table 4.1. The black line depicts the theoretical curve ψ_{BRM} for the best-fit BRM parameters given by Table 4.3. The plots are constructed with a modified version of the Python code *J2007DisplayData.py*, which is shown in Appendix C.

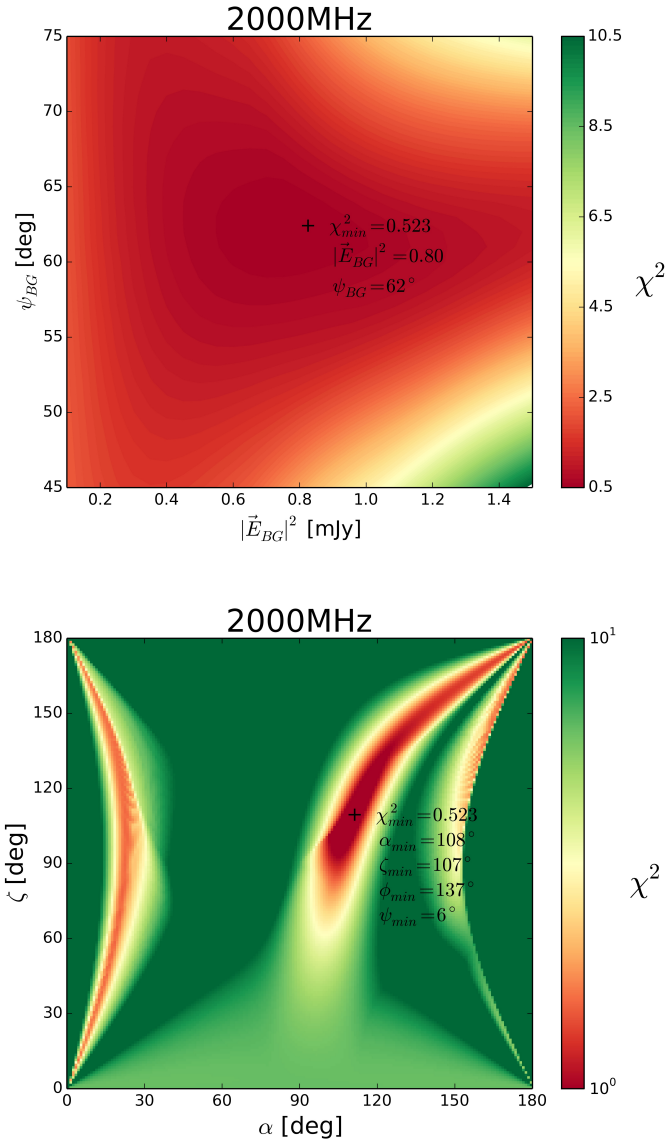


Figure 4.12.: The top heat map shows the reduced χ^2 values for a selected data set as a function of $(|\vec{E}_{BG}|^2, \psi_{BG})$ at 2000 MHz (BRM). At each point, χ^2 was minimized over the RVM parameters α , ζ , ϕ_0 and ψ_0 . The best-fit value is marked by the black cross. The parameter space of the χ^2 analysis (top heat map) is $0.1 \text{ mJy} \leq |\vec{E}_{BG}|^2 \leq 1.5 \text{ mJy}$, $45^\circ \leq \psi_{BG} \leq 75^\circ$, $100^\circ \leq \alpha \leq 120^\circ$, $100^\circ \leq \zeta \leq 120^\circ$, $100^\circ \leq \phi_0 \leq 200^\circ$ and $-20^\circ \leq \psi_0 \leq 20^\circ$. The bottom heat map shows the reduced χ^2 values for $(|\vec{E}_{BG}|^2 = 0.8, \psi_{BG} = 62^\circ)$ as a function of (α, ζ) at 2000 MHz (BRM). At each point, χ^2 was minimized over the offset parameters ϕ_0 and ψ_0 . The best-fit value is marked by the black cross. Note that the color code for χ^2 has a logarithmic scale for the bottom heat map. The bottom heat map extends over the full range of the $(\alpha, \zeta, \phi_0, \psi_0)$ -space.

ν	α	ζ	β	ϕ_0	ψ_0	ρ	$ \vec{E}_{\text{BG}} ^2$	ψ_{BG}	χ^2
2000 MHz	108°	107°	-1°	137°	6°	80.3°	0.8 mJy	62°	0.523

Table 4.4.: The best-fit BRM parameters for PSR J2007+2722 are obtained from the analysis of a selected 2000 MHz data set (see Figure 4.13). In the last column, the minimum χ^2 values, which correspond to the best-fit RVM parameters, are listed. The impact parameter β represents the closest approach of the magnetic axis to the line of sight and is calculated with $\beta = \zeta - \alpha$. The emission cone half-opening angle ρ (Equation 4.4) is determined by the best-fit parameters and the peak-to-peak width $W_{2000} = 107.2^\circ$.

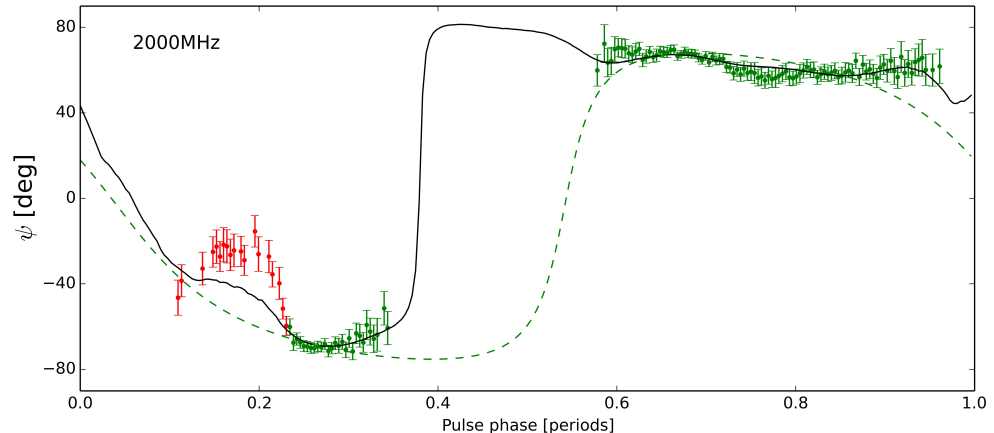


Figure 4.13.: This figure shows the derived polarization position angles ψ of Equation 4.1 at 2000 MHz as a function of the pulse phase, along with estimated measurement uncertainties $\Delta\psi$. The green dashed line depicts the old theoretical curve ψ_{RVM} for the best-fit RVM parameters given by Table 4.1. The black line depicts the theoretical curve ψ_{BRM} for the best-fit BRM parameters given by Table 4.4. The best-fit BRM parameters are obtained from the analysis of a selected data set, which are marked green. The data set, which is marked red, is disregarded for the analysis. The plots are constructed with a modified version of the Python code *J2007DisplayData.py*, which is shown in Appendix C.

5. Conclusion

This thesis gives an overview of the fundamentals of polarization, the theoretical background of radio pulsar astronomy and the emission beam geometry of pulsars. During the project, the previous study of PSR J2007+2722 by B. Allen and B. Knispel [2] has been confirmed and extended. Several attempts to explain the deviations and particularities of PSR J2007+2722 has been accomplished, since the conventional *rotational vector model* (RVM) only describes the data to a certain degree. The reason why this project started, was the attempt to extend the RVM with the interpulse (IP). This project outlines arguments that the consideration of the IP will not have an effect on the RVM fitting. To improve the fitting of the data, the almost completely depolarized part at 2000 MHz was disregarded for the RVM analysis. This leads to a more similar emission beam geometry at both observing frequencies.

The attempt to model the data with the superposition of the pulsar radiation and a fixed linearly polarized radiation seems to fit well for the 1500 and 2000 MHz data and the selected 2000 MHz data set. To make the statement more quantitative, the *bayesian information criterion* (BIC) of the RVM is calculated and then compared with the BIC of the *background radiation model* BRM. The BIC is determined by

$$\text{BIC} = k \cdot [\ln(n) - \ln(2\pi)] - 2 \cdot \ln(\hat{L}), \quad (5.1)$$

where \hat{L} is the likelihood function, k is the number of parameters estimated by the model and n is the number of data points. The likelihood function is calculated by

$$\hat{L} = \prod_{i=1}^n \frac{1}{\sqrt{2\pi(\Delta\psi_i)^2}} \exp\left(-\frac{(\psi_i - \tilde{\psi}_i)^2}{2(\Delta\psi_i)^2}\right), \quad (5.2)$$

where ψ_i is the observed data, $\tilde{\psi}_i$ is the theoretical value and $\Delta\psi_i$ is the measurement uncertainty [20, 22]. A model describes the observed data better as the BIC gets smaller. For the 1500 and 2000 MHz data, the BIC difference between the RVM and the BRM is $\Delta\text{BIC}_{1500} = \text{BIC}_{\text{RVM}} - \text{BIC}_{\text{BRM}} = 363.63$ and $\Delta\text{BIC}_{2000} = 421.03$, respectively. For the selected 2000 MHz data set, the BIC difference between the RVM and the BRM is $\Delta\text{BIC}_{2000'} = 258.55$. The effort of developing the BRM is worthwhile, because the model describes the data of PSR J2007+2722 much better than the conventional RVM.

As a possible further investigation, one could study the radio sources in space. It would be very interesting to know, if any radio source has the ability to cause a background radiation as assumed in the BRM. Another difficulty to face, would be the detection and the identification of the background radiation source in the region close to PSR

J2007+2722. However, it could also be possible that the assumed background radiation in the BRM is caused by the instruments of measuring or a noise source near the telescope.

A. Symmetric and antisymmetric functions

Definition A.1. Let $f(x)$ be a real-valued function of a real variable.

a) Then f is *symmetric/even* if

$$f(x) = f(-x)$$

holds for all x and $-x$ in the domain of f .

b) Then f is *antisymmetric/odd* if

$$f(x) = -f(-x)$$

holds for all x and $-x$ in the domain of f .

Corollary A.2. Let $f_1(x)$ and $g_1(x)$ be symmetric functions. The product $h_1(x) = f_1(x) \cdot g_1(x)$ is symmetric.

Proof. According to definition, $f_1(x) = f_1(-x)$ and $g_1(x) = g_1(-x)$. Thus,

$$\begin{aligned} h_1(x) &= f_1(x) \cdot g_1(x) \\ &= f_1(-x) \cdot g_1(-x) \\ &= h_1(-x). \end{aligned}$$

□

Corollary A.3. Let $f_2(x)$ and $g_2(x)$ be antisymmetric functions. The product $h_2(x) = f_2(x) \cdot g_2(x)$ is symmetric.

Proof. According to definition, $f_2(x) = -f_2(-x)$ and $g_2(x) = -g_2(-x)$. Thus,

$$\begin{aligned} h_2(x) &= f_2(x) \cdot g_2(x) \\ &= -f_2(-x) \cdot (-g_2(-x)) \\ &= f_2(-x) \cdot g_2(-x) \\ &= h_2(-x). \end{aligned}$$

□

Corollary A.4. Let $f_3(x)$ be a symmetric function and $g_3(x)$ an antisymmetric function. The product $h_3(x) = f_3(x) \cdot g_3(x)$ is antisymmetric.

Proof. According to definition, $f_3(x) = f_3(-x)$ and $g_3(x) = -g_3(-x)$. Thus,

$$\begin{aligned} h_3(x) &= f_3(x) \cdot g_3(x) \\ &= f_3(-x) \cdot (-g_3(-x)) \\ &= -f_3(-x) \cdot g_3(-x) \\ &= -h_3(-x). \end{aligned}$$

□

Theorem A.5. If $a \in \mathbb{R}$ and $f_{sym}(x)$ be a symmetric function, then

$$\int_{-a}^{+a} f_{sym}(x) dx = 2 \int_0^{+a} f_{sym}(x) dx.$$

Proof. According to definition, $f_{sym}(x) = f_{sym}(-x)$. In the second step the substitution $t = -x$ is made, that obtain $dt = -dx$. Thus,

$$\begin{aligned} \int_{-a}^{+a} f_{sym}(x) dx &= \int_{-a}^0 f_{sym}(x) dx + \int_0^{+a} f_{sym}(x) dx \\ &= \int_{+a}^0 -f_{sym}(-t) dt + \int_0^{+a} f_{sym}(x) dx \\ &= \int_0^{+a} f_{sym}(-t) dt + \int_0^{+a} f_{sym}(x) dx \\ &= \int_0^{+a} f_{sym}(t) dt + \int_0^{+a} f_{sym}(x) dx \\ &= 2 \int_0^{+a} f_{sym}(x) dx. \end{aligned} \quad \square$$

Theorem A.6. If $a \in \mathbb{R}$ and $f_{asym}(x)$ be an antisymmetric function, then

$$\int_{-a}^{+a} f_{asym}(x) dx = 0.$$

Proof. According to definition, $f_{asym}(-x) = -f_{asym}(x)$. In the second step the substi-

tution $t = -x$ is made, that obtain $dt = -dx$. Thus,

$$\begin{aligned}
\int_{-a}^{+a} f_{asym}(x) dx &= \int_{-a}^0 f_{asym}(x) dx + \int_0^{+a} f_{asym}(x) dx \\
&= \int_{+a}^0 -f_{asym}(-t) dt + \int_0^{+a} f_{asym}(x) dx \\
&= \int_0^{+a} f_{asym}(-t) dt + \int_0^{+a} f_{asym}(x) dx \\
&= \int_0^{+a} -f_{asym}(t) dt + \int_0^{+a} f_{asym}(x) dx \\
&= 0.
\end{aligned}$$

□

III

B. Additional calculations

Orientation angle of the polarization ellipse

Calculation B.1.

$$\begin{aligned}
 & \frac{E_{0x} \cos \delta_x \cos \psi + E_{0y} \cos \delta_y \sin \psi}{E_{0x} \sin \delta_x \cos \psi + E_{0y} \sin \delta_y \sin \psi} = \frac{E_{0x} \sin \delta_x \sin \psi - E_{0y} \sin \delta_y \cos \psi}{-E_{0x} \cos \delta_x \sin \psi + E_{0y} \cos \delta_y \cos \psi} \\
 \Leftrightarrow & (E_{0y}^2 \cos^2 \delta_y - E_{0x}^2 \cos^2 \delta_x) \cos \psi \sin \psi \quad (E_{0x}^2 \sin^2 \delta_x - E_{0y}^2 \sin^2 \delta_y) \cos \psi \sin \psi \\
 & + E_{0x} E_{0y} \cos \delta_x \cos \delta_y (\cos^2 \psi - \sin^2 \psi) \quad - E_{0x} E_{0y} \sin \delta_x \sin \delta_y (\cos^2 \psi - \sin^2 \psi) \\
 \Leftrightarrow & E_{0x} E_{0y} (\cos \delta_x \cos \delta_y + \sin \delta_x \sin \delta_y) \quad E_{0x}^2 \cos \psi \sin \psi (\cos^2 \delta_x + \sin^2 \delta_x) \\
 & \cdot (\cos^2 \psi - \sin^2 \psi) \quad - E_{0y}^2 \cos \psi \sin \psi (\cos^2 \delta_y + \sin^2 \delta_y) \\
 \Leftrightarrow & E_{0x} E_{0y} \cos \delta \cos 2\psi = \frac{(E_{0x}^2 - E_{0y}^2)}{2} \sin 2\psi \\
 \Leftrightarrow & \tan 2\psi = \frac{2E_{0x} E_{0y} \cos \delta}{(E_{0x}^2 - E_{0y}^2)}
 \end{aligned}$$

Oblique rotator

Calculation B.2.

$$\begin{aligned}
 \vec{E}_{ob}^{int} \cdot \vec{B}_{ob} &= \frac{\Omega B_0^2}{4c} \frac{R^6}{r^5} \begin{pmatrix} 2(\cos \theta \cos \alpha + \sin \theta \sin \alpha \cos \phi_s) \\ \sin \theta \cos \alpha - \cos \theta \sin \alpha \cos \phi_s \\ \sin \alpha \sin \phi_s \end{pmatrix} \\
 &\quad \cdot \begin{pmatrix} \sin^2 \theta \cos \alpha - \sin \theta \cos \theta \sin \alpha \cos \phi_s \\ -2(\sin \theta \cos \theta \cos \alpha + \sin^2 \theta \sin \alpha \cos \phi_s) \\ 0 \end{pmatrix} \\
 &= \frac{\Omega B_0^2}{4c} \frac{R^6}{r^5} \cdot \left[\begin{array}{l} \underbrace{2 \sin^2 \theta \cos \theta \cos^2 \alpha}_{\textcircled{1}} - \underbrace{2 \sin \theta \cos^2 \theta \sin \alpha \cos \alpha \cos \phi_s}_{\textcircled{2}} \\ + \underbrace{2 \sin^3 \theta \sin \alpha \cos \alpha \cos \phi_s}_{\textcircled{3}} - \underbrace{2 \sin^2 \theta \cos \theta \sin^2 \alpha \cos^2 \phi_s}_{\textcircled{4}} \\ - \underbrace{2 \sin^2 \theta \cos \theta \cos^2 \alpha}_{\textcircled{1}} - \underbrace{2 \sin^3 \theta \sin \alpha \cos \alpha \cos \phi_s}_{\textcircled{3}} \\ + \underbrace{2 \sin \theta \cos^2 \theta \sin \alpha \cos \alpha \cos \phi_s}_{\textcircled{2}} + \underbrace{2 \sin^2 \theta \cos \theta \sin^2 \alpha \cos^2 \phi_s}_{\textcircled{4}} \end{array} \right] \\
 &= 0
 \end{aligned}$$

Calculation B.3.

$$\begin{aligned}
(\vec{E}_{ob}^{ext} \cdot \vec{B}_{ob})|_{r=R} &= \frac{\Omega B_0^2 R}{4c} \begin{pmatrix} 2(\cos \theta \cos \alpha + \sin \theta \sin \alpha \cos \phi_s) \\ \sin \theta \cos \alpha - \cos \theta \sin \alpha \cos \phi_s \\ \sin \alpha \sin \phi_s \end{pmatrix} \\
&\quad \cdot \begin{pmatrix} \cos \alpha - 3 \cos^2 \theta \cos \alpha - 3 \sin \theta \cos \theta \sin \alpha \cos \phi_s \\ \sin \alpha \cos \phi_s (\cos^2 \theta - \sin^2 \theta) - \sin \alpha \cos \phi_s - 2 \sin \theta \cos \theta \sin \alpha \cos \alpha \\ 0 \end{pmatrix} \\
&= \frac{\Omega B_0^2 R}{4c} \cdot \left[2 \cos \theta \cos^2 \alpha - 6 \cos^3 \theta \cos^2 \alpha - 6 \sin \theta \cos^2 \theta \sin \alpha \cos \alpha \cos \phi_s \right. \\
&\quad + 2 \sin \theta \sin \alpha \cos \alpha \cos \phi_s - 6 \sin \theta \cos^2 \theta \sin \alpha \cos \alpha \cos \phi_s \\
&\quad - 6 \sin^2 \theta \cos \theta \sin^2 \alpha \cos^2 \phi_s + \sin \theta \cos^2 \theta \sin \alpha \cos \alpha \cos \phi_s \\
&\quad - \frac{\sin^3 \theta}{\sin \theta (1 - \cos^2 \theta)} \sin \alpha \cos \alpha \cos \phi_s - \sin \theta \sin \alpha \cos \alpha \cos \phi_s \\
&\quad - 2 \frac{\sin^2 \theta}{1 - \cos^2 \theta} \cos \theta \cos^2 \alpha - \frac{\cos^3 \theta}{\cos \theta (1 - \sin^2 \theta)} \sin^2 \alpha \cos^2 \phi_s \\
&\quad + \sin^2 \theta \cos \theta \sin^2 \alpha \cos^2 \phi_s + \cos \theta \sin^2 \alpha \cos^2 \phi_s \\
&\quad \left. + 2 \sin \theta \cos^2 \theta \sin \alpha \cos \alpha \cos \phi_s \right] \\
&= \frac{\Omega B_0^2 R}{4c} \cdot \left[\underbrace{2 \cos \theta \cos^2 \alpha}_{\textcircled{1}} - \underbrace{6 \cos^3 \theta \cos^2 \alpha}_{\textcircled{2}} - \underbrace{6 \sin \theta \cos^2 \theta \sin \alpha \cos \alpha \cos \phi_s}_{\textcircled{3}} \right. \\
&\quad + \underbrace{2 \sin \theta \sin \alpha \cos \alpha \cos \phi_s}_{\textcircled{4}} - \underbrace{6 \sin \theta \cos^2 \theta \sin \alpha \cos \alpha \cos \phi_s}_{\textcircled{3}} \\
&\quad - \underbrace{6 \sin^2 \theta \cos \theta \sin^2 \alpha \cos^2 \phi_s}_{\textcircled{5}} + \underbrace{\sin \theta \cos^2 \theta \sin \alpha \cos \alpha \cos \phi_s}_{\textcircled{3}} \\
&\quad - \underbrace{\sin \theta \sin \alpha \cos \alpha \cos \phi_s}_{\textcircled{4}} + \underbrace{\sin \theta \cos^2 \theta \sin \alpha \cos \alpha \cos \phi_s}_{\textcircled{3}} \\
&\quad - \underbrace{\sin \theta \sin \alpha \cos \alpha \cos \phi_s}_{\textcircled{4}} - \underbrace{2 \cos \theta \cos^2 \alpha}_{\textcircled{1}} + \underbrace{2 \cos^3 \theta \cos^2 \alpha}_{\textcircled{2}} \\
&\quad - \underbrace{\cos \theta \sin^2 \alpha \cos^2 \phi_s}_{\textcircled{6}} + \underbrace{\sin^2 \theta \cos \theta \sin^2 \alpha \cos^2 \phi_s}_{\textcircled{5}} \\
&\quad + \underbrace{\sin^2 \theta \cos \theta \sin^2 \alpha \cos^2 \phi_s}_{\textcircled{5}} + \underbrace{\cos \theta \sin^2 \alpha \cos^2 \phi_s}_{\textcircled{6}} \\
&\quad \left. + \underbrace{2 \sin \theta \cos^2 \theta \sin \alpha \cos \alpha \cos \phi_s}_{\textcircled{3}} \right] \\
&= -\frac{\Omega B_0^2 R}{c} \cdot \cos \theta \left[\cos^2 \theta \cos^2 \alpha + \sin^2 \theta \sin^2 \alpha \cos^2 \phi_s \right. \\
&\quad \left. + 2 \sin \theta \cos \theta \sin \alpha \cos \alpha \cos \phi_s \right]
\end{aligned}$$

C. Codes

Displaying the data of PSR J2007+2722

```
# -*- coding: utf-8 -*-
#!/usr/bin/python
#
#   J2007DisplayData.py
#
#   Created by Tjark Miener and Bruce Allen on 10.08.17.
#   Copyright (c) 2017 Tjark Miener and Bruce Allen. All rights reserved.
#

import numpy as np
import matplotlib.pyplot as plt

#Degrees to Radians conversion.
def deg2rad(val):
    return val*np.pi/180
#Radians to Degrees conversion.
def rad2deg(val):
    return val*180/np.pi
#Equation of the theoretical polarization position angle psi. All arguments
#in the head of the function are in radians, except the variable phi.
def position_angle(alpha, zeta, phi, phi0, psi0):
    x=-(np.sin(zeta)*np.cos(alpha)-np.cos(zeta)*np.sin(alpha)*np.cos(phi-
        phi0))
    y=np.sin(phi-phi0)*np.sin(alpha)
    return np.arctan2(y,x) + psi0

def main():
    #Change MHZ for working with the 2000MHz profile!
    MHZ = '1500'
    file = open("J2007_%sMHz_profile.txt" % MHZ, "r")
    data = np.loadtxt(file, dtype=str, delimiter='\n')
    #Reading the data and writing it into arrays.
    for line in xrange(0, len(data)):
        if line==0:
            d=data[line].split()
            intensitaetI=[float(d[3])]
            linearQ=[float(d[4])]
            linearU=[float(d[5])]
            linearL=[np.sqrt(np.power(float(d[4]),2)+np.power(float(d[5]),
                2))]
            circularV=[float(d[6])]
            psi=[float(d[7])]
            err=[float(d[8])]
```

```

    else :
        d=data[ line ].split( )
        intensitaetI.append( float(d[3]) )
        linearQ.append( float(d[4]) )
        linearU.append( float(d[5]) )
        linearL.append( np.sqrt(np.power( float(d[4]) ,2)+np.power( float(d[5]) ,2)) )
        circularV.append( float(d[6]) )
        psi.append( float(d[7]) )
        err.append( float(d[8]) )

    file .close()

#In the following only non-zero value of psi and error of psi are used.
psi=np.asarray(psi)
err=np.asarray(err)
psi_index=np.where( psi!=0.0)
err_index=np.where( err!=0.0)

#The pulse phase phi is discretized with the help of the index x (
#       number of measurements).
x=np.arange(0.0,256.0,1.0)
phi=2*np.pi*x/256
#Calculating the theoretical psi with the resulting values of the RVM
#       analysis .
if MHZ=='1500':
    alpha=deg2rad(111.6)
    zeta=deg2rad(104.1)
    phi0=deg2rad(193)
    psi0=deg2rad(-12.9)
    psi_theo=position_angle(alpha,zeta,phi,phi0,psi0)
    print "J2007_%sMHz_profile.txt" % MHZ
if MHZ=='2000':
    alpha=deg2rad(115.1)
    zeta=deg2rad(109.7)
    phi0=deg2rad(202)
    psi0=deg2rad(-5.5)
    psi_theo=position_angle(alpha,zeta,phi,phi0,psi0)
    print "J2007_%sMHz_profile.txt" % MHZ

#Creating the plots in figure 1 to see the results .
plt.figure(figsize=(9,7.2))
#The first subplot (top) is the measured and the theoretical
#       polarization angle psi as a function of pulse phase.
plt.subplot(211)
plt.plot(phi/(2*np.pi),rad2deg(psi_theo),'g—',label='theo PA')
plt.errorbar((x/256)[psi_index], psi[psi_index], err[err_index], fmt='g'
., ecolor='g',label='measured PA')
plt.xlim(0,1)
plt.ylim(-90+psi0,90+psi0)
plt.yticks([-80,-40,0,40,80])
plt.xlabel('Pulse phase [periods]')
plt.ylabel(r'$\psi$ [deg]', fontsize=18)
plt.xlim(0,1)

```

```

#The second subplot (bottom) is the different radio flux-density S as a
# function of pulse phase.
plt.subplot(212)
plt.plot(x/256,intensitaetI,'g-',label='I')
plt.plot(x/256,linearL,'y--',label='L')
plt.plot(x/256,circularV,'k-.',label='V')
plt.text(0.03,6.2,"%sMHz" % MHZ, fontsize=14)
plt.xlim(0,1)
plt.ylim(-1,7)
plt.yticks([0,3,6])
lg=plt.legend(loc='upper right')
lg.draw_frame(False)
plt.xlabel('Pulse phase [periods]')
plt.ylabel(r'$S$ [mJy]', fontsize=16)

# Saving the plots.
plt.savefig("J2007_%sMHz_profilePlot.png" % MHZ, dpi = 600)

#Execute the main function.
if __name__ == "__main__":
    main()

```

Applying the RVM to the data of PSR J2007+2722

Calculation of χ^2 values over $(\alpha, \zeta, \phi_0, \psi_0)$

```
//  
// chi_squared.c  
//  
// Created by Tjark Miener and Bruce Allen on 17.08.17.  
// Copyright (c) 2017 Tjark Miener and Bruce Allen. All rights reserved.  
  
#include <stdio.h>  
#include <stdlib.h>  
#include <math.h>  
  
//To compile this code on a Linux machine, the constant M_PI (actually a  
//constant from math.h) has to be defined manually.  
#ifndef M_PI  
#define M_PI 3.14159265358979323846  
#endif  
  
struct Data{  
    int index;           // 0,...,255  
    float intensityI;  
    float linearQ;  
    float linearU;  
    float linearL;  
    float circularV;  
    float psi;  
    float psi_error;  
};  
struct Data list[256];  
  
//Degrees to radians conversion.  
double deg2rad(float val){  
    return val*M_PI/180.0;  
}  
//Radians to degrees conversion.  
float rad2deg(double val){  
    return val*180.0/M_PI;  
}  
  
//All arguments in the head of the function are in radians, except the  
//variable called 'index'. The returning position angle is declared in  
//degrees.  
double positionAngle(float alpha, float zeta, int index, float phi0, float  
    psi0) {  
    double phi_rad=index*2*M_PI/256.0;  
    //Calculating the position angle with the rotating vector model (RVM).  
    double x=-(sin(zeta)*cos(alpha)-cos(zeta)*sin(alpha)*cos(phi_rad-phi0));  
    double y=sin(phi_rad-phi0)*sin(alpha);  
    return rad2deg(atan2(y,x)) + psi0;  
}
```

X

```

//main function
int main ( int argc , char** argv ) {

    //Initialization of helpful variables.
    int i , counter , counterA , counterB ;
    float alpha_val[3] , zeta_val[3] , psi0_val[3];
    int phi0_val[3];

    //For reasons of parallelizing the code , two variables from the console
    //mark the start and end of the alpha values . The third value of the
    //array is the iteration size .
    alpha_val[0]=atof(argv[2]);
    alpha_val[1]=atof(argv[3]);
    alpha_val[2]=1.0;    //0.1 for the finer grid

    //Bin size for the heatmap , which the python code 'J2007heatmap.py' will
    //visualize .
    int alpha_bins=(int)(alpha_val[1]-alpha_val[0]);      //((int)((alpha_val
    [1]-alpha_val[0])*10) for the finer grid
    int zeta_bins=181; //201 for the finer grid
    double chi[alpha_bins][zeta_bins];
    int phi0_minArray[alpha_bins][zeta_bins];
    float psi0_minArray[alpha_bins][zeta_bins];

FILE *input_file=fopen(argv[1],"r");
int file_index=atoi(argv[2]);
char str[35];
//Detecting if the input file is the profile of 1500MHz or 2000MHz.
if (argv[1][6]== '1') {
    sprintf(str , "J2007_1500MHz_Chi%d.txt" , file_index );
    zeta_val[0]=0.0;        //95.0 for the finer grid
    zeta_val[1]=180.0;      //115.0 for the finer grid
    zeta_val[2]=1.0;        //0.1 for the finer grid
    phi0_val[0]=0;          //150 for the finer grid
    phi0_val[1]=360;         //250 for the finer grid
    phi0_val[2]=1;          //1 for the finer grid
    psi0_val[0]=-90.0;      //-30.0 for the finer grid
    psi0_val[1]=90.0;        //10.0 for the finer grid
    psi0_val[2]=1.0;        //0.1 for the finer grid
} else if (argv[1][6]== '2') {
    sprintf(str , "J2007_2000MHz_Chi%d.txt" , file_index );
    zeta_val[0]=0.0;        //100.0 for the finer grid
    zeta_val[1]=180.0;      //120.0 for the finer grid
    zeta_val[2]=1.0;        //0.1 for the finer grid
    phi0_val[0]=0;          //150 for the finer grid
    phi0_val[1]=360;         //250 for the finer grid
    phi0_val[2]=1;          //1 for the finer grid
    psi0_val[0]=-90.0;      //-20.0 for the finer grid
    psi0_val[1]=90.0;        //20.0 for the finer grid
    psi0_val[2]=1.0;        //0.1 for the finer grid
} else {
    printf("Error! Inputfile %s is wrong!\n" , argv[1]);
    exit(1);
}

```

```

FILE *output_file=fopen(str,"w");

if (!input_file) {
    printf("Error! Inputfile %s not found\n", argv[1]);
    exit(2);
}
if (!output_file) {
    printf("Error! Outputfile %s not found\n", str);
    exit(3);
}

//Reading the input data and writing it into the structure (struct Data).
counter=0;
while (1) {
    int foobar1,foobar2;
    if (9==(i=fscanf(input_file,"%d %d %d %f %f %f %f %f %f\n",&foobar1,&
        foobar2,&list[counter].index,&list[counter].intensityI,&list[
        counter].linearQ,&list[counter].linearU,&list[counter].circularV,&
        list[counter].psi,&list[counter].psi_error))) {
        list[counter].linearL=sqrt(pow(list[counter].linearQ,2)+pow(list [
            counter].linearU,2));
        counter++;
    } else break;
}
if (i!=EOF) {
    fprintf(stderr, "Error! Problem reading %s at line %d . fscanf()
        returned %d\n", argv[1], counter+1,i);
    exit(4);
}

//Calculating the prefactor of the Chi^2 Equation.
float n=0.0;
for (int i=0; i<=255;i++) {
    if (list[i].psi!=0 && list[i].psi_error!=0) {
        n+=1.0;
    }
}
double prefactor=1.0/(n-4.0);

//Minimizing Chi^2 over the parameter space (alpha,zeta,phi0,psi0).
alpha_val[1]=-1.0;           //0.1 for the finer grid
counterA=-1;
for (float alpha=alpha_val[0]; alpha<=alpha_val[1]; alpha+=alpha_val[2])
{
    double alpha_rad=deg2rad(alpha);
    counterA+=1;
    counterB=-1;
    for (float zeta=zeta_val[0]; zeta<=zeta_val[1]; zeta+=zeta_val[2]) {
        printf("Iteration: alpha=%1f (%.1f-%.1f); zeta=%1f\n",alpha ,
            alpha_val[0],alpha_val[1],zeta);
        double zeta_rad=deg2rad(zeta);
        counterB+=1;
        for (int phi0=phi0_val[0]; phi0<=phi0_val[1]; phi0+=phi0_val[2]) {
            double phi0_rad=deg2rad(phi0);

```

```

for (float psi0=psi0_val[0]; psi0<=psi0_val[1]; psi0+=psi0_val[2])
{
    //Calculating the Chi^2 for one point of the parameter space.
    double psi_theo[256];
    double sum=0.0;
    for (int i=0; i<=255;i++) {
        if (list[i].psi!=0 && list[i].psi_error!=0) {
            psi_theo[i]=positionAngle(alpha_rad , zeta_rad , i , phi0_rad ,
                psi0);
            sum+=(pow((list[i].psi-psi_theo[i])/list[i].psi_error ,2));
        }
    }

    //Initializing Chi^2.
    if (phi0==phi0_val[0] && psi0==psi0_val[0]) {
        chi[counterA][counterB]=prefactor*sum;
        phi0_minArray[counterA][counterB]=phi0;
        psi0_minArray[counterA][counterB]=psi0;

    } else {
        //Minimizing Chi^2.
        if (chi[counterA][counterB] > prefactor*sum) {
            chi[counterA][counterB]=prefactor*sum;
            phi0_minArray[counterA][counterB]=phi0;
            psi0_minArray[counterA][counterB]=psi0;
        }
    }
}

//Printing the minimized Chi^2 into the output file. The python code 'J2007heatmap.py' will read in this file and visualize the Chi^2 using a heatmap.
counterA=-1;
for (float alpha=alpha_val[0]; alpha<=alpha_val[1]; alpha+=alpha_val[2])
{
    counterA+=1;
    counterB=-1;
    for (float zeta=zeta_val[0]; zeta<=zeta_val[1]; zeta+=zeta_val[2]) {
        counterB+=1;
        fprintf(output_file ,"%1f %1f %d %1f %lf\n",alpha , zeta ,
            phi0_minArray[counterA][counterB] , psi0_minArray[counterA][
            counterB] ,chi[counterA][counterB]);
    }
}

fclose(input_file);
fclose(output_file);

return 0;
}

```

Displaying the χ^2 values (heatmap)

```
# -*- coding: utf-8 -*-
#!/usr/bin/python
#
# J2007Heatmap.py
#
# Created by Tjark Miener and Bruce Allen on 27.08.17.
# Copyright (c) 2017 Tjark Miener and Bruce Allen. All rights reserved.
#
import numpy as np
import matplotlib.pyplot as plt
import matplotlib as mpl

#This function is doing the same as the function range(), but with floats.
def frange(start, stop, step):
    x = start
    while x <= stop:
        yield x
        x += step

def main():
    #Change MHZ for working with the 2000MHz data!
    MHZ = '1500'
    file = open("J2007_%sMHz_Chi.txt" % MHZ, "r")    # J2007_%sMHz_Chi-finer
    .txt" for the finer grid
    data = np.loadtxt(file, dtype=str, delimiter='\n')
    #Initialization of the arrays.
    arr_len=181      #201 for the finer grid
    chi_squared=[[-1. for _ in range(arr_len)] for _ in range(arr_len)]
    phi0_minArray=[[-1. for _ in range(arr_len)] for _ in range(arr_len)]
    psi0_minArray=[[-1. for _ in range(arr_len)] for _ in range(arr_len)]
    alpha_array=[[-1. for _ in range(arr_len)] for _ in range(arr_len)]
    zeta_array=[[-1. for _ in range(arr_len)] for _ in range(arr_len)]

    #Reading the data and writing it into the arrays.
    counterA=0
    counterB=0
    for line in xrange(len(data)):
        d=data[line].split()
        alpha_array[counterA][counterB]=float(d[0])
        zeta_array[counterA][counterB]=float(d[1])
        phi0_minArray[counterA][counterB]=int(d[2])
        psi0_minArray[counterA][counterB]=float(d[3])
        chi_squared[counterA][counterB]=float(d[4])

        #Updating the counters.
        counterB+=1
        if (counterB==arr_len):
            counterA+=1
            counterB=0

    file.close()
```

```

#Creating alpha and xi arrays for the plt.pcolormesh().
if MHZ=='1500':
    alpha_start=0.0      #100.0 for the finer grid
    alpha_end=180.0      #120.0 for the finer grid
    zeta_start=0.0        #95.0 for the finer grid
    zeta_end=180.0        #115.0 for the finer grid
else:
    alpha_start=0.0      #105.0 for the finer grid
    alpha_end=180.0      #125.0 for the finer grid
    zeta_start=0.0        #100.0 for the finer grid
    zeta_end=180.0        #120.0 for the finer grid
#Length of iteration
it_len=1.0          #0.1 for the finer grid
alpha = []
for i in frange(alpha_start ,alpha_end ,it_len):
    alpha.append(i)
alpha = np.asarray(alpha)
zeta = []
for x in frange(zeta_start ,zeta_end ,it_len):
    zeta.append(x)
zeta = np.asarray(zeta)
#To get the x-axis and y-axis of the heatmap right , the 2-dim. array
# has to be transpose.
chi_squared=np.asarray(chi_squared)
chi_squared=chi_squared.T

#Searching for the minimum and the corresponding values (alpha,zeta ,
# phi_0 ,psi_0).
chi_squared_min=chi_squared.min()
chi_squaredindex=np.where(chi_squared==chi_squared_min)
alpha_minPos=int(chi_squaredindex[1])
zeta_minPos=int(chi_squaredindex[0])
alpha_min=float(alpha_array [alpha_minPos][zeta_minPos])
zeta_min=float(zeta_array [alpha_minPos][zeta_minPos])
phi0_min=int(phi0_minArray [alpha_minPos][zeta_minPos])
psi0_min=float(psi0_minArray [alpha_minPos][zeta_minPos])

#printing out the values of the minimum.
print "Value_min: " + str(chi_squared_min)
print "Alpha_min: " + str(alpha_min)
print "Zeta_min: " + str(zeta_min)
print "Phi0_min: " + str(phi0_min)
print "Psi0_min: " + str(psi0_min)

#Marking the minimum with a cross in the heatmap and writing the values
# besides.
stringChi=r'+ \$\backslash, \chi^2_{min}=%3f\$' % chi_squared_min
stringAlpha=r'$\quad \alpha_{min}=%d^{\circ}$' % alpha_min      #%.1f
            '^{\circ} for the finer grid'
stringZeta=r'$\quad \zeta_{min}=%d^{\circ}$' % zeta_min      #%.1f
            '^{\circ} for the finer grid'
stringPhi=r'$\quad \phi_{min}=%d^{\circ}$' % phi0_min
stringPsi=r'$\quad \psi_{min}=%d^{\circ}$' % psi0_min      #%.1f
            '^{\circ} for the finer grid

```

```

plt.text(alpha_min, zeta_min, stringChi, fontsize=15)
plt.text(alpha_min, zeta_min-10, stringAlpha, fontsize=15)      #zeta_min-1
    for the finer grid
plt.text(alpha_min, zeta_min-20, stringZeta, fontsize=15)      #zeta_min-2
    for the finer grid
plt.text(alpha_min, zeta_min-30, stringPhi, fontsize=15)      #zeta_min-3
    for the finer grid
plt.text(alpha_min, zeta_min-40, stringPsi, fontsize=15)      #zeta_min-4
    for the finer grid

#Creating the heatmap with a logarithmic colorbar.
alpha, zeta = np.meshgrid(alpha, zeta)
plt.pcolormesh(alpha, zeta, chi_squared, cmap='RdYlGn', norm=matplotlib.colors.
    LogNorm(), vmin=10e-1, vmax=10e2)      #vmax=10e1 for the finer grid
cbar=plt.colorbar()
cbar.ax.set_ylabel('$ \backslash quad\chi^2 $', rotation=0, fontsize=24)
plt.title("%sMHz" % MHZ, fontsize=24)
plt.xticks([0,30,60,90,120,150,180])      #comment this line out for the
    finer grid
plt.yticks([0,30,60,90,120,150,180])      #comment this line out for the
    finer grid
plt.xlabel(r'$ \backslash alpha $ [deg]', fontsize=18)
plt.ylabel(r'$ \backslash zeta $ [deg]', fontsize=18)

#Saving the heatmap.
plt.savefig("J2007_%sMHz_ChiPlot.png" % MHZ, dpi = 600)

#Execute the main function.
if __name__ == "__main__":
    main()

```

Applying the BRM to the data of PSR J2007+2722

Calculation of χ^2 values over $(\alpha, \zeta, \phi_0, \psi_0, |\vec{E}_{BG}|^2, \psi_{BG})$

```
//  
// chi_squaredBRM.c  
//  
// Created by Tjark Miener and Bruce Allen on 02.02.18.  
// Copyright (c) 2018 Tjark Miener and Bruce Allen. All rights reserved.  
  
#include <stdio.h>  
#include <stdlib.h>  
#include <math.h>  
  
struct Data{  
    int index;           // 0 ,...,255  
    float intensityI;  
    float linearQ;  
    float linearU;  
    float linearL;  
    float circularV;  
    float psi;  
    float psi_error;  
    float e1;  
};  
struct Data list[256];  
  
//Degrees to Radians conversion.  
double deg2rad(float val){  
    return val*M_PI/180.0;  
}  
  
//Radians to Degrees conversion.  
float rad2deg(double val){  
    return val*180.0/M_PI;  
}  
  
//All arguments in the head of the function are in radians, except the  
//variable called 'index'. The returning position angle is declared in  
//radians.  
double positionAngle(float alpha, float zeta, int index, float phi0, float  
    psi0) {  
    double phi_rad=index*2*M_PI/256.0;  
    //Calculating the position angle with the rotating vector model (RVM).  
    //The result is declared in radians.  
    double x=-(sin(zeta)*cos(alpha)-cos(zeta)*sin(alpha)*cos(phi_rad-phi0));  
    double y=sin(phi_rad-phi0)*sin(alpha);  
    return atan2(y,x) + psi0;  
}  
  
//main function  
int main (int argc, char** argv) {
```

```

//Initialization of helpful variables.
int i,counter,counterA,counterB,counterE2,counterP2;
float alpha_val[3],zeta_val[3],psi0_val[3],e2_val[3],psi2_val[3];
int phi0_val[3];

//Bin size for the contourplot.
int bins=21;
int e2_bins=29;
int psi2_bins=31;

double chi[bins][bins];
float alpha_Array[bins][bins];
float zeta_Array[bins][bins];
int phi0_Array[bins][bins];
float psi0_Array[bins][bins];
double chi_min[e2_bins][psi2_bins];
float alpha_minArray[e2_bins][psi2_bins];
float zeta_minArray[e2_bins][psi2_bins];
int phi0_minArray[e2_bins][psi2_bins];
float psi0_minArray[e2_bins][psi2_bins];

FILE *input_file=fopen(argv[1],"r");
char str[35];

float alpha_theo,zeta_theo,phi0_theo,psi0_theo;
//Detecting if the input file is the profile of 1500MHz or 2000MHz.
if (argv[1][6]== '1') {
    sprintf(str, "J2007_BRM1500Chi.txt");
    alpha_theo=deg2rad(111.6);
    zeta_theo=deg2rad(104.1);
    phi0_theo=deg2rad(193.0);
    psi0_theo=deg2rad(-12.9);
    e2_val[0]=0.1;
    e2_val[1]=1.5;
    e2_val[2]=0.05;
    psi2_val[0]=40.0;
    psi2_val[1]=70.0;
    psi2_val[2]=1.0;
} else if (argv[1][6]== '2') {
    sprintf(str, "J2007_BRM2000Chi.txt");
    alpha_theo=deg2rad(115.1);
    zeta_theo=deg2rad(109.7);
    phi0_theo=deg2rad(202.0);
    psi0_theo=deg2rad(-5.5);
    e2_val[0]=0.1;
    e2_val[1]=1.5;
    e2_val[2]=0.05;
    psi2_val[0]=45.0;
    psi2_val[1]=75.0;
    psi2_val[2]=1.0;
} else {
    printf("Error! Inputfile %s is wrong!\n", argv[1]);
    exit(1);
}

```

```

//This ranges are the same for both observing frequencies .
alpha_val[0]=100.0;
alpha_val[1]=120.0;
alpha_val[2]=1.0;
zeta_val[0]=100.0;
zeta_val[1]=120.0;
zeta_val[2]=1.0;
phi0_val[0]=100;
phi0_val[1]=200;
phi0_val[2]=1;
psi0_val[0]=-20.0;
psi0_val[1]=20.0;
psi0_val[2]=1.0;

//Open the output file .
FILE *output_file=fopen(str ,”w”);
if (!input_file) {
    printf(”Error! Inputfile %s not found\n” , argv[1]);
    exit(2);
}
if (!output_file) {
    printf(”Error! Outputfile %s not found\n” , str);
    exit(3);
}

//Reading the input data and writing it into the structure (struct Data).
counter=0;
while (1) {
    int foobar1,foobar2;
    if (9==fscanf(input_file ,”%d %d %d %f %f %f %f %f %f\n”,&foobar1 ,&
        foobar2,&list [counter].index,&list [counter].intensityI ,&list [
        counter].linearQ,&list [counter].linearU,&list [counter].circularV ,&
        list [counter].psi ,&list [counter].psi_error))) {
        list [counter].linearL=sqrt(pow( list [counter].linearQ ,2)+pow( list [
            counter].linearU ,2));
        counter++;
    } else break;
}

if ( i!=EOF) {
    fprintf(stderr , ”Error! Problem reading %s at line %d . fscanf()
        returned %d\n” , argv[1] , counter+1,i);
    exit(4);
}

//Calculating the prefactor of the Chi^2 Equation .
float n=0.0;
for ( int i=0; i<=255;i++) {
    if ( list [i].psi!=0 && list [i].psi_error!=0) {
        n+=1.0;
    }
}
double prefactor=1.0/(n-6.0);

```

```

//Minimizing Chi^2 over the parameter space (alpha ,zeta ,phi0 ,psi0) plus
E2 and psi2 .
counterE2=-1;
for ( float e2=e2_val [ 0]; e2<=e2_val [ 1]; e2+=e2_val [ 2]) {
    counterE2+=1;
    counterP2=-1;
    for ( float psi2=psi2_val [ 0]; psi2<=psi2_val [ 1]; psi2+=psi2_val [ 2]) {
        printf(" Iteration:%.2f %.1f\n",e2 ,psi2 );
        counterP2+=1;
        double e3 ;
        double y[256] ,psi_rvm [ 256];
        for ( int i=0; i<=255; i++) {
            e3=list [ i ]. linearL;
            //If there is no measured psi , the theoretical psi from the RVM by
            Allen and Knispel is taken. This is an acceptable approximation
            !
            if ( list [ i ]. psi==0.0) {
                psi_rvm [ i ]=positionAngle(alpha_theo , zeta_theo , i , phi0_theo ,
                    psi0_theo );
                if ( psi_rvm [ i ]>0.0) {
                    y [ i ]=e3+e2-2*sqrt ( e3)*sqrt ( e2)*cos ( fabs ( deg2rad ( psi2 )-psi_rvm [ i ]
                        ));
                } else {
                    y [ i ]=e3+e2-2*sqrt ( e3)*sqrt ( e2)*cos ( fabs ( psi_rvm [ i ])+deg2rad (
                        psi2 ) );
                }
                list [ i ]. e1=y [ i ];
            } else if ( list [ i ]. psi<0.0) {
                list [ i ]. e1=e3+e2-2*sqrt ( e3)*sqrt ( e2)*cos ( fabs ( deg2rad ( list [ i ]. psi
                    ))+deg2rad ( psi2 ) );
            } else {
                list [ i ]. e1=e3+e2-2*sqrt ( e3)*sqrt ( e2)*cos ( fabs ( deg2rad ( psi2 )-
                    deg2rad ( list [ i ]. psi )) );
            }
        }
        counterA=-1;
        for ( float alpha=alpha_val [ 0]; alpha<=alpha_val [ 1]; alpha+=alpha_val
            [ 2]) {
            double alpha_rad=deg2rad ( alpha );
            counterA+=1;
            counterB=-1;
            for ( float zeta=zeta_val [ 0]; zeta<=zeta_val [ 1]; zeta+=zeta_val [ 2])
            {
                double zeta_rad=deg2rad ( zeta );
                counterB+=1;
                for ( int phi0=phi0_val [ 0]; phi0<=phi0_val [ 1]; phi0+=phi0_val [ 2])
                {
                    double phi0_rad=deg2rad ( phi0 );
                    for ( float psi0=psi0_val [ 0]; psi0<=psi0_val [ 1]; psi0+=psi0_val
                        [ 2]) {
                        double psi0_rad=deg2rad ( psi0 );
                        //Calculating the Chi^2 for one point of the parameter space.
                        double psi_theo [ 256];
                        double sum=0.0;

```



```

//Printing the minimized Chi_min^2 into the output file. The python code
'J2007ContourplotBRM.py' will read in this file and visualize the
Chi_min^2 using a heatmap.
counterE2=-1;
for (float e2=e2_val[0]; e2<=e2_val[1]; e2+=e2_val[2]) {
    counterE2+=1;
    counterP2=-1;
    for (float psi2=psi2_val[0]; psi2<=psi2_val[1]; psi2+=psi2_val[2]) {
        counterP2+=1;
        fprintf(output_file,"% .2f %.1f %lf %.1f %.1f %d %.1f\n",e2, psi2,
            chi_min[counterE2][counterP2], alpha_minArray[counterE2][counterP2]
            ,zeta_minArray[counterE2][counterP2], phi0_minArray[counterE2][
            counterP2], psi0_minArray[counterE2][counterP2]);
    }
}
fclose(input_file);
fclose(output_file);
return 0;
}

```

Displaying the χ^2 values (contourplot)

```

# -*- coding: utf-8 -*-
#!/usr/bin/python
#
# J2007ContourplotBRM.py
#
# Created by Tjark Miener and Bruce Allen on 06.02.18.
# Copyright (c) 2018 Tjark Miener and Bruce Allen. All rights reserved.
#

import numpy as np
import matplotlib.pyplot as plt
import matplotlib as mpl

#This function is doing the same as the function range(), but with floats.
def frange(start, stop, step):
    x = start
    while x <= stop:
        yield x
        x += step

def main():
    #Change MHZ for working with the 2000MHz data!
    MHZ = '1500'
    file = open("J2007_BRM%Chi.txt" % MHZ, "r")
    data = np.loadtxt(file, dtype=str, delimiter='\n')

    #Initialization of the arrays.
    e2_len=29
    psi2_len=31
    chi_squared=[[-1. for _ in range(psi2_len)] for _ in range(e2_len)]
    e2_Array=[[-1. for _ in range(psi2_len)] for _ in range(e2_len)]
    psi2_Array=[[-1. for _ in range(psi2_len)] for _ in range(e2_len)]

```

```

#Reading the data and writing it into the arrays.
counterA=0
counterB=0
for line in xrange(len(data)):
    d=data[line].split(' ')
    e2_Array[counterA][counterB]=float(d[0])
    psi2_Array[counterA][counterB]=float(d[1])
    chi_squared[counterA][counterB]=float(d[2])
#Updating the counters.
counterB+=1
if (counterB==psi2_len):
    counterA+=1
    counterB=0
file.close()

#Creating e2 and psi2 arrays for the plt.contourf().
e2_start=0.1
e2_end=1.51
e2_it=0.05
if MHz=='1500':
    psi2_start=40.0
    psi2_end=70.0
else:
    psi2_start=45.0
    psi2_end=75.0
psi2_it=1.0

e2 = []
for i in frange(e2_start,e2_end,e2_it):
    e2.append(i)
e2 = np.asarray(e2)

psi2 = []
for x in frange(psi2_start,psi2_end,psi2_it):
    psi2.append(x)
psi2 = np.asarray(psi2)

#To get the x-axis and y-axis of the heatmap right, the 2-dim. array
#has to be transpose.
chi_squared=np.asarray(chi_squared)
chi_squared=chi_squared.T

#Searching for the minimum and the corresponding values (e2,psi2).
chi_squared_min=chi_squared.min()
chi_squared_index=np.where(chi_squared==chi_squared_min)
e2_minPos=int(chi_squared_index[1])
psi2_minPos=int(chi_squared_index[0])
e2_min=float(e2_Array[e2_minPos][psi2_minPos])
psi2_min=float(psi2_Array[e2_minPos][psi2_minPos])

#printing out the values of the minimum.
print "Value_min: " + str(chi_squared_min)
print "E2_min: " + str(e2_min)
print "Psi2_min: " + str(psi2_min)

```

```

#Marking the minimum with a cross in the contourplot and writing the
# values besides .
stringChi=r '+ $\\chi^2_{min}=%3f$' % chi_squared_min
stringE2=r '$\\vec{E}_{BG}|^2=%2f$' % e2_min
stringPsi2=r '$\\psi_{BG}=%d^{\\circ}$' % psi2_min
plt.text(e2_min,psi2_min,stringChi,fontsize=15)
plt.text(e2_min,psi2_min-2,stringE2,fontsize=15)
plt.text(e2_min,psi2_min-4,stringPsi2,fontsize=15)

#Creating the contourplot .
e2, psi2 = np.meshgrid(e2, psi2)
clevs = np.arange(0.5,10.55,0.1)
plt.contourf(e2,psi2,chi_squared,clevs,cmap='RdYlGn')
cbar=plt.colorbar(ticks=[0.5,2.5,4.5,6.5,8.5,10.5])
cbar.ax.set_ylabel('$\\chi^2$', rotation=0, fontsize=24)
plt.title("%sMHz" % MHZ, fontsize=24)
plt.xlim(0.1,1.5)
if MHZ=='1500':
    plt.ylim(40,70)
else:
    plt.ylim(45,75)
plt.xlabel(r'$|\\vec{E}_{BG}|^2$ [mJy]', fontsize=16)
plt.ylabel(r'$\\psi_{BG}$ [deg]', fontsize=16)

#Saving the heatmap .
plt.savefig("J2007_%sMHz_ChiBRMPlot.png" % MHZ, dpi = 600)

#Execute the main function .
if __name__ == "__main__":
    main()

```

6. Bibliography

- [1] Ahmadi, P. & Gangadhara, R. T., 2002. *ApJ*, **566**, 365.
- [2] Allen, B., 2013. *ApJ*, **773**, 91.
- [3] Blaskiewicz, M., Cordes, J. M. & Wasserman, I., 1991. *ApJ*, **370**, 643.
- [4] Everett, J. E. & Weisberg, J. M., 2001. *ApJ*, **553**, 341.
- [5] Gangadhara, R. T. & Gupta, Y., 2001. *ApJ*, **555**, 31.
- [6] Goldreich, P. & Julian, W. H., 1969. *ApJ*, **157**, 869.
- [7] Goldstein, D. H., 2011, Polarized Light 3rd Edition (CRC Press)
- [8] Hewish, A., Bell, S. J., Pilkington, J. D. H., Scott, P. F. & Collins, R. A., 1968. *Nature*, **217**, 709.
- [9] Hones, E. W. & Bergeson, J. E., 1965. *J. Geo-phys. Res.*, **70**, 4951.
- [10] Kolanoski, H., 2009, Einführung in die Astroteilchenphysik (Script), 171.
- [11] Komesaroff, M. M., 1970. *Nature*, **225**, 612.
- [12] Lorimer, D. R. & Kramer, M., 2005, Handbook of Pulsar Astronomy (Cambridge University Press)
- [13] Mancuso, S. & Spangler, S. R., 2000, *ApJ*, **539**, 480.
- [14] Mestel, L., 1971. *Nature*, **233**, 149.
- [15] Michel, F. C., 1991, Theory of Neutron Star Magnetospheres (The University of Chicago Press), 299.
- [16] Michel, F. C. & Li, H., 1999, *Physics Reports*, **318**, 227.
- [17] Radhakrishnan, V. & Cooke, D. J., 1969. *Astrophys. Lett.*, **3**, 225.
- [18] Radhakrishnan, V., Cooke, D. J., Komesaroff, M. M. & Morris, D., 1969. *Nature*, **221**, 443.
- [19] Rookyard, S. C., Weltevrede, P. & Johnston, S., 2015. *MNRAS*, **446**, 3367.
- [20] Schwarz, G. E., 1978. *Ann. Statist.*, **6 (2)**, 461.

- [21] Weltevrede, P. & Wright, G., 2009. *MNRAS*, **395**, 2117.
- [22] Wit, E., van den Heuvel, E. & Romeijn, J.-W., 2012. *Statistica Neerlandica*, **66** (3), 217.
- [23] Zinth, W. & Zinth, U., 2008, Additional material to Optik, Lichtstrahlen-Wellen-Photonen (Oldenbourg Verlag)